Dynamical Complexity of Nonlinear Dynamical Systems with Multiple Delays

by

Kamyar Tavakoli

A thesis submitted in partial fulfillment of the requirements for the Doctorate in Philosophy degree in Physics

Ottawa-Carleton Institute for Physics
Department of Physics
Faculty of Science
University of Ottawa
October 2023

Declaration of Authorship

I, Kamyar Tavakoli, certify that this thesis is entirely my own original work except where otherwise indicated. I am aware of the University of Ottawa regulations concerning plagiarism, including those regarding consequent disciplinary actions. Any use of the works of any other author, in any form, is properly acknowledged at their point of use.

Abstract

The high-dimensional property of delay differential equations makes them useful for various purposes. The applications of systems modelled with delay differential equations demand different degrees of complexity. One solution to tune this property is to make the dynamics of the current state dependent on more delayed states. How the system responds to more delayed states depends on the system under study, as both decreases and increases in the complexity were observed in different nonlinear systems. However, it is also known that when there is an infinite number of delays that follow a continuous distribution, simpler dynamics usually expected due to the averaging over previous states that the delay kernel provides. The present thesis investigates the role of multiple delays in nonlinear time delay systems, as well as methods for evaluating their complexity. Through the use of pseudospectral differentiation, we first compute the Lyapunov exponents of such multi-delay systems. In systems with a large number of delays, chaos is found to be less likely to occur. However, in systems with oscillatory feedback functions, the entropy can increase just by adding a few delays. Our study also demonstrates that the transition to simpler dynamics in nonlinear delay systems can be either monotonous or abrupt. This is particularly true in first-order nonlinear systems, where increasing the width of the distribution of delays results in complexity collapse, even in the presence of a few discrete delays. The roots of the characteristic equation around a fixed point can be used to approximate the degree of complexity of the dynamics of such time-delay systems, as they can be linked to other dynamical invariants such as the Kolmogorov-Sinai entropy.

The phenomenon of complexity collapse uncovered in our work was further studied in an 80/20 ratio excitatory-inhibitory neural network. We found that the smaller the time delay, the higher the likelihood of chaotic dynamics, and this also promotes asynchronous spiking activity. But for larger values of the delay, the neurons show synchronized oscillatory spiking activity. A global inhibition at a longer delay results in a novel dynamical pattern of randomly occurring epochs of synchrony within the chaotic dynamics.

The final part of the thesis examines the behavior of time delay reservoir computing when there are multiple time delays. It is shown that the choice of spacing between time delays is crucial, and depends on the task at hand. The system was studied for a prediction

task with one chaotic input as well as for a mixture of two chaotic inputs. It was found that, similar to the single delay case, there is a resonance when the difference between delays is equal to the clock cycle. Together, our research provides valuable insights into the dynamics and complexity of nonlinear multi-delay systems and the importance of the spacing between delays.

Sommaire

La propriété de haute dimensionnalité des équations différentielles à retard les rend utiles à diverses fins. Les applications des systèmes modélisés avec des équations différentielles à retard exigent différents degrés de complexité. Une solution pour ajuster cette propriété est de rendre la dynamique de l'état actuel dépendante davantage d'états retardés. La manière dont le système répond à des états plus retardés dépend du système étudié, car des diminutions et des augmentations de la complexité ont été observées dans différents systèmes non linéaires. Cependant, il est également connu que, lorsque le nombre de retards est infini et suit une distribution continue, une dynamique plus simple en est habituellement le résultat étant donné la moyenne sur les états précédents que fournit le noyau de retard. La présente thèse examine le rôle de retards multiples dans les systèmes à retard temporel non linéaires, ainsi que les méthodes d'évaluation de leur complexité. À l'aide des méthodes pseudospectrales, nous calculons d'abord les exposants de Lyapunov de ces systèmes à plusieurs retards. Dans les systèmes avec un grand nombre de retards, le chaos est moins susceptible de se produire. Cependant, dans les systèmes avec des fonctions de rétroaction oscillatoires, l'entropie peut augmenter en ajoutant seulement quelques retards. Notre étude démontre également que la transition vers une dynamique plus simple dans les systèmes de retard non linéaires peut être soit monotone, soit abrupte. Ceci est particulièrement vrai dans les systèmes non linéaires de premier ordre, où l'augmentation de la largeur de la distribution des retards entraîne un effondrement de la complexité, même en présence de quelques retards discrets. Les racines de l'équation caractéristique autour d'un point fixe peuvent être utilisées pour approximer le degré de complexité de la dynamique de tels systèmes à retard, car elles peuvent être liées à d'autres invariants dynamiques tels que l'entropie de Kolmogorov-Sinaï.

Le phénomène d'effondrement de la complexité découvert dans notre travail a été étudié plus en détail dans un réseau neuronal d'excitation-inhibition avec un ratio de 80/20. Nous avons découvert que plus le délai est court, plus la probabilité de dynamiques chaotiques est élevée, ce qui favorise également une activité de décharge neuronale asynchrone. Mais pour des valeurs plus grandes du délai, les neurones montrent une activité de décharge oscillatoire synchronisée. Une inhibition globale avec un délai plus long entraîne un nouveau patron

dynamique ayant des périodes de synchronie apparaissant aléatoirement dans la dynamique chaotique.

La dernière partie de la thèse examine le comportement du calcul par réservoir à retard temporel lorsqu'il y a plusieurs retards temporels. Il est montré que le choix de l'espacement entre les retards temporels est crucial et dépend de la tâche à réaliser. Le système a été étudié pour une tâche de prédiction avec une entrée chaotique ainsi que pour un mélange de deux entrées chaotiques. Il a été constaté que, de manière similaire au cas d'un seul retard, il y a une résonance lorsque la différence entre les retards est proche du cycle de l'horloge. En somme, ces différents projets de recherches fournissent un aperçu important sur la dynamique et la complexité des systèmes non linéaires à plusieurs retards et sur le rôle de l'espacement temporel entre les retards.

Acknowledgements

Firstly, I would like to thank my supervisor, Professor André Longtin. His support, advice, and knowledge have been very helpful during my studies at the University of Ottawa. His passion for science and enthusiasm for exploring new ideas are truly inspiring.

My sincere thanks go out to my friends at Longtin's Lab, including Nicolas, Raphael, Alexandre, Ben, and Arthur, as well as to past members Ahmed and Mauricio.

To my lovely and wonderful parents, my father Ali and my mother Atefeh, I am deeply indebted to you for the endless efforts and sacrifices you have made to support me throughout my life.

I would also like to acknowledge my lovely brother Yashar and his wife Leila, along with their dearest baby Kian, for their encouragement and unwavering support.

Finally, I would like to express my deepest appreciation to my beloved Parisa. Thank you for your support, understanding, and encouragement. I'm grateful for your love and for your dedication.

Table of Contents

List of Tables

List of Figures

Chapter 1

Introduction

Delay differential equations have emerged as a vital tool for understanding various systems' dynamical behavior. To develop accurate and realistic models, it is essential to incorporate delays that significantly impact these systems. For example, when modeling optimal traffic flow, consideration of the driver's reaction time is crucial to representing the intricate dynamics of the motion [1,2]. In nervous systems, time delays play a significant role in understanding balance control [3,4]. In the realm of physics, semiconductor laser systems with optical feedback highlight the importance of delay differential equations. These equations enable precise modeling of such systems, which is useful for the development of chaotic communication devices [5] and random bit generator devices [6]

Time delays can interact with additional time scales - such as the system's intrinsic response time, time scale induced by additive noise, and external inputs - resulting in intriguing phenomena. For example, in social systems, the decision-making is influenced by the evolving relationship between time delays inherent in the political system and the accelerating pace of opinion dynamics [7]. In specific time delay systems, the presence of both noise and time delays can result in transient stabilization of unstable fixed points [4]. Despite the complexity of stochastic time delay systems, their analysis using density evolution via an approximate Fokker-Planck formalism can be tremendously insightful [8–10].

This research focuses on the role of time delays in nonlinear systems and how they affect the entropy of phase space trajectories. In a simple linear delay differential equation in 1D, a fixed point can lose its stability and exhibit oscillatory dynamics, which is not seen in 1D linear ordinary differential equations. Nonlinear systems can display a higher level of complexity in the presence of delays. According to the Poincaré–Bendixson theorem, two-dimensional continuous-time dynamical systems cannot exhibit chaotic behavior, as their trajectories are limited to limit cycles, or trajectories that approach fixed points. However, in systems with three or more dimensions, there is the potential for chaotic dynamics to emerge. This is particularly true for nonlinear delay differential equations, which inherently possess an infinite-dimensional phase space. In these equations, chaotic or hyper-chaotic dynamics can be observed, given the proper system parameters.

It should be noted that time delays do not always destabilize and in some cases, they can even have a stabilizing effect. For example, the amplitude death phenomenon (cessation of oscillation in the coupled oscillators) can occur in coupled oscillators [11, 12] or in the context of chaos control, a transition of chaotic to periodic dynamics by adding a feedback loop whose time delay matches the period of unstable periodic orbits [13]. Understanding these effects requires a deeper look into how time delays are represented. In some cases, for a more comprehensive representation of the system, it is occasionally important to take into account the continuum of past states, as opposed to a singular past event, as manifested in distributed delay differential equations [14, 15]. The shape of the delay distribution plays a crucial role. For example, it was shown for the Mackey-Glass equation that, as the width of the uniform delay kernel broadens, the stabilized regime in the parameter space is expected to expand, leading to more regular and predictable behavior [16]. In the case that the kernel follows a gamma distribution, the 'linear chain trick' can be utilized, enabling to convert the integro-differential equation to a set of ordinary differential equations. In particular, as the kernel's shape sharpens to a centralized peak, the distribution approaches a delta distribution. As this peak becomes more pronounced, characteristics typical of the single discrete delay case become increasingly observable [17, 18].

Despite the intricate dynamics of high-dimensional delay systems, they possess finite-dimensional properties that can be computed using methods such as the correlation dimension or correlation integral, Shannon entropy, Lyapunov exponents, Kaplan-Yorke dimension, and Kolmogorov-Sinai entropy. Deepening our knowledge of how these delay system properties evolve as the number of delays increases is vital, and is the central focus of this thesis.

This thesis is organized as follows:

Chapter 2 briefly introduces the dynamical systems and nonlinear delay differential equations used in the papers and provides a description of the main models. We also present several useful tools for studying the properties of delay differential equations.

In Chapter 3, we investigate in depth the dynamics of the Lang-Kobayashi model (LK model) in the presence of multiple delayed feedbacks when the number of delays normalizes the feedback coefficient. This system has been demonstrated, both numerically and experimentally, to be applicable to various applications, including random bit generators, chaotic communication devices, and reservoir computing. The critical distinction between the applications mentioned is that they require different dynamical characteristics to be implemented properly. For example, when applying delayed systems to reservoir computing, which is a machine learning scheme suitable for a variety of tasks such as prediction and classification, the feedback coefficient must be chosen such that the steady state is stable yet, not too distant from the destabilized regime. Conversely, random bit generator devices should operate in a regime with the highest entropy. For a modified LK model with many delays picked randomly from a uniform distribution, it has been shown that the time delay signature vanishes [19]. This is surprising since the complexity is reduced when there is a uniform distribution of delays due to averaging (and resulting smoothing) over the past delayed terms. Here we investigate the case of multiple discrete random delays chosen from a uniform distribution, as well as the distributed delay differential case of the LK model. We employ various tools, such as permutation entropy, autocorrelation function, and Lyapunov exponents approximation, to analyze the complexity of this multi-delay system. Additionally, we demonstrate the novel phenomenon of complexity collapse for first-order nonlinear delay differential equations, such as the Mackey-Glass model. We illustrate that the transition to periodic dynamics can be abrupt in this system when the width of the delay distribution increases.

In Chapter 4, we perform an in-depth analysis of two first-order nonlinear time delay systems and study how the eigenvalues of these systems behave as the density of the delays changes. We find that, irrespective of the nonlinear function in the feedback term, the general trend of the sum of the real parts of the eigenvalues is similar for two first-order nonlinear time-delay systems. This sum is shown to act as a surprisingly simple proxy for the Kolmogorov-Sinai entropy. Complexity collapse in these systems is studied through variations in the spacing between delays.

In Chapter 5, we study the dynamics of recurrent neural networks with a specific schematic of synaptic connections and time delays between units. The dynamics of spiking recurrent neural networks are affected by delayed feedback, as time delay can induce bifurcations [20]. We aim to investigate whether the aforementioned complexity collapse phenomenon can occur in a chaotic neural net model by introducing multiple delays. Chaotic dynamics of firing rate network models have been an important topic of interest, as they may help uncover unknown facts about brain dynamical diseases and disordered activity [21]. In this chapter, we also investigate the impact of periodic inputs on the network dynamics in the presence of global delayed feedback. Further, the effect of external periodic inputs on the network dynamics in the absence of the global inhibitory feedback delay is very complex, and can alter the characteristics of synchronous oscillatory activity and cause nonlinear oscillatory entrainment [22–25]. We explore chaos suppression and stability of oscillations within the network using periodic stimulation, offering insights into possible applications for controlling network behavior and mitigating irregular oscillations.

In Chapter 6, we explore the role of time delays in time delay Reservoir Computing. The infinite-dimensional properties of delay differential equations allow them to map input information into higher dimensions. By injecting information into a single nonlinear node of time delay differential equations, it has been demonstrated that the information can be processed [26] and stored, enabling tasks such as time-series prediction, classification, and speech recognition. In this chapter, we investigate the effects of connecting virtual nodes in delay reservoir computers through multiple rather than single delays. Additionally, we study how multiple delays can enhance the linear memory capacity property of the Electro-optic Oscillator model. Finally, we show preliminary results on time series predictions for the case where a mixture of chaotic signals, rather than a single signal as above, is fed into the multi-delay reservoir computer, with the goal of predicting the each signal individually.

Chapter 7 concludes the thesis and discusses open problems and future work.

Publication notes

- **Chapter 3:** This chapter appeared in [27].
  I am the main author of the research, text and figures. Supervision, corrections and comments were provided by Professor Longtin.
- **Chapter 4:** This chapter appeared in [28].
  I am the main author of the research, text and figures. Supervision, corrections and comments were provided by Professor Longtin.
- **Chapter 5:** This chapter appeared in [29].
  The initial idea of the model was originally Prof. Longtin's and I further developed and did numerical simulation of the model. I am the main author of the research, text and figures. Supervision, corrections and comments were provided by Professor Longtin.
- **Chapter 6:** All parts of this chapter, except the last one, is submitted for publication in Physical Review E. I am the main author of the research, text, and figures. Supervision, corrections, and comments were provided by Professor Longtin.

Chapter 2

Nonlinear Delay Differential Equations

2.1 Background

In this chapter, we provide essential background information for the topics addressed in this thesis. Following an overview of nonlinear dynamics, we discuss the methodologies used to assess the dynamical invariants of nonlinear delay differential equations. We then introduce the primary models utilized in this thesis. Our final section explores the use of delay differential equations in reservoir computing, demonstrating their practical utility.

2.1.1 Nonlinear Dynamics

In the study of dynamical systems, differential equations serve as a powerful mathematical tool for understanding and analyzing the behavior of complex systems across various fields. Nonlinear dynamical systems, in particular, offer rich and intricate behaviors. Often, finding analytical solutions to these equations can be challenging, necessitating the use of numerical algorithms to analyze the states of variables over time.

Upon simulating a dynamical system, the states of the variables over time can be plotted versus one another to produce a phase space plot. This simple yet powerful tool visually represents the system's evolution, highlighting its various states. Many dynamical systems exhibit fixed points, which are constant asymptotic solutions to the associated differential equations. These fixed points can be classified into stable, unstable, and semi-stable categories. Stable fixed points act as attractors, drawing nearby trajectories toward them, and once the system's state reaches them, the state remains unchanged over time. In contrast, unstable fixed points serve as repellers, pushing nearby trajectories away from them. Semi-stable fixed points may attract trajectories from one direction and repel from another. If a system's state is perturbed sufficiently and falls into the basin of attraction of another attractor, its subsequent behavior depends on the stability of that attractor: the system will settle onto a stable attractor but move away from an unstable one. Understanding the nature of these fixed points and their impact on the system's dynamics is crucial for obtaining insights into the behavior and stability of dynamical systems.

The stability of a fixed point depends on the system's parameters. The system may lose stability as its parameters are varied. This can lead to drastic changes in the system's behavior, including the emergence of new dynamical regimes. This critical point at which stability is lost is known as a bifurcation point. One specific type of bifurcation is the Hopf bifurcation, which occurs when the system's asymptotic solution transitions from a stable fixed point to a stable pure periodic behavior. In this case, the attractor plot shows a closed-form trajectory which is called a Limit Cycle, with $x(t+T) = x(t)$ where T is the period of the solution. There are three main types of Hopf bifurcation: supercritical (birth of a stable limit cycle when a parameter crosses a critical value and the fixed point loses its stability), subcritical (where the unstable limit cycle shrinks to zero amplitude, rendering the fixed point unstable, and past the parameter value at the bifurcation, there is a stable limit cycle) and degenerate (not relevant to our study).

In order to analyze the stability of limit cycles, tools such as Floquet multipliers and Poincaré sections can be utilized. Floquet multipliers of a periodic orbit can be determined using the eigenvalues of the equations of the motion linearized around the periodic orbit. Whenever the absolute value of the eigenvalues is greater than 1, the periodic orbit is unstable, otherwise it is stable or neutrally stable. The Poincaré section projects the system's N-dimensional state onto a (N-1)-dimensional space by considering a Poincaré surface that intersects the trajectories, and then monitoring the system's evolution during time and recording whenever a point hits this surface. If the points form a closed curve or intersections occur at the same point consistently, the solution is considered stable. Studying bifurcation properties is crucial in dynamical systems since, for example, in brain diseases such as epilepsy and Parkinson's disease, knowing the mechanism that leads to the bifurcation towards an unhealthy oscillatory state might provide clues towards treatment [30].

Further varying the parameters, particularly by increasing the strength of nonlinear terms, might result in higher complexity in the dynamics, and a chaotic solution can arise with its "strange" attractor. Despite these systems being deterministic, their evolution can be unpredictable. Even a slight difference in the initial condition can result in drastic differences in the long-term solution. There are several recognized routes to chaos, including period-doubling sequences to chaos (repeated period-doubling bifurcations), quasi-periodic dynamics to chaos (periodic behavior on multiple scales at once) and intermittency.

The study of chaos and nonlinear dynamics has been an active research area for several decades, as it offers a wide range of practical applications across various fields. These applications include transmitting and receiving information via chaotic signals [31–33], investigating the behavior of neurological and biological systems [34–36], exploring ecological and meteorological sciences [37, 38], and many more.

2.1.2 Delay differential equations

In dynamical systems, time lags can be critical elements that significantly impact the system's properties. These time lags may arise due to various reasons, such as communication latency (e.g. finite propagation speed of light in optical circuits or of neural activity down axons), inherent delays in the system's components or feedback mechanisms. To accurately model such systems, delay differential equations (DDEs) can be employed. The mathematical representation of a delay differential equation with multiple discrete delays can be described as:

$$\frac{dx}{dt} = f(x(t), x(t-\tau_1), ..., x(t-\tau_M)) \tag{2.1}$$

Here $x(t)$ denotes the state of the system at time t, and discrete delays are represented by $\tau_1, \ldots, \tau_M$. In the special case of first-order nonlinear delay differential equations with a single delay, the equation's representation becomes similar to that of iterated (discrete-time) maps when the response time of the system is much smaller than the delay. This correspondence enables a more straightforward analysis of the delay system, as it benefits from the well-known properties of nonlinear maps [39]. There are other types of delay differential equations, each with distinct characteristics and capable of showing different dynamical behavior. These include time-varying delays [40–43], where delay is the function of time, distributed delay differential equations [44–47] which consider a continuous distribution of delays rather than discrete delays, and state-dependent DDEs [48, 49], where the delay depends on the state of the system. Delays can also affect the derivatives of the state variable.

The study of how time delays can alter the stability of various dynamical systems and reveal diverse phenomena has been an attractive research topic in recent decades. For example, in neural systems, particularly in purely inhibitory neural networks, a delay can promote oscillations in the firing rate [50]. Beyond neuroscience, time delays can influence the dynamics of ecological models, with small delays leading to delay-induced bifurcation [51]. Moreover, time delays can give rise to phenomena such as synchronization and desynchronization [52–56]. In certain systems, time delays can also result in the emergence of chimera states, characterized by the coexistence of coherent and non-coherent solutions [57–59].

Another feature that has been extensively studied in delay systems is multi-stability [60–62]. One consequence of this property is that noise can sometimes lead to switching between multi-stable states, as shown in the semiconductor laser with optical feedback [63]. In other nonlinear systems, such as the Kuramoto oscillator model with delay, noise-induced hopping between different attractors can occur, resulting in oscillations with varying frequencies over different time spans [64]. And when there is multi-stability, the choice of the initial condition can have a qualitative impact on the solution.

In this thesis, we used a constant history (over the delay interval) for the initial condition in all simulations. The most straightforward numerical algorithm to solve DDEs is the Euler method which uses the general definition of derivatives to solve an equation. More accurate algorithms have been developed to solve such equations, such as the Heun method, the Runge-Kutta method, etc. Unless otherwise stated, numerical simulations of DDEs is done using the Runge-Kutta method in this thesis. The Runge-Kutta algorithm needs the value of the delayed variable at the unknown intermediate point $t_{n+1/2}$ to move forward with a step h from t_n to t_{n+1}. Therefore, interpolation needs to be performed. For cases with additive noise in the system, we used the Euler-Mauryama method.

2.2 Methods

In this section, we provide a concise overview of the methods employed to assess the complexity of the solutions under study.

2.2.1 Autocorrelation Function

One way to gain insight into the complexity of delayed systems (or dynamical systems in general) is to analyze the autocorrelation function (ACF) and power spectral density (PSD) of their time series. The ACF and PSD are interconnected through the Fourier Transform, and their analysis provides valuable information on the system's response time, time delays and other time scales that govern the system's dynamics. For instance, in the case of the chaotic dynamics of a semiconductor laser with optical feedback, the time delay (which is proportional to the distance between the external reflective device and the semiconductor laser device) can be detected from the ACF of the chaotic time series. When it comes to practical applications such as chaotic secure communication and random bit generation, traces of these delays can be detrimental since, for example in random bit generation, they impose periodicity in the generated random bit sequence [65]. One configuration that has effectively managed to hide the round-trip delay time from the autocorrelation function

(ACF) of the time series is the ring configuration, utilizing a dimensionless Ikeda-type equation, as outlined in the paper by Sande et al. [66]:

$$\frac{dx_i}{dt} = -x_i(t) + \beta \sin\left(x_j(t - \frac{\tau}{N}) + \phi\right), \tag{2.2}$$

where N is the number of elements in the ring, τ is the round-trip delay of the ring, and β is the feedback strength. In Eq. 2.2, for $i \in \{2, \ldots, N\}$, $j = i - 1$, and for $i = 1$, $j = N$, illustrating that each element is connected to its neighbouring element, with the first element being connected to the last element, creating a loop or ring structure. In the special case where $N = 1$, Equation 2.2 simplifies to a single Ikeda delay equation. In this scenario, within the chaotic regime, the peak around the time delay becomes more pronounced with a smaller feedback strength. The ACF of the self-delayed feedback loop and ring structure is depicted in Fig. 2.1. The time delay τ was set to 50 and $\beta = 4$.

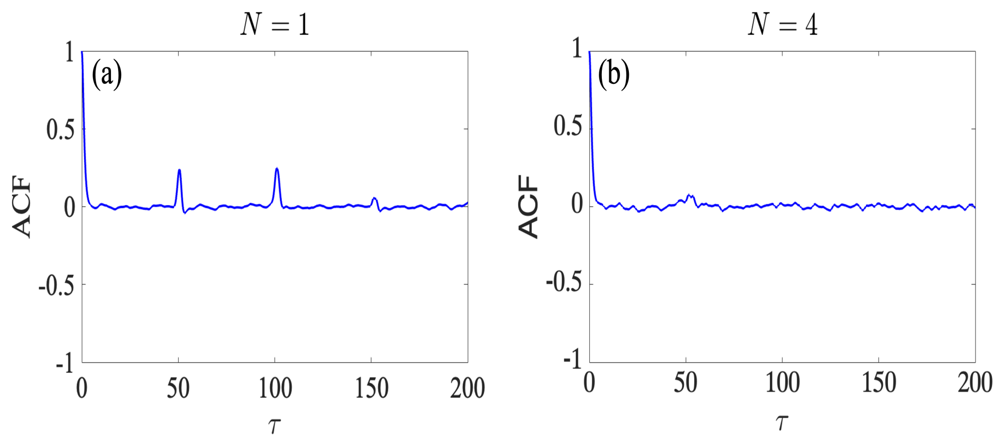

Figure 2.1: ACF of the time-series for a ring system as defined in Eq. 2.2. Panel (a) depicts the ACF for a single oscillator, while panel (b) displays the ACF for a ring structure comprising four elements. In both cases, the parameters β and τ are held constant, with values of 4 and 50, respectively.

As we can see, there are very small correlation traces when there are 4 elements in the ring, and the trace of the round-trip time in the ring becomes challenging to detect. For the Ikeda-type equation, there would be a time delay signature suppression for a very strong gain coefficient, and a tendency towards a Gaussian probability density function of the state variable is expected [67]. Other types of Ikeda models, such as the one described in [68], can exhibit dynamics that display statistical properties similar to Brownian motion. Implementing the unidirectional structure on a semiconductor laser with optical feedback also eliminates the round-trip time [66].

2.2.2 Linear stability analysis

A powerful method to analyze the stability of the nonlinear system is to conduct a linear stability analysis around a fixed point. It can help us understand whether trajectories near equilibrium points flow toward them or are repelled by them. The analysis can be done by linearizing the nonlinear equation around the steady-state:

$$\frac{d\delta x}{dt} = \mathbf{A}\delta x(t) + \sum_{i=1}^{M} \mathbf{B}_i \delta x(t-\tau_i)\,. \tag{2.3}$$

where $\mathbf{A}$ is the Jacobian of Eq. 2.1 with respect to $x(t)$ and $\mathbf{B}_i$ is the Jacobian with respect to $x(t-\tau_i)$. Assuming Eq. 2.3 has a solution of $\delta x(t) = x^* e^{\lambda t}$ around the steady state solution, λ can determine the stability of that steady state [69].

Consider the first-order nonlinear time delay Ikeda equation with multiple delayed feedback loops:

$$\frac{dx}{dt} = -x(t) + \frac{\beta}{M}\sum_{i=1}^{M} \sin\left(x(t-\tau_i) + \phi\right). \tag{2.4}$$

The steady state solution of this equation will be determined by:

$$x^* = \beta \sin\left(x^* + \phi\right). \tag{2.5}$$

For the case of a single delay ($M = 1$), we obtain the following characteristic equation:

$$-\lambda - 1 + F(x^*)e^{-\lambda\tau} = 0\,, \tag{2.6}$$

where in this case $F(x^*) = \beta\cos\left(x^* + \phi\right)$. Here, λ consists of a real part μ which governs the time scale of decay of perturbations, and the imaginary part ω which relates to the frequency of oscillation. The Hopf bifurcation point is the critical value for which there are solutions with only an imaginary part. In this case, the fixed point destabilizes at the bifurcation, and a pure oscillatory behaviour appears (it has zero amplitude at a supercritical bifurcation point). In order for the system to become destabilized and exhibit behaviour more complex than a fixed point, the real parts of the rightmost eigenvalues (in the complex plane) must be non-negative. By separating the real and imaginary parts of Eq. 2.6, the following equations can be obtained:

$$\mu + 1 - F(x^*)e^{-\mu\tau}\cos(\omega\tau) = 0 \tag{2.7}$$

$$\omega + F(x^*)e^{-\mu\tau}\sin(\omega\tau) = 0\,. \tag{2.8}$$

Firstly, we can find the Hopf bifurcation by setting $\mu = 0$, leading to the following equations:

$$\tan(\omega\tau) = -\omega \tag{2.9}$$

$$\omega^2 + 1 = F^2(x^*)\,. \tag{2.10}$$

By combining the two equations above, τ_{Hopf} can be written as:

$$\tau_{Hopf} = \frac{\tan^{-1}(-\sqrt{F^2(x^*) - 1}) + \pi}{\sqrt{F^2(x^*) - 1}}\,. \tag{2.11}$$

If we consider $\mu > 0$, we can observe that for $\tau > \tau_{Hopf}$ the fixed point is locally unstable. In Fig. 2.2, the steady state solutions of the Eq. 2.4 with $M = 1$ for three different values $\tau = 0.1$, $\tau = 1$ and $\tau = 100$ have been plotted. In this figure, stable fixed points have been depicted in blue and unstable fixed points in red.

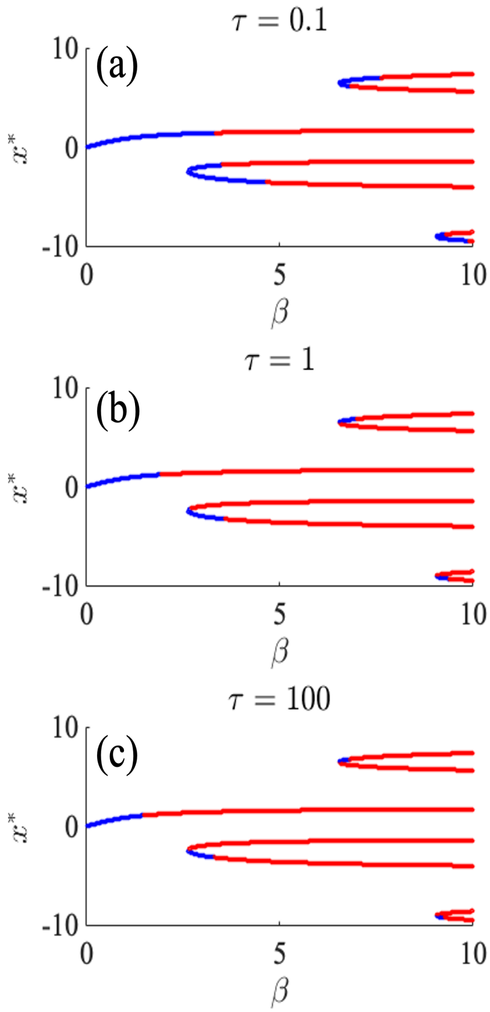

Figure 2.2: Steady states of the Eq. 2.4 for a fixed value of $\phi = 2\pi/5$ and varying feedback strength. The three rows correspond to different values of time delays: (a) 0.1, (b) 1, and (c) 100. The blue color indicates stable steady states, while the red color represents unstable steady states.

For all cases, the increase in feedback strength leads to the appearance of branches of solutions. These branches initially are stable (depicted in blue), but then turn into unstable solutions (depicted in red) as the feedback increases. Additionally, the solutions become unstable at smaller feedback coefficients for a larger time delay.

The bifurcation diagram of the Eq. 2.4 with a time delay $\tau = 200$ after a transient time of the $t = 5000$ is shown in Fig. 2.3. The bifurcation properties of these types of equations were studied in depth in [70]. The diagram illustrates the first destabilization from a stable fixed point to periodic oscillations, followed by a period-doubling bifurcation. Eventually, chaotic behavior appears. These chaotic solutions' maxima are shown to increase with the feedback coefficient.

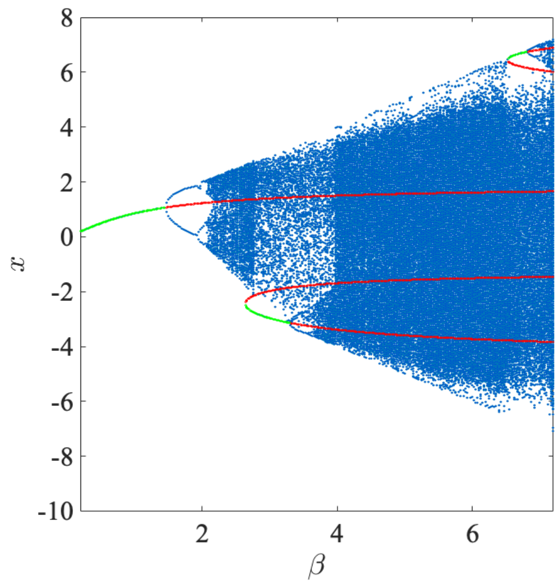

Figure 2.3: Bifurcation diagram for the time-delayed Ikeda equation (Eq. 2.4) with a constant time delay of $\tau = 200$ and increasing gain coefficient β. Green points represent steady-states that are locally stable, while red points indicate locally unstable steady-states.

The solution branches are also displayed in Fig. 2.3, which illustrates that the trace of a stable steady state solution and its subsequent loss of stability can also be seen in the chaotic regime. Plotting after a much longer time to let the transients decay results in the disappearance of the stable traces in the bifurcation diagram within the chaotic regime. The dynamics for the two cases $\beta = 3$ and $\beta = 6.53$ are illustrated in Fig. 2.4. It can be seen that multistability in the system leads to alternating intervals of chaotic dynamics and steady-state. These chaotic intervals expand with time and the chaotic period gets longer, resulting in the system's sustained chaotic behavior (see Fig. 2.3). This behavior resembles the chimera behavior observed in spatio-temporal figures for time-delayed systems. As the ratio of the time delay to the response time increases, the chimera behavior can persist for longer periods.

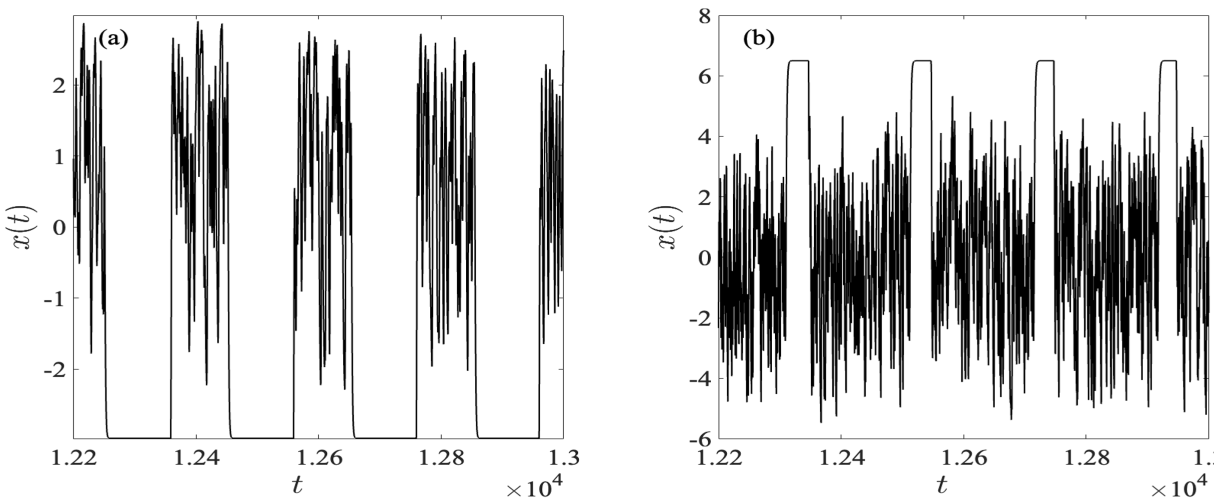

Figure 2.4: Time series plots illustrating the dynamics of the time-delayed Ikeda equation (Eq. 2.4), with (a) $\beta = 3$ and (b) $\beta = 6.53$. For both cases, the time delay τ is set to 200.

2.2.3 Lyapunov Exponents

Another method that help us determine the stability of dynamical systems for a given choice of parameters is the set of Lyapunov exponents. The main advantage of using Lyapunov exponents is the ability to determine the conditions under which chaos occurs, providing valuable insights into the behavior of the system. Secondly, Lyapunov exponents can also be used to quantify the degree of complexity of the system, along with other information such as the attractor's fractal and information dimensions. Also, by calculating the conditional Lyapunov exponents for coupled systems, we can determine whether they are synchronizable [71,72]. The Lyapunov exponent, by definition, measures the sensitivity of a system to initial conditions and the rate of divergence of trajectories. There have been many studies on how to evaluate the Lyapunov exponents of delay differential equations

[73–76]. Here, we briefly describe the method mentioned in [77]. To calculate the Lyapunov exponents of the delay systems, first we need to write the linearized form of the DDE (Eq. 2.3) and evaluate the terms using values from the numerical integration of the full nonlinear dynamical equations. Then we write the Euclidean distance of all linearized variables during the time delay τ [77, 78]:

$$D(t) = \sqrt{\sum_{i=0}^{n-1} \delta x^2(t - idt)}, \tag{2.12}$$

where $n = \frac{\tau}{dt}$ with dt being the integration time step. Here, δx represents the small deviation or perturbation from the trajectory of the system. Whenever time is an integer multiple of the time delay, all linearized variables are normalized. The norm ratio of consecutive Euclidean distances separated by the delay τ is denoted as d_j. This ratio is computed for various instants, and after iterating this calculation N times, the rate of divergence is determined by:

$$\lambda_{max} = \frac{1}{N\tau} \sum_{j=1}^{N} \ln(d_j), \tag{2.13}$$

This is the maximum Lyapunov exponent; whenever it is positive, the dynamics is chaotic. Other Lyapunov exponents can be found by considering other initial conditions for the linearized equations of the reference trajectory and using the Gram-Schmidt to orthogonalize the vectors. The existence of more than one positive Lyapunov exponent is indicative of hyper-chaotic dynamics, introducing multiple directions of sensitivity to initial conditions. Furthermore, finding more Lyapunov exponents can also help us determine the degree of complexity of the dynamical systems. For example, the Kolmogorov-Sinai entropy (KS entropy), which is the summation of the positive Lyapunov exponents, is a measure of the dynamical system's unpredictability. In Fig. 2.5, we plotted the 50 positive Lyapunov exponents and approximated the KS entropy for the Ikeda model Eq. 2.4. As we can see, the KS-entropy increases with feedback strength for this system.

In this thesis, we used the Chebyshev polynomials to estimate the Lyapunov exponents

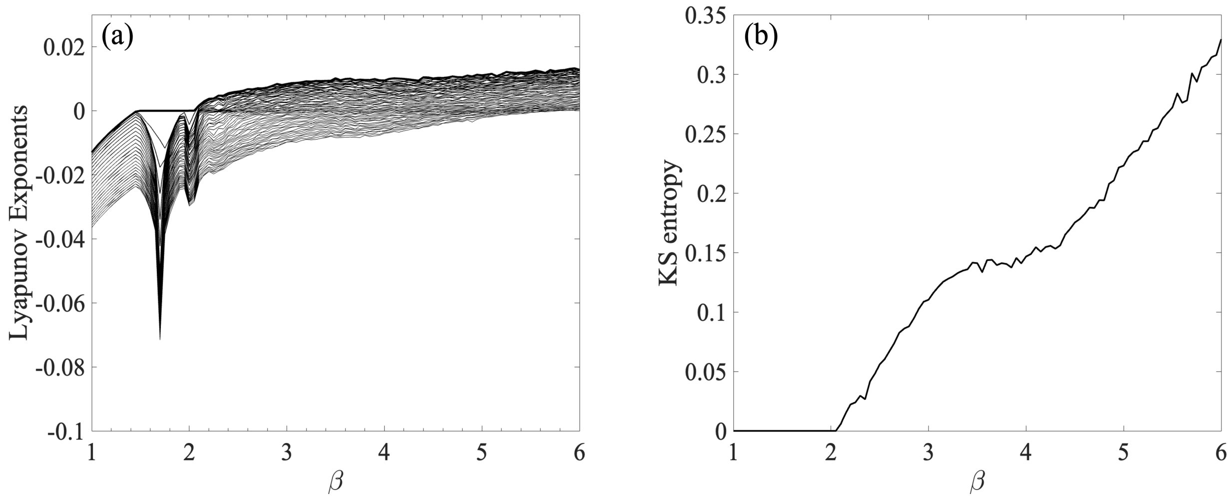

Figure 2.5: Lyapunov spectrum (a) and KS entropy (b) of the Ikeda model (Eq. 2.4) with a constant time delay of $\tau = 50$ and increasing feedback strength.

for the multiple delay systems, a novel method that is explained in the next chapter.

2.2.4 Permutation Entropy

We can determine a system's complexity without knowing its dynamical equations using metrics such as estimating Shannon entropy. Even though Shannon Entropy is useful, it does not account for the temporal information embedded within the time series [79]. A more accurate method called Permutation Entropy (PE) was suggested in [80]. Unlike Shannon Entropy, PE considers the ordering of the data points in the time series, enabling the detection of temporal patterns that the Shannon Entropy does not capture. This method is as follows: Consider time series data mapped to the vector $x = [x_1, x_2, ..., x_N]$, where N represents the total number of data points. We can construct "subdivision vectors", X_j, of dimension D. These can be represented as:

$$X_j = [x_j, x_{j+\tau'}, ..., x_{j+(D-1)\tau'}], . \tag{2.14}$$

In this equation, τ' is the embedding delay, which is equal to $\frac{\tau}{dt}$. Here, τ is the time delay and dt refers to the step size. It is recommended to set the value of the embedding dimension D between 3 and 7 [80]. From each subdivision vector X_j, a new vector X'_j is created by assigning ranks to the elements of X_j based on their magnitude. This vector X'_j represents an ordinal pattern that captures the relative ordering of values in X_j. The probability distribution of each ordinal pattern $p(\pi_i)$ is [80–82]:

$$p(\pi_i) = \frac{\#[j|j \leq N - (D-1)\tau'; X'_j \textit{has type } \pi_i]}{N - (D-1)\tau'} \,. \tag{2.15}$$

Once these probabilities are obtained for all ordinal patterns, the permutation entropy can be calculated by the following equation:

$$H[p] = \frac{-\sum_{i=1}^{D!} p(\pi_i) \log p(\pi_i)}{\log D!} \,. \tag{2.16}$$

$H[p]$ can take values between zero and one. The higher value means higher complexity, and hence a higher degree of randomness in the time-series. This tool is a computationally efficient method to evaluate the predictability of the system. We can also differentiate stochastic and chaotic deterministic dynamics by using permutation entropy [79, 83].

To illustrate the effectiveness of PE in determining the time scales of the dynamics, we initially examined the ACF and permutation entropy of Eq. 2.4 with a single delay, as shown in the top row of Fig. 2.6. In this case, we set the gain coefficient β to the very high value of 12, making it challenging to detect the time delay in the equation. Considering the potential complexities caused by additional delays, we also present a scenario with two time delays in the bottom row of Fig. 2.6.

The complexity in both cases is high, yielding little information about the delays due to the absence of distinct peaks at the time delays within the ACF. When there are two delays, the ACF primarily provides a signature around the difference between time delays, rather than the delays themselves. However, through the use of permutation entropy, we can detect not only the difference between time delays, but also identify the time delays themselves. This distinction underscores the power of permutation entropy as a versatile

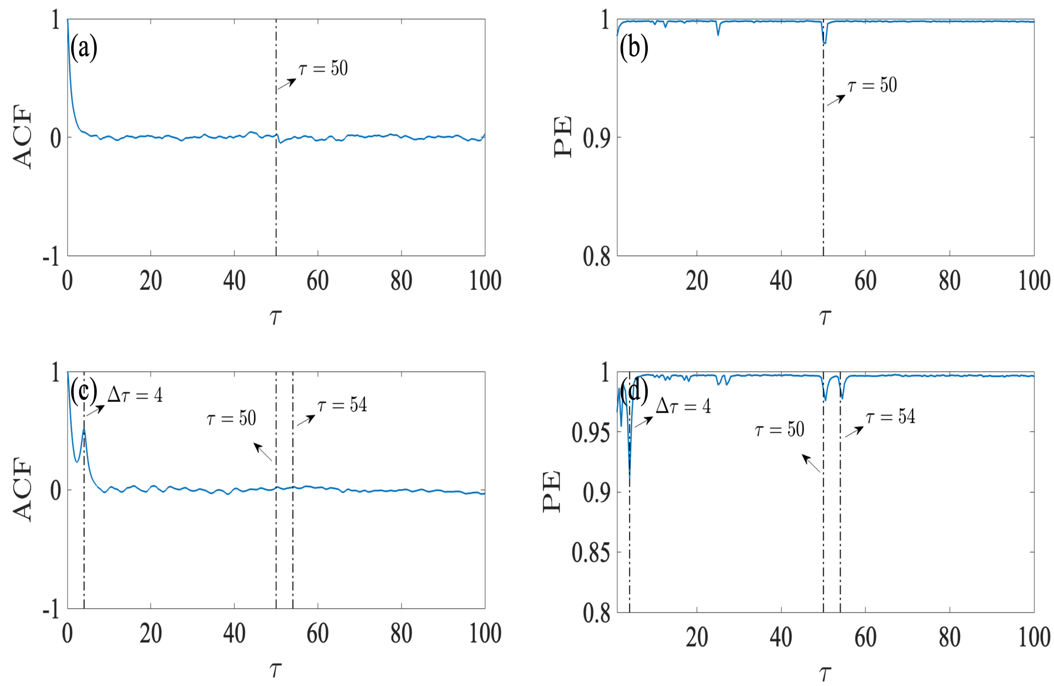

Figure 2.6: ACF (a, c) and permutation entropy (b, d) of the time series for the Ikeda model (Eq. 2.4) with different numbers of delays. The top row shows the case with one feedback loop ($M = 1$), and the bottom row shows the case with two feedback loops ($M = 2$). The first column shows the ACF and the second column shows the permutation entropy. The parameters β and τ are fixed at $\beta = 12$ and $\tau = 50$ for the first column, and $\tau_1 = 50$ and $\tau_2 = 54$ for the second column.

tool in time series analysis.

2.3 Models

We briefly introduce the models that we used throughout this thesis in this section.

2.3.1 Lang-Kobayashi Model

The Lang-Kobayashi Model serves as a valuable framework for understanding the chaotic dynamics of semiconductor lasers with optical feedback. Its ability to account for the intricate interplay between the laser's intrinsic characteristics and the external feedback has made it a cornerstone model for nonlinear dynamics and laser physics. The transition to the chaotic state as parameters are changed can vary based on the distance of the external reflective device and other parameters that determine the intrinsic response time of the semiconductor laser [84]. The model encapsulates the dynamics through the following equations:

$$\frac{dE(t)}{dt} = \frac{1}{2}\left[\frac{G_N(N(t)-N_0)}{1+\epsilon E^2} - \frac{1}{\tau_p}\right]E(t) + \kappa E(t-\tau)\cos(\omega\tau + \phi(t) - \phi(t-\tau)) \tag{2.17}$$

$$\frac{d\phi(t)}{dt} = \frac{\alpha}{2}\left[\frac{G_N(N(t)-N_0)}{1+\epsilon E^2} - \frac{1}{\tau_p}\right] - \kappa\frac{E(t-\tau)}{E(t)}\sin(\omega\tau + \phi(t) - \phi(t-\tau)) \tag{2.18}$$

$$\frac{dN(t)}{dt} = J - \frac{N(t)}{\tau_s} - \frac{G_N(N(t)-N_0)}{1+\epsilon E^2(t)}E^2(t)\,. \tag{2.19}$$

where E is the electric field, ϕ is the electric phase and N is the carrier density. The rest of the parameters and their values are summarized in the Table 3.1 in chapter 3. The derivation of the Lang-Kobayashi equations assumes that the higher-order reflections are neglected, and thus the model works best for weak to moderate feedback strength. The dynamics of the system, as described by these equations, can be further elucidated by comparing the relaxation oscillation period (which arises from the interplay between laser intensity and carrier density time scales) with the time delay. In the case of a semiconductor laser without optical feedback, the relaxation oscillation period can be calculated using the following equation [84]:

$$\tau_{RO} = \left(\frac{1}{\tau_p\tau_s}(\mu-1) - \frac{\mu^2}{4\tau_s^2}\right)^{-1/2} \tag{2.20}$$

where

$$\mu = G_N\tau_p\tau_s\left(J - \frac{N_0}{\tau_s}\right)\,. \tag{2.21}$$

The dynamics predicted by the Lang-Kobayashi model are highly dependent on the time delay τ. When this delay is small ($\tau < \tau_{RO}$), the system exhibits behaviors such as regular pulse packages where the dominant time scale is the round-trip time [85]. For $\tau > \tau_{RO}$, high-dimensional chaotic attractors are expected for moderate to strong feedback [86], yet the time delay signature is still detectable from the ACF of the time series. When the time delay is close to the relaxation oscillation period, it is more difficult to obtain information about the time scales of the system [87, 88].

In the Lang-Kobayashi equations, the coupling between the electric field and the phase is governed by the parameter α. Increasing it augments the nonlinearity and complexity of the dynamics. However, a high value of α does not necessarily guarantee the ideal outcome for applications such as cryptography (chaos communication) and random bit generator devices, since the time delay signature can still be traced from the phase time series [89]. One potential solution is optical injection from other semiconductor lasers which can help to destroy the time delay signature [82]. Apart from eliminating the time delay signature, optical injection can also induce highly stabilized regimes under specific parameter conditions [78, 90]. In the context of reservoir computing using the LK system, when optical injection is employed, it's important to note that optimal performance can often be achieved by operating near the bifurcation point or the edge of chaos [91, 92]. The dynamical equations of the LK model in the presence of multiple feedback delays is studied in more detail in Chapter 3.

2.3.2 Mackey-Glass

The Mackey-Glass model, a prominent first-order nonlinear delay differential equation, serves as a physiological model of blood cell production. The following equation describes the Mackey-Glass model:

$$\frac{dx}{dt} = -ax(t) + \frac{\beta x(t-\tau)}{1 + x^n(t-\tau)}\,. \tag{2.22}$$

Here a represents the rate at which x is destroyed, β is the rate at which x is produced, and τ is a cellular maturation time. This equation has two steady state solutions: $x^* = 0$

and $x^* = (\frac{\beta}{a} - 1)^{1/n}$; the stability of these fixed points can be analyzed with Eq. 2.11.

The model's intricate behavior arise from the influence of the time delay; in the chaotic regime, increasing the delay value enhances the fractal dimension of the chaotic attractor [73]. The bifurcation diagram of the system reveals a sequence of period-doubling bifurcations as a consequence of either increasing the time delay or the feedback strength. The model has been experimentally implemented in electronic circuits [93–96] and applied in diverse areas, such as secure communication systems [33] and reservoir computing [26].

2.3.3 Electro-optic Oscillator model

The Electro-optic oscillator model is another instance of a first-order nonlinear time delay differential equations. Experimentally, this model involves a Mach-Zehnder modulator for nonlinear transformation and a delay line, which together mimic the high-dimensional characteristics of delay differential equations. The combination of these features can lead to hyper-chaotic dynamics within an electro-optic oscillator. Furthermore, the presence of multiple time-scales in the dynamics of these equations allows them to display a variety of phenomena. Slow-fast dynamics [57, 97, 98], chimera states under certain parameter selections, and chaotic breathers [99, 100] have all been observed. The Ikeda-like electro-optic oscillator model is expressed as follows [101, 102]:

$$\frac{dx}{dt} = -x(t) + \beta \sin^2(x(t-\tau) + \phi) \tag{2.23}$$

where x is the Kerr phase shift, ϕ is the phase offset and β is the feedback strength. Similar to the Ikeda model discussed in Subsection 2.2.2, this model's steady states can be determined numerically. With an increase in the feedback strength, the number of solutions multiplies. The system's rapid fluctuations and the possibility of synchronization of its chaotic behavior with that of another system have attracted much interest, particularly for applications in chaos-based communication technologies [103].

2.3.4 Neural Networks

In this section, we delve into the dynamics of neural networks involving time delays. It's common for firing rate-based neural networks to neglect delays. Our analysis focuses on a neural network that is represented by the following equation [104, 105]:

$$\frac{du_i}{dt} = -u_i(t) + \sum_{j=1}^{N} w_{ij} f(u_j(t-\tau)) \,. \tag{2.24}$$

In this model, N denotes the number of neurons, w_{ij} represents the weight matrix, and f is the activation function. The aggregate input received by a neuron from other neurons in the network is represented by the summation term. In this section, for the sake of simplicity to perform stability analysis, the hyperbolic tangent function has been employed as an activation function. However, in Chapter 5, a logistic sigmoid function is used instead in the context of spiking recurrent neural networks where the spiking activity follows Poisson statistics.

We follow the method outlined in [104], which considers deviations of unit activities from a fixed point, described by $\delta u_i(t) = \delta u_i^* e^{\lambda t}$. By plugging $\delta u_i(t)$ into the linearized equation of Eq. 2.24, we obtain:

$$e^{-\lambda\tau}(1+\lambda)\delta u_i^* = \sum_{j=1}^{N} w_{ij}\delta u_j^* \,. \tag{2.25}$$

In this equation, the values of the weight matrix are chosen randomly from a Gaussian distribution, $\mathcal{N}(0, g^2/N)$, where g represents the average synaptic gain. We have numerically solved Eq. 2.25 for the values of λ. The real and imaginary components of λ are depicted in the top panels of Fig. 2.7, with the weight matrix's eigenvalues shown in the bottom panels. It has been demonstrated in various studies that, in the absence of time delays, when the real part of some of the eigenvalues of the weight matrix exceeds 1, chaotic dynamics can be expected. This notion is evident in Eq. 2.25, where setting $\tau = 0$ and assuming the existence of a root λ with a positive real part results in an eigenvalue for the weight matrix equal to $1 + \lambda$.

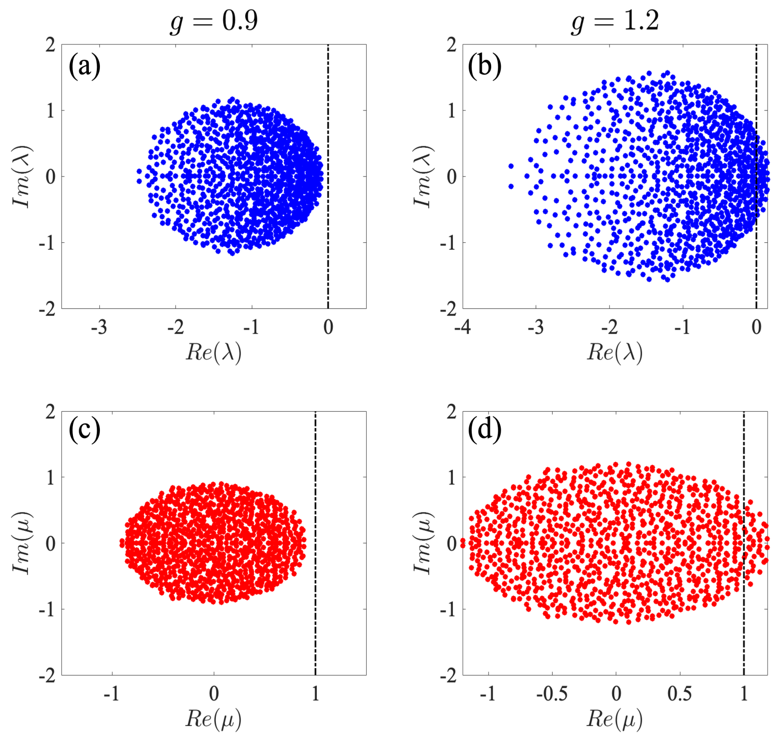

Figure 2.7: Eigenvalues of Eq. 2.25 and of the weight matrix for different gain coefficients g with $N = 1000$. The top row illustrates the eigenvalues of Eq. 2.25 with (a) $g = 0.9$ and (b) $g = 1.2$ with $\tau = 0.2$. The bottom row depicts the eigenvalues of the weight matrix for (c) $g = 0.9$ and (d) $g = 1.2$.

For $g > 1$, the second column in Fig. 2.7 displays roots indicative of chaotic dynamics, which is not observed for $g = 0.9$. In the above equation, the time delay itself does not have a specific effect and there will still be numerous roots with positive real parts for larger time delay; as the correlation between the weight matrix elements changes, the time delay becomes critical [104].

2.4 Reservoir Computing

Reservoir computing models, such as Echo State Networks (ESNs), are computationally efficient tools algorithms for time-series prediction. They utilize the transient states and fading memory properties of a dynamical system to perform machine learning tasks. They mimic the structure of neural networks by providing a high-dimensional phase space motion. There are fixed random connections between neurons, to which inputs are fed and outputs are read out. The inputs kick the system into complicated transients. The high diversity of response behaviours provides a pool of waveforms that can be combined from the neurons (or "nodes") in the network to predict future behaviour from current behaviour. Only the output weights are adjusted through supervised learning. In its most basic form, this learning amounts to a regression between desired outputs and actual outputs.

A new, easy-to-implement numerical and experimental scheme for reservoir computing was suggested by Appeltant et al. [26]. They used the high-dimensional property of delay-differential systems to map input information into higher dimensions, in contrast to classical reservoir computing which injects all inputs into one nonlinear node. In this scheme it is assumed that there exist N virtual nodes, which are separated with identical distance θ, and the time duration for each loop is $T = N\theta$. The simple architecture of the delay reservoir computing is shown in Fig. 2.8.

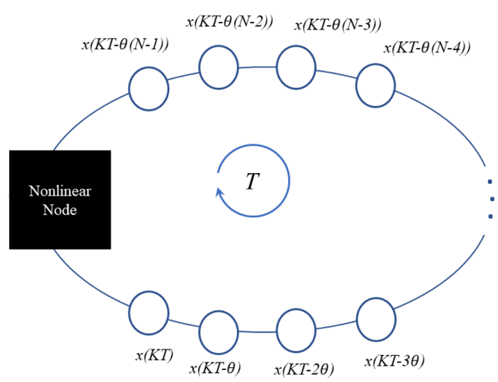

Figure 2.8: Schematic of the RC. Time Multiplexed masked input travels along the loops with a clock cycle of T. The virtual nodes are spaced with a distance of $\theta = \frac{T}{N}$.

The operation scheme is explained in more detail in Chapter 6. To inject the input into the nonlinear node and pass it along the all virtual nodes, time-multiplexing is used to create temporally separated virtual nodes. An input time series to be predicted (for example, the x component of the classic Lorenz system) is sampled for the duration of one clock cycle time T. These sampled values are further multiplied by a rapidly varying "mask" made up of a sequence of N randomly chosen binary numbers. These multiplexed

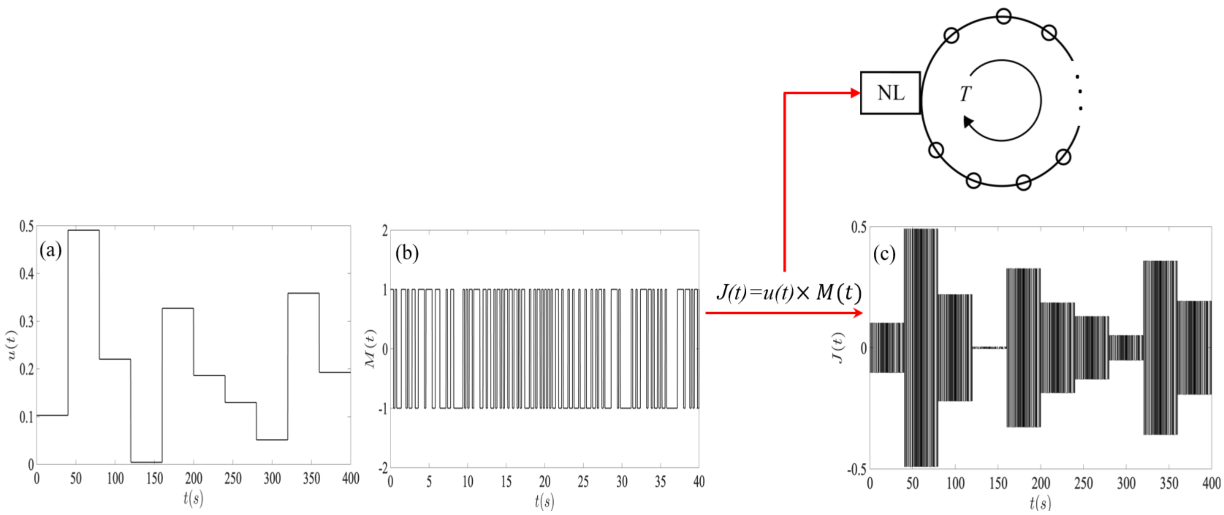

Figure 2.9: Processing of the input signal in the nonlinear node. (a) Discrete inputs are multiplexed. (b) The mask function, which is a series of random -1 or 1 values. (c) The multiplexed masked input signal is fed into the nonlinear node (e.g. the laser dynamical equations).

inputs then will be injected into the nonlinear DDEs. The samples of the input multiplied by the random mask, $M(t)$, thus elicit complex transient behaviour from the reservoir. Consider Eq. 2.4 for the delay reservoir computing model:

$$\dot{x} = F(x(t), x(t-\tau), J(t)) = -x(t) + \beta \sin(x(t-\tau) + \phi + \gamma J(t)) \tag{2.26}$$

where γ is the input scaling factor and $J(t)$ is the multiplexed masked input. These virtual nodes are read out and weighted to solve a given task [26]. Considering N virtual nodes and a clock cycle T, there is a time difference $\theta = \frac{T}{N}$ between two neighbouring nodes, which is much smaller than the time delay and also smaller than the response time of the system ($\tau_R = 1$). By storing the states of these nodes and the responses to each input over time, a state matrix with the dimension $K \times N$ can be constructed:

$$X = \begin{bmatrix} x(T-\frac{T}{N}(N-1)) & x(T-\frac{T}{N}(N-2)) & \dots & x(T) \\ \\ x(2T-\frac{T}{N}(N-1)) & x(2T-\frac{T}{N}(N-2)) & \dots & x(2T) \\ \\ \vdots & & \ddots & \vdots \\ \\ x(KT-\frac{T}{N}(N-1)) & x(KT-\frac{T}{N}(N-2)) & \dots & x(KT) \end{bmatrix}_{K \times N}$$

Ideally, the goal is to train a weight matrix such that when we multiply it by the nodes states matrix, we can predict the next target output values:

$$o = X \times W\,. \tag{2.27}$$

To avoid over-fitting, we used the ridge regression method, which solves the $argmin(||XW-o||_2^2 + \lambda||W||_2^2)$ problem with regularization parameter λ and $||.||_2$ is the Euclidean norm. Solution of this regression leads to the following form for W:

$$W = (X^T X + \lambda I)^{-1}(X^T o)\,. \tag{2.28}$$

In our work (Chapter 6), λ is set to 10^{-8}. The standard task that we considered to illustrate the performance of delay reservoir computing is known as the Narma10 task which is a benchmark that can be used to evaluate the performance of the reservoir computers. It consists in predicting the sequence of values obtained from the following nonlinear high-dimensional difference equation:

$$o_{n+1} = 0.3o_n + 0.05o_n(\sum_{i=0}^{9} o_{n-i}) + 1.5u_{n-9}u_n + 0.1 \tag{2.29}$$

in which u_n is the input; we try to predict the value of o_{n+1}. u_n is an independent random number drawn from a uniform distribution from the interval $[0, 0.5]$. This task involves a mixture of linearity and nonlinearity, as each output depends on the previous steps before, and on the other hand inputs are picked randomly. Figure 2.10 shows the one step-ahead prediction task for Narma10 (the input) using Eq. 2.4 as the nonlinear node, i.e. as the core of the reservoir computer. The time delay is set to 58 and the clock cycle is 40, $\gamma = 0.4$ and $\beta = 1.35$. As we explain later in Chapter 6, there is memory degradation whenever the clock cycle is close to the time delay used in the dynamics of the nonlinear node. Here, for this part, we used 4 samples of input each with a length of 5000 for the training set and 2500 for the testing set.

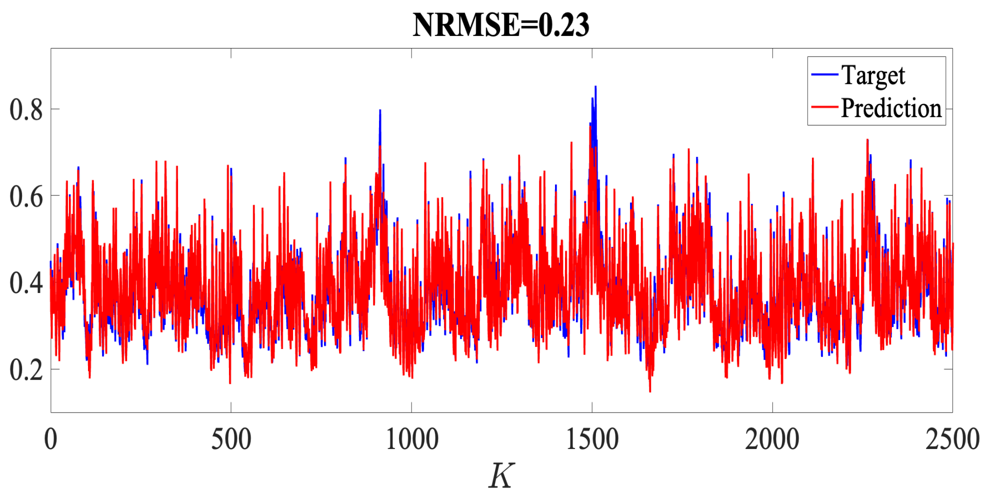

Figure 2.10: Prediction of the NARMA10 task using Eq. 2.26 as a nonlinear delay system for the reservoir. The blue line represents the target output, while the red line indicates the predicted values. The parameters used are $\tau = 58$, $T = 40$, $\gamma = 0.4$, $\phi = 2\pi/5$, and $\beta = 1.35$.

This figure shows that this architecture produces an acceptable prediction of such a complicated time series using a single nonlinear node with a single delay. We used 200 virtual nodes spread evenly along the delayed feedback loop. Increasing the number of virtual nodes can decrease the error between the target output and predicted output.

Chapter 3

Multi-delay Complexity Collapse

Abstract

Increasing the number of delays in nonlinear dynamical systems is generally assumed to lead to higher complexity, but "distributed delay" systems with an infinite number of delays to lesser complexity. This paradox is studied here using the Lang-Kobayashi laser model by first extending a recent method for Lyapunov exponent estimation from single to multiple delays. The Kolmogorov-Sinai entropy, permutation entropy, and time delay signature suppression initially increase with number of delays as the dynamics become more hyperchaotic. At a large number of delays that depends on the feedback strength, this trend reverses, leading to simpler dynamics. The phenomenon is also found in other delay equations, such as the Mackey-Glass system. A similar collapse is uncovered in the distributed delay case with broadening delay kernel.

Delay Differential Equations (DDEs) are a class of dynamical systems governed by some memory of the past. They exhibit a rich array of behaviors in a broad range of applications [6,106,107]. Their multiple timescales [108] can be exploited for the generation of oscillatory [109] and chaotic time series, including the recently discovered laminar chaos [110], as well as for stabilizing complex dynamics [111] and unstable steady states [112]. What role plays the number of delays M? Adding a second delay has been shown experimentally to induce hyperchaotic behavior [113]. More recently, fiber gratings in semiconductor lasers that synthesize large numbers of random delays have been used to produce strongly hyperchaotic dynamics with application to random number generation and secure chaos communication [19].

In contrast, stabilizing effects can also arise with multiple delays. Second and third delays added to the Lang-Kobayashi (LK) laser system can produce continuous-wave dynamics with enhanced stability [114]. A second delay can stabilize unstable periodic orbits in the Mackey-Glass (MG) system [115], and many feedback terms with delays that are integer multiples of a fixed delay can control unstable periodic orbits [116]. Feedback control of Chua's circuit with two different delays can replace chaos by simpler stabilized steady states [117]. Dependence on an infinite number of past states defines distributed delay systems with integrodifferential dynamics that are also generally "simpler"—i.e., with a less positive spectrum of Lyapunov exponents (LEs) and smaller dynamical entropy especially when the feedback kernel is broad (see, e.g., Ref. [118]).

Although details matter to some extent, a general paradox does emerge: More delays can lead to stronger chaos, but a large number of delays - and sometimes even two delays - can lead to simpler dynamics. This M-dependent transition is not well understood, and our paper studies this paradox using a semiconductor laser model with many delays. Such lasers with optical feedback are useful in our context due to their ability to produce high-dimensional hyperchaotic behavior. Modes with frequency less than the characteristic frequency of the laser in isolation (i.e., without feedback) can destabilize the fixed point through a Hopf bifurcation, yielding a limit cycle, then a torus, and eventually chaos and hyperchaos [119].

Information about the presence of a time delay can be extracted from the chaotic time series by the autocorrelation function (ACF), delayed mutual information or permutation entropy [120]. Setups involving optical injection, rings [66] or phase conjugate optical feedback mirrors [121] have been shown numerically and experimentally to suppress the time-delay signature (TDS) in the ACF, thereby increasing unpredictability. TDS suppression can be achieved with multiple random (but fixed) delays, a useful property for random number generation [19,122]. To understand the complexity transition at higher M, we make use of the TDS from the ACF, but also estimate dynamical invariants, including Lyapunov exponents through an extension of a method for a single delay [75]. The dimensionless laser Lang-Kobayashi semiconductor laser model with multiple discrete delays can be expressed as

$$\frac{dE(t)}{dt} = (1+i\alpha)\left[\frac{G_E[N(t)-N_0]}{1+\epsilon|E(t)|^2} - \gamma_E\right]E(t) + \frac{\kappa}{M}\sum_{i=1}^{M} E(t-\tau_i)e^{-i\omega\tau_i}, \tag{3.1a}$$

$$\frac{dN(t)}{dt} = \gamma_N[J_r N_{th} - N(t)] - \frac{G_N(N(t)-N_0)}{1+\epsilon|E(t)|^2}|E(t)|^2, \tag{3.1b}$$

where $E(t)$ is the slowly varying complex electric field, $N(t)$ is the carrier density, M is the number of delays, and κ is the feedback strength. The τ_i are the delay times. The intrinsic relaxation oscillation period of this system is $\tau_{ro} = 0.75$. The values and descriptions of the parameters used in Eq. 3.1 are presented in Table 3.1.

Table 3.1: Parameter values used for the simulation of the Lang-Kobayashi model Eq. 3.1.

Parameter	Description	Value
α	Linewidth enhancement factor	5
ω	The frequency of the solitary laser	1.226×10^6
J_r	The pumping factor	1.05
N_0	The transparency carrier density	81.2585
G_E	Differential gain for electric-field amplitude	13.8447
G_N	The gain coefficient for carrier density	0.26156
ϵ	The gain saturation	0.00872
γ_N	Inverse of carrier lifetime	0.490196
γ_E	Inverse of photon lifetime for the electric field	259.471
λ	Wavelength	1.537×10^{-6}m

We assume that the random fiber grating consists of M segments, each with length half of $L = 1.8$ mm. The delays are picked randomly for each segment as

$$
\begin{aligned}
\tau_i &= \tau_{\text{avg}} - \frac{(i-1)L}{2\bar{c}} - \Delta\tau_i, \quad i \text{ is odd}, \\
\tau_i &= \tau_{\text{avg}} + \frac{(i-2)L}{2\bar{c}} + \Delta\tau_i, \quad i \text{ is even},
\end{aligned}
\tag{3.2}
$$

where i is from one up to the maximum number of delays M, with $\tau_{avg} > (M+1)L/(2\bar{c})$ and $\Delta\tau_i$ is randomly chosen from $[0, \frac{L}{\bar{c}}]$, the average delay is $\tau_{avg} = 5$ and $\bar{c} = c\bar{T}$ where c is the speed of light and $\bar{T}$ normalization constant for time which is 1 ns. Time series were obtained using a fourth-order Runge-Kutta routine with a time-step 4×10^{-4}. Figure 3.1 shows the interplay of the different timescales with M for fixed feedback strength κ. For the single delay case, the ACF displays a sharp peak at multiples of the delay [Fig. 3.1(b)]. For 20 delays, Fig. 3.1(e) displays no time-delay signature around the time delays, however, peaks around τ_{ro} become more pronounced.

For large M, such as 160 delays in Fig. 3.1(g), the attractor appears like a torus, and the ACF displays two components with timescales of τ_{avg} and τ_{ro}. This is reminiscent of the single-delay weak feedback case where the external cavity causes periodic oscillations. The time delays still affect the dynamics; their ACF signatures are seen around lag τ_{avg} with contributions of similar magnitude to that of the intrinsic response. $M = 180$ leads to a limit cycle with period τ_{ro}, and only the fast intrinsic frequency is left. Increasing M to 1000 leads to a fixed point in Fig. 3.1(m).

The central peak of ACF at lag 0 broadens as the number of delays increases, and it is modulated by oscillations with a period near the intrinsic period τ_{ro} (Fig. 3.2). It is known [123] that such oscillations are visible in ACF peaks when the feedback strength is not too high; otherwise the ACF peaks are too narrow to resolve those oscillations. In this sense, increasing the number of delays to 20 seems to have a similar effect to lowering the coupling strength. But, as we will see below, the complexity measures behave nonmonotonically as a function of M in this range of coupling strengths.

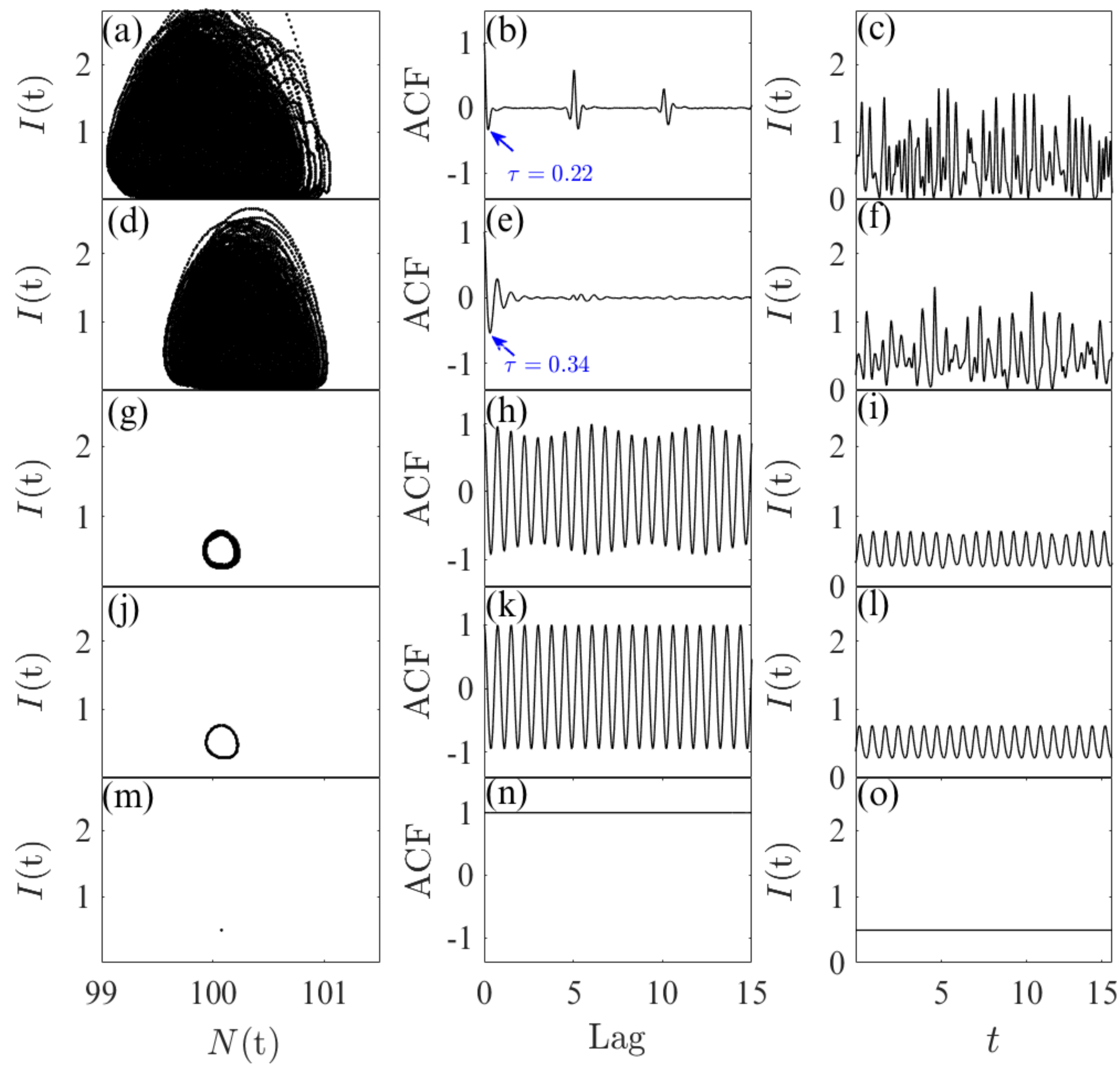

Figure 3.1: Increase followed by decrease in dynamical complexity with increasing number of delays. Intensity-carrier number phase plots (left), ACF of the intensity $[I(t) = |E(t)|^2]$ (center), and intensity time series (right) for (from top to bottom) $M = 1, 20, 160, 180, 1000$. The feedback strength is $\kappa = 10$.

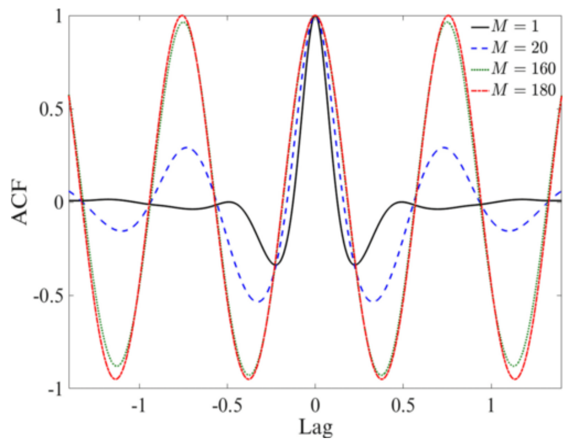

Figure 3.2: Broadening of the central peak as the number of delays M increases for the LK model.

We can rewrite Eq. 3.1a as a function of optical phase ϕ and intensity $I = |E|^2$:

$$\begin{aligned}\frac{dI(t)}{dt} =& 2\left[\frac{G_E[N(t)-N_0]}{1+\epsilon I(t)} - \gamma_E\right] I(t) \\ &+ \frac{2\kappa}{M}\sum_{i=1}^{M}\sqrt{I(t)I(t-\tau_i)}\cos\{\omega\tau_i + 2\pi[\phi(t)-\phi(t-\tau_i)]\},\end{aligned} \tag{3.3a}$$

$$\begin{aligned}\frac{d\phi(t)}{dt} =& \frac{\alpha}{2\pi}\left[\frac{G_E[N(t)-N_0]}{1+\epsilon I(t)} - \gamma_E\right] \\ &- \frac{\kappa}{2\pi M}\sum_{i=1}^{M}\sqrt{\frac{I(t-\tau_i)}{I(t)}}\sin\{\omega\tau_i + 2\pi[\phi(t)-\phi(t-\tau_i)]\},\end{aligned} \tag{3.3b}$$

The numerically estimated densities of the feedback term in Eq. 3.3a are shown in Fig. 3.3. The standard deviation clearly decreases with increasing M, and the shape goes from unimodal to multimodal. The density appears almost skewed Gaussian for $M = 20$, but this is generally not the case.

A small value of the ACF at a lag around the mean time delay is suggestive of a parameter regime that is more strongly chaotic and vice versa. This intuition arises because this simple ACF measure is inversely proportional to the TDS, which generally decreases the stronger the chaos is - although no direct theoretical link has been established between

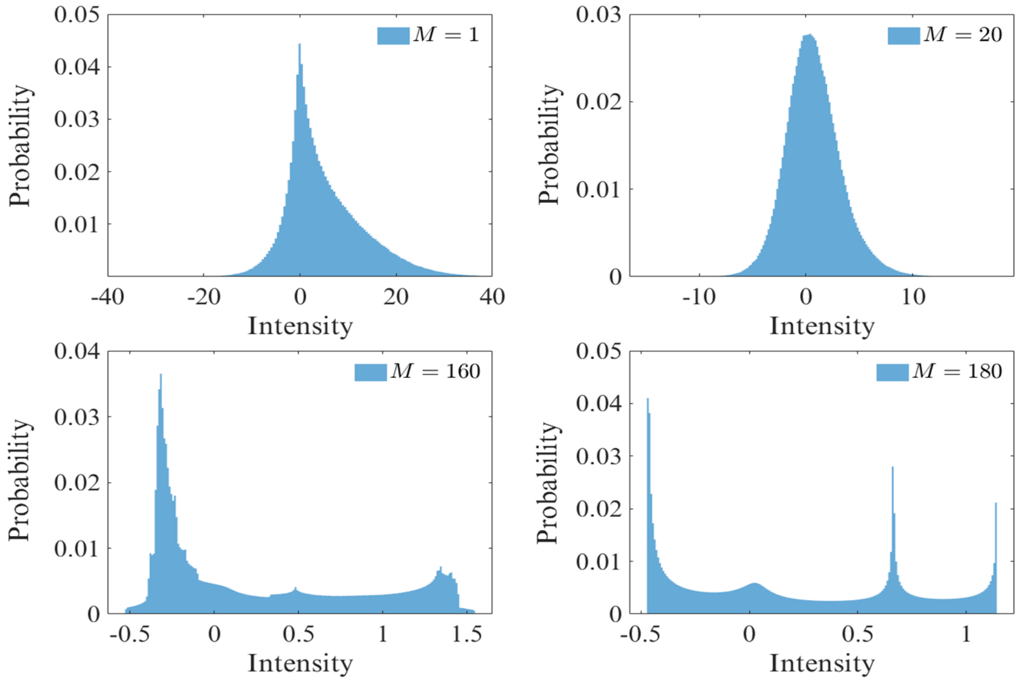

Figure 3.3: Probability density of the total feedback term in Eq. 3.3a for different number of delays.

low TDS as measured in the ACF and positive sub-Lyapunov exponents (see Ref. [124]). We thus plotted the maximal peak of the ACF around the mean delay for different M and κ values in Fig. 3.4(a). Blue (dark gray) regions, starting at $M = 1$ and $\kappa = 3$, correspond to regimes where TDS is small, whereas red (intermediate gray) regions, starting at $M = 5$ and $\kappa = 2$, reflect torus, limit cycle, and fixed point behavior. Increasing κ at fixed M, first the value of this maximal peak decreases, corresponding to transitions from fixed point to limit cycle to chaos, until it reaches a minimum. In this low-signature regime, the dominant time scale is the intrinsic response of the laser. For larger M, however, a stronger feedback coefficient is needed to enter the chaotic regime, suggestive of relatively simpler dynamics for large M.

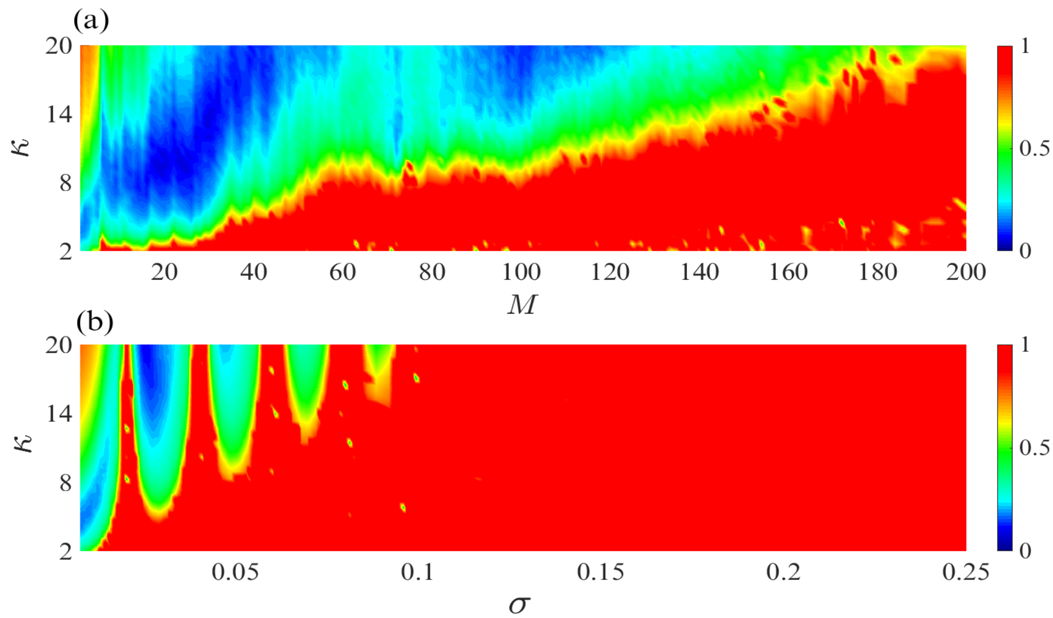

Figure 3.4: (a) Impact of feedback strength κ and number of delays M on the maximal peak height of the ACF around the mean time delay for multiple discrete delays. (b) Impact of κ and width of the delay kernel on the maximal peak height of the ACF around the mean time delay in the distributed delay case.

When the number of delays become infinite, the state of the system depends on a continuum of past states. Such ecological [125] or neural feedback [118] distributed delay differential systems are known to have simpler dynamics, especially when the delay kernel is broad. They can be expressed using integrodelay differential equations,

$$\frac{dE}{dt} = \int_0^\infty g(\tau) F[N(t), E(t), E(t-\tau)] d\tau, \tag{3.4}$$

where $g(\tau)$ denotes the kernel which must satisfy $\int_0^\infty g(\tau)d\tau = 1$. Here, we used the uniform distribution for $g(\tau)$, and $F[N(t), E(t), E(t-\tau)]$ is the right-hand side of Eq. 3.1a, and $N(t)$ evolves as in Eq. 3.1b. The maximum peak of the ACF near τ_{avg} for different widths of the delay distribution σ and feedback strength are depicted in Fig. 3.4(b). The periodic structures in Fig. 3.4(b) show that semiconductor laser dynamics with distributed delays keep transitioning between states of high and low TDS, until no more chaos exists ($\sigma \geq 0.12$). These structures occur when the width of the distribution (σ) times ω is approximately $2n\pi$ where n is a positive integer. In this case, the coupling between delayed terms and the current state requires a very strong feedback coefficient, since the sum of the $\exp(i\omega\tau_i)$ factors is a very small value. Figure 3.5 shows the collapse of complexity for this distributed LK model for increasingly broad delay kernels, i.e., for a larger range of delays. Note that simulating these dynamics involves a fixed discretization of the delay kernel set here to the integration time step; the trapezoidal rule was used for the integral.

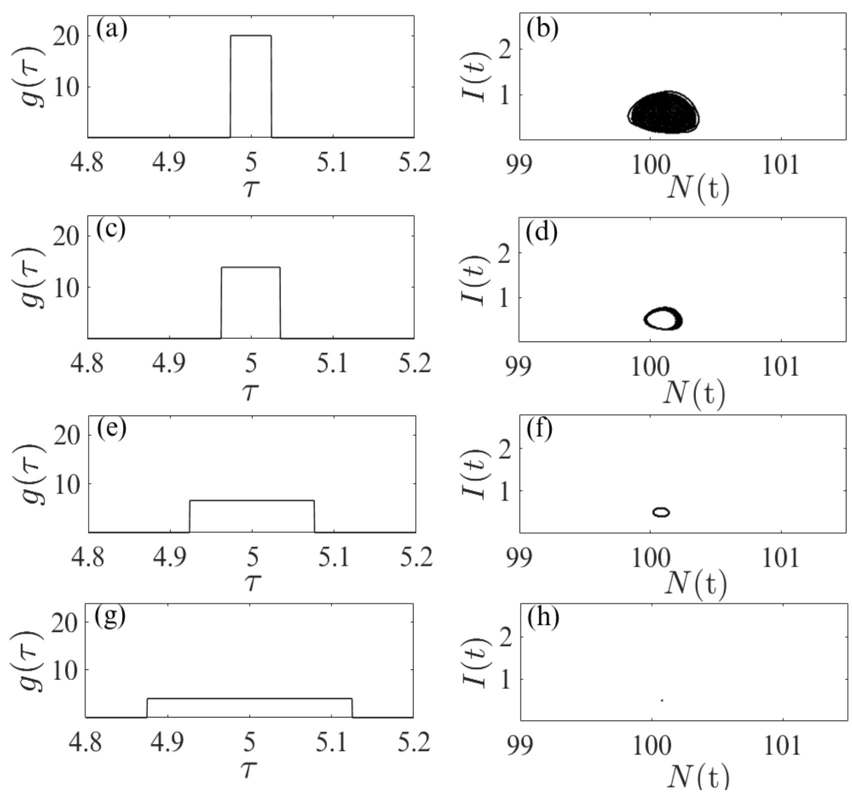

Figure 3.5: Uniform distributions (left) and attractors in the intensity-carrier number subspace (right) for total width of the delay kernel equal to (from top to bottom) $\sigma = 0.05$, 0.072, 0.152 and 0.25 for $\kappa = 10$.

Calculation of the Kolmogorov-Sinai (KS) entropy can generally be used to quantify the unpredictability of the motion since it measures the average information loss rate. It can be computed by summation of all the positive Lyapunov exponents, but the estimation of the Lyapunov spectrum for multiple delays is an open problem. Here, we resolve this issue by converting the multidelay DDE to $m_t + 1$ ordinary differential equations [75],

$$\begin{aligned} u_0'(t) &= f[x(t), x(t-\tau_1), \ldots, x(t-\tau_M)], \\ u_k'(t) &= \sum_{j=0}^{m_t} d_{kj} u_j(t), \quad k = 1, \ldots, m_t, \end{aligned} \tag{3.5}$$

where the $u_j(t)$'s are functions defined on the Chebyshev nodes θ_{ij} during the interval $x(t-\tau_i)$ and $x(t-\tau_{i-1})$, $f[x(t), ..., x(t-\tau_M)]$ is the right hand side of Eqs. 3.1a-3.1b, and τ_M is defined in Eq. 3.2. The quantity m_t is defined further below. The $m_i + 1$ Chebyshev nodes on each of the M intervals (τ_{i-1}, τ_i) between successive delay pairs in the discrete delay distribution are defined as

$$\begin{gathered} \theta_{ij} = \frac{(\tau_i - \tau_{i-1})}{2} \cos\left(\frac{j\pi}{m_i}\right) - \frac{(\tau_i + \tau_{i-1})}{2}\,, \\ i = 1, ..., M, \qquad j = 0, ..., m_i\,. \end{gathered} \tag{3.6}$$

This formula shows that the nodes between each pair of delays are spaced differently in a manner that depends on the m_i values. It should be noted that only the evolution of $u_0(t)$ depends on the delayed variable values $x(t-\tau_i)$. The d_{kj}'s are the elements of the Chebyshev differentiation matrix. There are $m_i + 1$ nodes between delays τ_i and τ_{i-1}. The m_i values can be determined by numerically solving [126]:

$$\left(\frac{\tau_1 - \tau_0}{m_1}\right)^{m_1} = \left(\frac{\tau_2 - \tau_1}{m_2}\right)^{m_2} = ... = \left(\frac{\tau_M - \tau_{M-1}}{m_M}\right)^{m_M}, \tag{3.7}$$

in such a way that $\sum_{i=1}^{M} m_i = m_t$ and $\tau_0 = 0$. We calculate the Lyapunov exponents from the evolution of the state vectors for the associated linearized differential equations of Eq. 3.5 with reorthogonalization after each time step using the modified Gram-Schmidt method [77,127].

Lyapunov exponents have not been computed previously for the multidelay LK model using this method, nor have they been estimated experimentally, and thus it is not possible to independently validate our new method for estimating Lyapunov exponents. We can, nevertheless, get a good degree of confidence by checking that it reproduces known exponent values when restricted to the single delay case. We plotted the four largest Lyapunov exponents in Fig. 3.6(a) for the LK model with a single delay in the weak chaos regime (at high feedback strength). We can see the dependency of the Lyapunov exponents on the time delay. As mentioned in Ref. [124], using a larger delay makes the Lyapunov exponents smaller such that after a limit, $\lambda_m \tau$ becomes almost constant where λ_m is the maximal Lyapunov exponent. The effect of feedback strength κ on these maximum Lyapunov exponents is shown in Fig. 3.6(b). The highest value of the maximal LE is found for $\kappa = 13$. Further increasing the feedback strength decreases these four maximal Lyapunov exponents, and they also get closer to each other. Parameters used in Eq. 3.1 for Figs. 3.6 and 3.7 are taken from Ref. [128] in order to compare the values obtained for the LK model. We found a good match between the Lyapunov exponents calculated in Ref. [128] and we further extended the simulation for higher feedback coefficients. Namely, to compare some values, we got $\lambda_m = 0.44$ and $\lambda_m = 2.43$ for $\kappa = 3.4$ and $\kappa = 7.8$ respectively, whereas the values found in Ref. [128] were approximately 0.43 and 2.5.

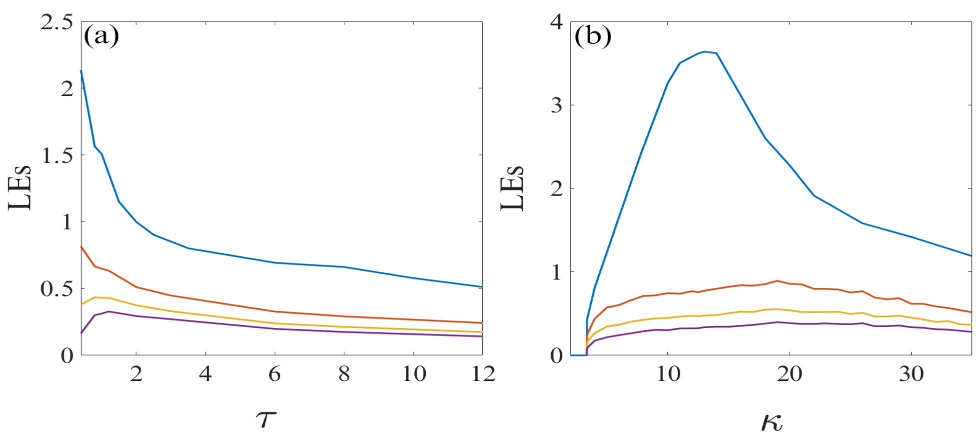

Figure 3.6: The four largest LEs (a) versus the time-delay τ with fixed feedback strength $\kappa = 35$, and (b) versus κ for fixed time-delay $\tau = 2$. The LK model here has only a single delay.

We can obtain further validation using another test where a second feedback pathway with a different delay ($\tau_2 = 1.4$) is added to the single delay case above ($\tau_1 = 2$) and check the behavior of the exponents as the strength of the second pathway becomes small. Specifically, instead of normalizing the feedback strength in Eq. 3.1 by the usual constant factor $1/M$, we assumed that each delayed feedback pathway has its own weight w_i which is multiplied by κ. We performed the calculation for a two-delay system. In the first case, we set $w_1 = w_2 = 0.5$. We see, in Fig. 3.7(a), that the largest Lyapunov exponent occurs for $\kappa = 19$, that this value is larger than in the single delay case Fig. 3.6(b) and that the exponents again converge for larger values of κ. In the second case shown in Fig. 3.7(b), we weaken the second delayed feedback by setting $w_1 = 0.95$ and $w_2 = 0.05$. The maximum Lyapunov exponent now occurs for a smaller κ; in fact, the curve is seen to converge to the one in Fig. 3.6(b). In other words, when the shorter delayed feedback pathway makes a very weak contribution to the dynamics, the system behaves dynamically very closely to the single delayed LK model in Fig. 3.6, an intuition that is reflected in our exponent estimations.

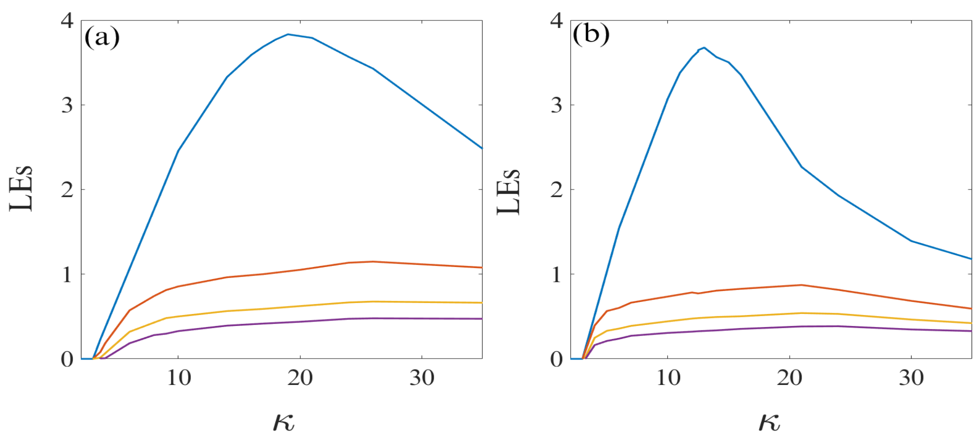

Figure 3.7: The four largest Lyapunov exponents versus feedback strength for a configuration with two delayed feedback pathways. The delays are $\tau_1 = 2$ and $\tau_2 = 1.4$. (a) Both pathways have the same weight: $w_1 = w_2 = 0.5$. (b) Pathway weights are asymmetric with $w_1 = 0.95, w_2 = 0.05$. The upper curve in (b) is close to the upper curve in Fig. 3.6(b). This is one validation of the Lyapunov exponent estimation method: the spectrum for two delays converges to that for the larger delay on its own when that larger delay pathway dominates.

The KS entropy is plotted versus M and κ in Fig. 3.8 using parameter values in Table 3.1 and $\tau_{avg} = 5$. One sees that for low κ, increasing M brings the KS entropy to zero as the dynamics transition from hyperchaos to limit cycle. There is a small remnant of chaos even for $M = 16$ for which the entropy is 0.3 ($\kappa = 2$); it is essentially zero for $M = 40$. For larger κ, the entropy is still relatively high at $M = 40$ but exhibits the key decreasing trend that qualitatively agrees with Fig. 3.1. Numerical calculation of entropies for the large M values in Fig. 3.1 are prohibitive, but the slow decay seen in Fig. 3.8(a) suggests that simpler dynamics may, in fact, consist of a small scale chaotic attractor with a simple (e.g. limit cycle) skeleton. For a fixed number of delays, increasing κ first brings on a strong chaos regime (unpredictability increases), followed by a weak chaos regime (unpredictability decreases) (Fig. 3.8(b)). These notions were first introduced in Ref. [124]: for strong chaos, the nonlinearity due to the relaxation oscillation is high, and for weak chaos, the feedback strength is either high or low. It can be seen that for more delays, a higher KS entropy can be obtained. However, the starting entropy values for small κ shift rightward for larger M, i.e., predictability increases, and the motion is simpler.

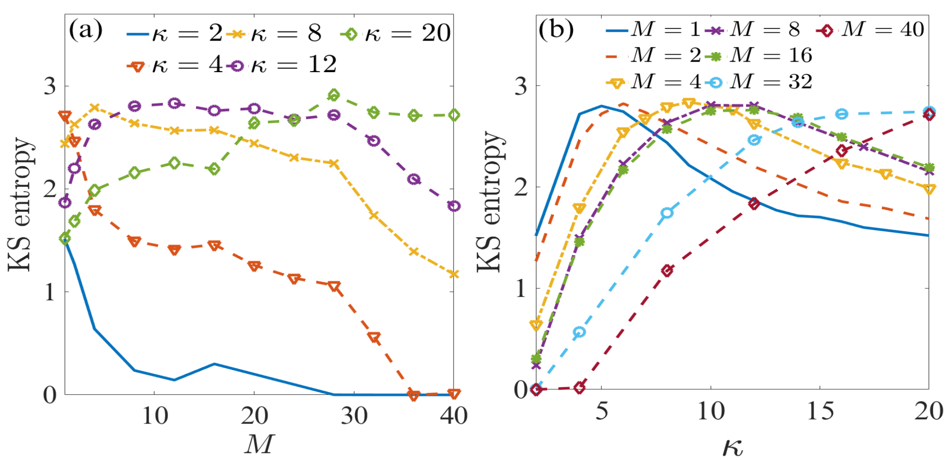

Figure 3.8: KS entropy (a) as a function of the number of delays when the feedback strength is fixed, and (b) as a function of the feedback strength when the number of delays is fixed.

We also calculated permutation entropy (PE) of the intensity time series to study the dependency of the complexity (entropy production) on M and κ [80]. Since the mean time delay is approximately the same for any M, we used the time delay for the single delay case in Fig. 3.1 as the embedding delay. PE can take values between 0 and maximal complexity 1. In agreement with the analyses up to now, Fig. 3.9(a) shows that PE is a nonmonotonic function of M when κ is sufficiently large, although the decrease is very slow at large M. We can see in Fig. 3.9(b) that, the smaller M gets, the weaker κ must be to reach high complexity. But the ordering of the curves with M inverses at stronger feedback like for the KS entropy, with a stronger κ being needed to reach higher values of PE.

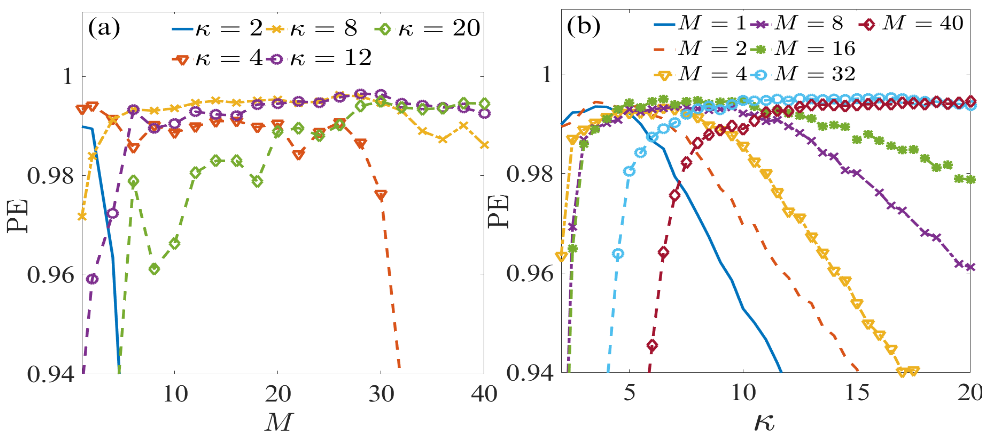

Figure 3.9: Permutation entropy (a) as a function of the number of delays when the feedback strength is fixed, and (b) as a function of the feedback strength when the number of delays is fixed.

Whereas increasing M in the discrete delay case or the kernel's width in the distributed delay case, the mean and standard deviation of the feedback term [last term in Eq. 3.3a] decrease (Fig. 3.3). This is not surprising for the LK system where the sum of harmonic functions at random phases in the numerator is overtaken by the $\frac{1}{M}$ normalization factor. As M increases, the density of the feedback fluctuations that was unimodal at low M becomes more U-shaped, similar to that for a sine wave, and narrows as well. The intuitive picture offered by the complexity collapse is one where large M delayed dynamics increasingly resemble those of a periodically driven, nondelayed, and underdamped stochastic system with small residual chaotic fluctuations thickening apparently simple limit cycles (Fig. 3.1(g)); this analogy will be pursued elsewhere.

We also observed the complexity collapse with M in the Ikeda model after an initial increase (not shown). Next, to illustrate the generality of this multidelay complexity collapse phenomenon, we turn to its investigation in a nonlinear delay differential system where the flow does not contain harmonic functions, in contrast to e.g. the LK and Ikeda systems. Specifically, we consider the MG model governed by

$$\frac{dx(t)}{dt} = -\gamma x(t) + \frac{\beta}{M}\sum_{i=1}^{M}\frac{x(t-\tau_i)}{1+x(t-\tau_i)^{10}}\,. \tag{3.8}$$

Here we set $\gamma = 1$, $\beta = 2$ and $\tau_{avg} = 17$. The discrete delays are chosen in the same way as for the LK model above: new delays required for a higher value of M are chosen randomly from the distribution and added to the delays used in the simulation for the previous lower value of M. We see, in Fig. 3.10 that, for a sufficiently large M, simple oscillatory behavior arises.

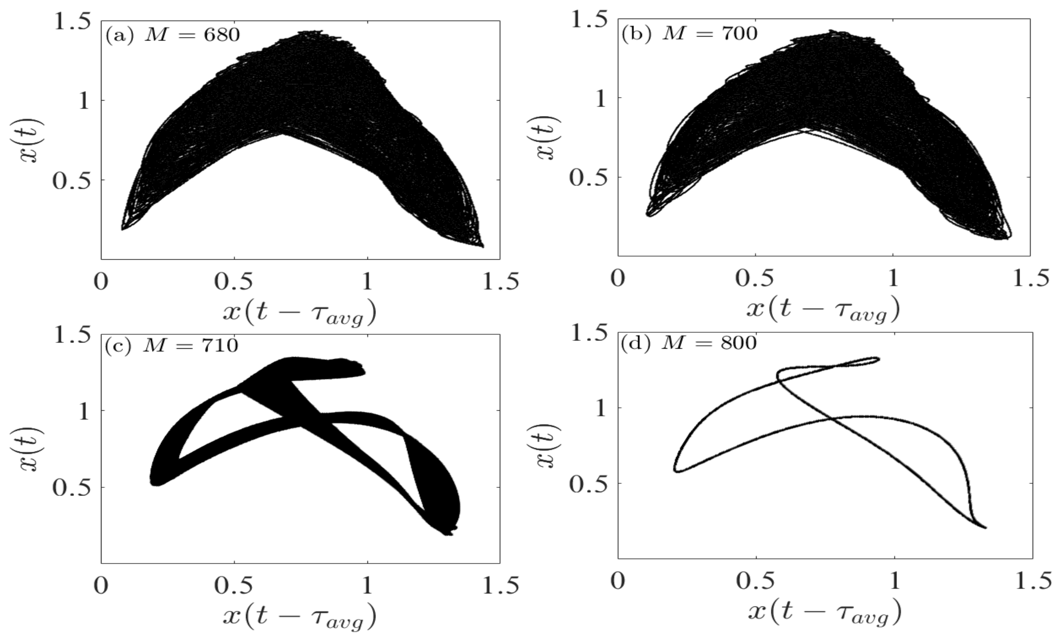

Figure 3.10: Attractor evolution of the Mackey-Glass system for an increasing number of delays. Here, $x(t)$ describes the current state, whereas $x(t-\tau_{avg})$ refers to the state at the average time delay in the past. Simplification of the dynamics occurs as for the Lang-Kobayashi model at a large number of delays.

The feedback function then has a multimodal stationary density, and the correlation time of the feedback function, i.e., the first time when the ACF of the feedback equals 1/e of its maximum at lag 0, increases. Figure. 3.11(a) shows the behavior of the correlation time versus M. After $M = 40$, a monotone increase in the correlation time with M is observed until around $M = 705$ at which point it begins a rapid drop by about 10 percent. Figure 3.11(b) displays the behavior of the permutation entropy versus M, and a sharp drop is also seen around $M = 705$. The dynamics beyond the drop display a moderately shorter correlation time and a significantly lower entropy that is compatible with what is seen in the phase plots of Fig. 3.10. In contrast to the LK Model, however, the dynamical complexity in the MG system does not increase upon adding delays starting at $M = 1$ or, at least, not for these parameter settings.

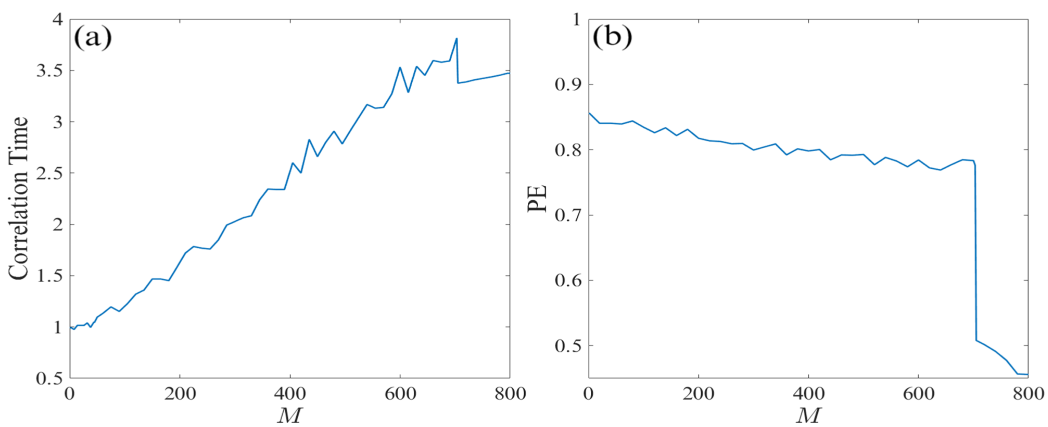

Figure 3.11: (a) Correlation time and (b) Permutation entropy for Mackey-Glass versus the number of delays. As in the attractor plots for $M < 705$, high complexity can be observed. A sudden complexity collapse occurs at $M = 705$.

In conclusion, we found a limiting number of discrete feedback delays for the LK model beyond which the complexity gradually collapses to simpler motion, characteristic of distributed delays with sufficiently broad memory kernels. Adding delays causes more interference pathways for the feedback light, enhancing the relaxation oscillation, and lowering the TDS. This oscillation eventually bifurcates to a stable fixed point. This phenomenon appears as a generic feature of multidelay dynamical systems and likely of networks with large numbers of delays, and its origin may be linked to the low effective dimension observed in stochastic distributed delay systems [129]. Multidelay nonlinear systems may, thus, paradoxically exhibit simple behavior. A differential delay system owes its complexity, in part, to the continuous perturbations that the nondelayed system receives from delayed feedback at a specific time in the past relative to the present, i.e., to the underlying dynamics of a discrete-time nonlinear map. Adding more delays at different times amounts to attenuating this discrete nature of these perturbations thereby causing a reversion to simpler dynamics. Our paper highlights this progressive loss of complexity, which can ,in fact, include steep drops as in the MG case.

Chapter 4

Dynamical Invariants and Inverse Period-doubling Cascades in Multi-delay Systems

Abstract

We investigate transitions to simple dynamics in first-order nonlinear differential equations with multiple delays. With a proper choice of parameters, a single delay can destabilize a fixed point. In contrast, multiple delays can both destabilize fixed points and promote high-dimensional chaos but also induce stabilization onto simpler dynamics. We show that the dynamics of these systems depend on the precise distribution of the delays. Narrow spacing between individual delays induces chaotic behavior, while a lower density of delays enables stable periodic or fixed point behavior. As the dynamics become simpler, the number of unstable roots of the characteristic equation around the fixed point decreases. In fact, the behavior of these roots exhibits an astonishing parallel with that of the Lyapunov exponents and the Kolmogorov-Sinai entropy for these multi-delay systems. A theoretical analysis shows how these roots move back toward stability as the number of delays increases. Our results are based on numerical determination of the Lyapunov spectrum for these multi-delay systems as well as on permutation entropy computations. Finally, we

report how complexity reduction upon adding more delays can occur through an inverse period-doubling sequence.

Dynamical invariants of delay-differential equations reveal much information regarding the complexity of infinite dimensional dynamical systems. Their quantification may help us tune the degree of chaos and better use delay-differential systems in applications such as reservoir computing. For first-order nonlinear delay-differential equations, dynamical complexity is proportional to the time delay. We show that chaotic behavior persists in spite of the presence of a large number of delays as long as the density of delays is high. However, when the distance between delays becomes large, the trajectory reaches a periodic attractor or a stable fixed point after a long transient. In this manner, instead of using many delays to simplify the dynamics, fewer delays with more space between them can be used. This statement holds true for the single-variable Mackey-Glass and electro-optic oscillator model systems and raises the question of its generalization to higher-order delay-differential dynamics.

4.1 Introduction

In the past decades, delay-differential equations (DDEs) have gained much attention in many real-world systems in optics, biology, neuroscience, network science and beyond [4,20,130,131]. The presence of delays provides a more realistic understanding of a spatially extended dynamical system in which effects propagate with a non-negligible speed back to the same system or to another system to which it is coupled. In these delayed systems, when the time delay becomes greater than the intrinsic response time, periodic and even chaotic solutions can arise; multistability between attractors can also occur when the time delay is relatively large [61,94,132]. The possibility of implementing delayed dynamics in electronic [94] and optical devices further enables both fundamental studies and the development of various applications from secure communication devices and random number generators to enhanced machine learning-based prediction techniques using reservoir computing [26,133].

However, chaotic and oscillatory behavior is not desired in all situations. For example, in reservoir computing devices, linearity is sometimes needed to increase the memory and decrease the task performance error [134]. The most studied technique for chaos control works by adding a perturbation made of the weighted difference between the current state and the past state to the original dynamical equation, which results in a stabilized periodic attractor or stable fixed point. This method is enhanced by using multiple delayed feedback control [117]. Other forms of delayed feedback control have been suggested to stabilize the unstable periodic orbits, e.g., in the Mackey-Glass (MG) model [135,136].

Studies on various models have reported that a stabilizing effect may arise upon adding a delay. For example, for synaptically interacting excitatory and inhibitory neuronal populations, there is a stable regime between two unstable regimes for a specific range of the two time delays [137]. Thus, adding further delays can be followed by simpler oscillatory or even fixed point behavior. However, this may not be the general case for all delayed models, such as the Lang-Kobayashi (LK) model of a semiconductor laser with external delayed feedback. Increasing the number of delays in the LK model can lead to a high level of dynamical complexity. However, upon further adding feedback delays, the complexity can drop - sometimes abruptly - as assessed by the decrease in the Kolmogorov-Sinai entropy (KS) and Permutation entropy (PE) [27]. The number of delays required to see this "complexity collapse" depends on the strength of the nonlinear feedback and on the precise manner in which the limit is taken but is generally due to the increased averaging over the chaotic fluctuations of the past states. In the limit of many delays, the resulting simplified dynamics are similar to those seen in distributed delay systems as the memory kernel broadens; such systems have an infinite number of delays and evolve according to an integro-differential system of equations.

This complexity collapse appears to be a fundamental property of a number of nonlinear delay-differential systems with many delays, and this paper is devoted to exploring these properties further using linear and nonlinear properties of the dynamics. Here, we further analyze the high-dimensional chaos and its collapse found recently in the three-variable LK model and the one-variable generalized MG system [27] by focusing on two standard first-order nonlinear delay-differential equations. In particular, we describe how the distribution of discrete delays shapes the dynamics of the multi-delayed DDEs. In Sec. 4.2, we introduce the generalized MG and electro-optic oscillator (EOO) models, extended here to the context of multiple delays. Section 4.3 explains the tools that are used to analyze the complexity of these models. In Sec. 4.4, the dynamical properties are explored as a function of the delay distribution, in particular, by linking linear and nonlinear characteristics of the system. In Section 4.5, we point out how the precise choice of delays may lead to simpler dynamics with less delays and support this notion theoretically. A Discussion then concludes the paper.

4.2 Models

The MG equation models white blood cell production. The generalized MG equation can be described by the following scalar DDE:

$$\frac{dx}{dt} = -x(t) + \frac{b}{M}\sum_{i=1}^{M}\frac{x(t-\tau_i)}{1+x(t-\tau_i)^{10}}\,. \tag{4.1}$$

In this model, $x(t-\tau_i)$ represents the state of x at time delay τ_i, b is the feedback coefficient, and M represents the number of delays. Throughout this paper, we set $b = 2$. Depending on the form of the delay and their values, the MG equation can show different oscillatory and chaotic behaviors, namely, hyperchaotic behavior or the recently described chaotic motion called laminar chaos [138]. When the feedback function is expressed instead in an integro-differential form as an integral over an equally-weighted infinite number of past states, the MG system shows simple oscillatory behavior [16].

The second scalar nonlinear DDE with multiple delayed feedbacks that we study is the EOO model defined as:

$$\frac{dx}{dt} = -x(t) + \frac{\beta}{M}\sum_{i=1}^{M}\sin^2(x(t-\tau_i)+\phi)\,. \tag{4.2}$$

Here, β is a delayed feedback gain, and ϕ is a constant phase offset. Deterministic chaos can arise from this feedback system under a range of feedback strengths and time delays. For a single-delay EOO model, increasing feedback strength β results in higher entropy [139]. And for strong feedback, the estimation of the time delay from the autocorrelation function becomes difficult; i.e., the time delay signature is weak. The parameters used here for Eq. 4.2 are $\beta = 5$, $\phi = \frac{\pi}{4}$.

Note that in both these DDEs, the coefficient of the feedback gain is normalized by the number of delays M in order to preserve the order of magnitude of the total feedback as M is varied.

4.3 Methods

In this section, we present the methods that we used to study the dynamical invariants of these DDEs. We begin with the computation of the Lyapunov exponents (LEs), a standard approach to characterize the chaotic motion from model-generated time series, but a challenging one for delay systems [73, 107]. To approximate the Lyapunov spectrum of DDEs with multiple delays, we extend a method introduced in Ref. [75] to estimate the LEs of the DDEs with a single delay to the system with multiple delays [27].

We consider that there are $m_i + 1$ points lying between the $x(t-\tau_i)$ and $x(t-\tau_{i-1})$ where we assume here that $\tau_{i-1} < \tau_i$; below, the ordering of the delays will use a subscript i that increases uniformly with delay magnitude. These $m_i + 1$ points will be the extrema of a Chebyshev polynomial, and the time corresponding to these points during the interval $[t-\tau_i, t-\tau_{i-1}]$ can be expressed as:

$$\theta_{i,j} = \frac{(\tau_i - \tau_{i-1})}{2} \cos\left(\frac{j\pi}{m_i}\right) - \frac{(\tau_i + \tau_{i-1})}{2}\,, \qquad i = 1, ..., M, \quad j = 0, ..., m_i\,, \tag{4.3}$$

where for $j = 0$ we have $\theta_{i0} = -\tau_{i-1}$, and for $j = m_i$, $\theta_{im_i} = -\tau_i$. The states associated with each of these points can be expressed with Lagrange polynomials u_j, where j is the point number index along this trajectory. The m_i values can be determined by numerically solving [126]:

$$\left(\frac{\tau_1 - \tau_0}{m_1}\right)^{m_1} = \left(\frac{\tau_2 - \tau_1}{m_2}\right)^{m_2} = ... = \left(\frac{\tau_M - \tau_{M-1}}{m_M}\right)^{m_M} \tag{4.4}$$

in such a way that $\sum_{i=1}^{M} m_i = m_t$ and $\tau_0 = 0$. The following equation can be written for Lagrange polynomials along this trajectory

$$U_i(t)(\theta) := \sum_{j=0}^{m_i} u_{j+m_0+...+m_{i-1}}(t) \prod_{\substack{k=0 \\ k\neq j}}^{m_i} \frac{\theta - \theta_{i,k}}{\theta_{i,j} - \theta_{i,k}}\,. \tag{4.5}$$

Here, we consider $m_0 = 0$, and θ is a time variable that is defined over the range $[-\tau_i, -\tau_{i-1}]$ for each Lagrange polynomial U_i. Then the following equations can be derived:

$$\begin{cases} u_0'(t) = f(x(t), x(t-\tau_1), ..., x(t-\tau_M)), \\ \\ u_k'(t) = \sum_{j=0}^{m_t} d_{kj} u_j(t) \qquad\qquad k = 1, ..., m_t \end{cases} \tag{4.6}$$

where $f(x(t), ..., x(t - \tau_M))$ is the right hand side of Eq. 4.1 or 4.2. The d_{kj} are the elements of the Chebyshev differentiation matrix, which is defined further below. We calculate the LEs from the evolution of the state vectors for the linearized differential equations associated with Eq. 4.6:

$$\frac{d\delta u_i}{dt} = A\delta u_i(t) \qquad\qquad i = 0, ..., m_t \tag{4.7}$$

where the Chebyshev differentiation matrix A is defined as:

$$\begin{pmatrix}
\frac{df}{dx} & \cdots & \frac{df}{dx_{\tau_1}} & 0 & \cdots & 0 & \cdots & & \frac{df}{dx_{\tau_M}} \\
d_{1,0} & \cdots & d_{1,m_1} & 0 & \cdots & \vdots & \cdots & & 0 \\
\vdots & \ddots & \vdots & \vdots & \cdots & 0 & \cdots & & \vdots \\
d_{m_1,0} & \cdots & d_{m_1,m_1} & 0 & & \vdots & \cdots & & 0 \\
0 & \cdots & d_{m_1+1,m_1} & \cdots & d_{m_1+1,m_1+m_2} & 0 & \cdots & & 0 \\
\vdots & & \vdots & \ddots & \vdots & \vdots & \cdots & & \vdots \\
0 & \cdots & d_{m_1+m_2,m_1} & \cdots & d_{m_1+m_2,m_1+m_2} & 0 & \cdots & & \vdots \\
\vdots & & & & & \ddots & & & 0 \\
0 & & & & & 0 & d_{m_{tot}-m_M+1,m_{tot}-m_M} & \cdots & d_{m_{tot}-m_M+1,m_{tot}} \\
\vdots & & & & & & \vdots & \ddots & \vdots \\
0 & \cdots & \cdots & \cdots & & 0 & d_{m_{tot},m_{tot}-m_M} & \cdots & d_{m_{tot},m_{tot}}
\end{pmatrix}. \tag{4.8}$$

where $x_{\tau_i} = x(t-\tau_i)$. In the first row of A, the derivatives of Eq. 4.1 or 4.2 with respect to corresponding variable can be used. At each time step, the modified Gram-Schmidt method is used for orthogonalization of the linearized variables state vector [127]. Furthermore, we measured the change in the ratio of the Euclidean distance of all linearized variables at each time step. The LEs can be approximated through repetition of this procedure over a long time series.

We further performed stability analysis of steady states for both models by using DDE-Biftool package [140]. It has been shown that the sum of eigenvalues with a positive real part may be related to the summation of positive LEs [17]. This correspondence will help us characterize different regimes based on the parameters for various numbers of delays and different delay configurations. Finally, we computed the permutation entropy (PE) [80].

It varies between zero for highly predictable behavior and 1 for maximal complexity. The embedding delay was chosen as $\tau_{emb} = \frac{\tau}{h}$ in which h is the integration time step equal to 0.001. This embedding delay will be adjusted such that the delay τ covers the range from 0 to 80, which is sufficient given the two schemes to choose the distribution of delays that we now describe.

4.4 Complexity collapse in multi-delay first-order nonlinear DDEs

In this section, we study the dynamics of DDE models mentioned in Sec. 4.2 as a function of the number of delays. We assume that the distance between the delays is fixed and equal to 0.5. Here, we consider two schemes for choosing delays to show complexity collapse in multi-delay nonlinear DDEs. Note that henceforth, the subscript i is defined in a different manner than in the description of the method to compute LEs. In the first scheme (scheme 1), we construct a discrete delay distribution in a way that keeps the average delay τ_{avg} approximately constant:

$$\begin{cases} \tau_i = \tau_{avg} - (i-1)/2\Delta\tau, & i \;\; odd \\ \\ \tau_i = \tau_{avg} + (i)/2\Delta\tau, & i \;\; even\,. \end{cases} \tag{4.9}$$

Below, we will keep $\tau_{avg} \approx 17$, which is suitable to illustrate the main dynamical behaviors of interest given our choices for the other model parameters. Here, $\Delta\tau$ is the difference between two successive delays, i.e., the “step” in the delay distribution. In order to avoid negative delays, the following condition must be satisfied: $i \leq i_{max} = 2\tau_{avg}/\Delta\tau + 1$.

In the second scheme (scheme 2), we assume that the τ_{avg} increases as more delays are added to the discrete delay distribution as follows:

$$\tau_i = \tau_{min} + (i-1)\Delta\tau\,. \tag{4.10}$$

In this case, the minimum delay τ_{min} is fixed, and $i = 1, ..., M$; for this scheme, we chose this minimal value to be 17 throughout our study. The maximal value is $\tau_{max} = \tau_{min} + (M-1)\Delta\tau$. The comparison of the two schemes is shown in Fig. 4.1 for $M = 21$ and $M = 51$. The ratio R of time delay to intrinsic response time, which is 1 in our models, is relatively large. We note that some properties of first-order single-delay nonlinear DDEs with large R can be understood as a discrete-time mapping of the solution in a given delay interval into the solution in the next delay interval [132,141]. A large ratio R also promotes multi-stability.

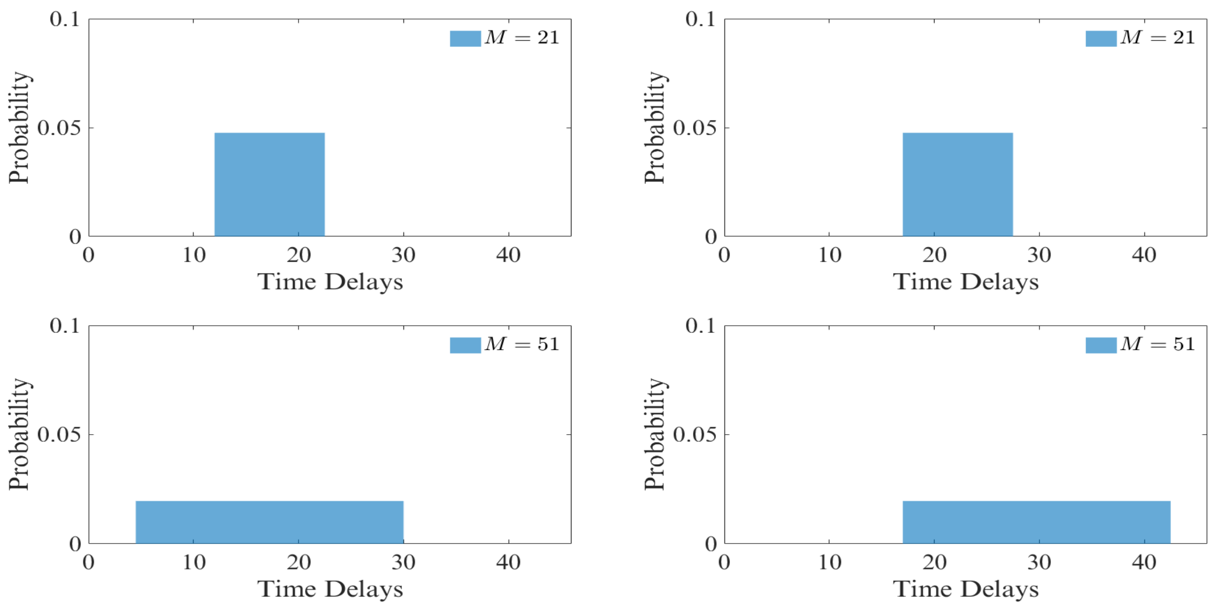

Figure 4.1: Histograms of delays for $M = 21$ delays (first row) and $M = 51$ delays (second row). In the left column, scheme 1 is used with $\tau_{avg} = 17$, and in the right column, scheme 2 is used with $\tau_{min} = 17$. Note that these plots may give the impression that the delays are chosen randomly, which is not the case throughout our study. The continuous blue histograms convey rather how the ranges of delays in the discrete delay distribution change in the two schemes, along with the normalization.

The attractors for both models for numbers of delays $M = 21$ and $M = 51$ with $\tau_{avg} = 17$ are shown in Fig. 4.2. For 21 delays, the generalized MG model has a periodic attractor, while the EOO model is in the chaotic regime. A further increase in the number of delays up to 51 causes the state with the minimum delay to approach the current (i.e., non-delayed) state, and both models have simple oscillatory behavior.

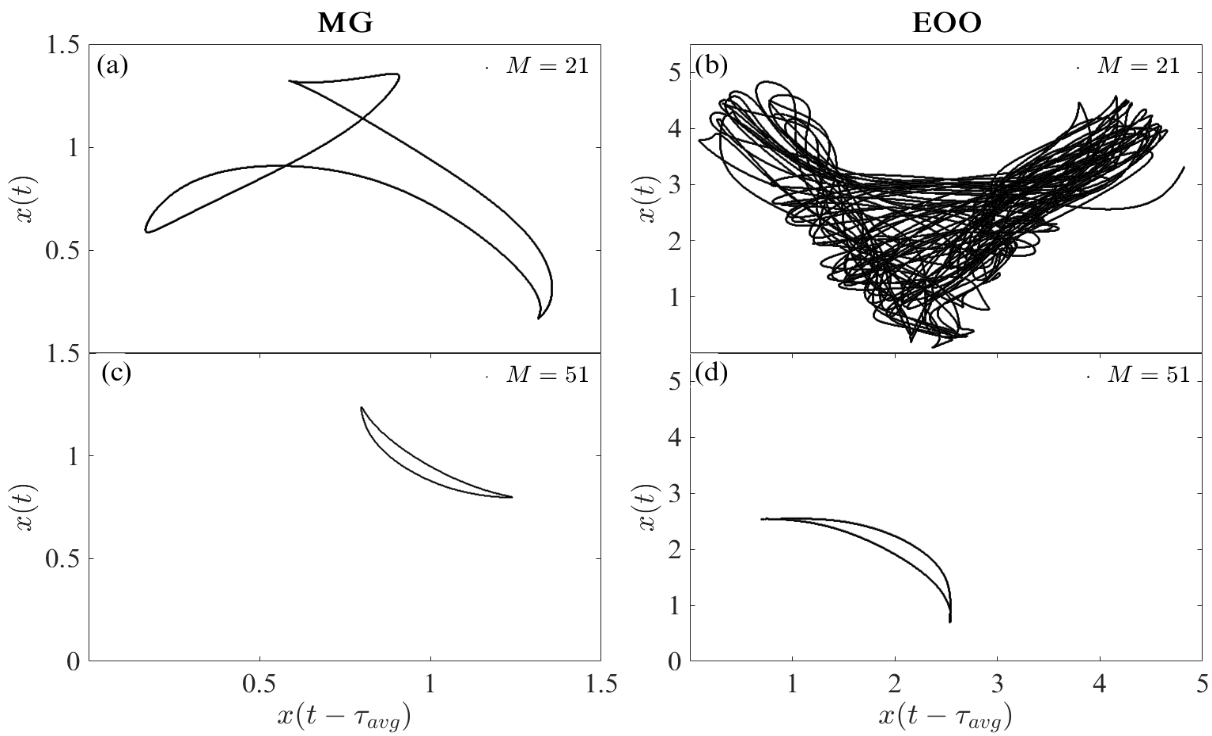

Figure 4.2: Two-dimensional attractor plots $x(t)$ vs $x(t - \tau_{avg})$ for the generalized MG model (left panels) and the EOO model (right panels) for $M = 21$ in (a) and (b) and for $M = 51$ in (c) and (d) when $\tau_{avg} = 17$ (scheme 1). Both these models exhibit chaos when they have a single delay equal to 17.

Information regarding the complexity and time scales of the time series generated by these dynamical systems can be extracted by computing the PE as a function of the scaled embedding delay. This technique has been shown to work for a system of two delays [120], and we extend here to multiple delays. Figure 4.3 provides more insight into the time scales present in these multi-delay dynamics. We first notice for the generalized MG system that the PE quickly climbs up to an asymptotic value, around which it fluctuates; this is characteristic of periodic solutions. That value is slightly smaller for $M = 51$ then $M = 21$, which means decreased complexity. We also note pronounced minima around one and two times the average time delay for $M = 51$. For the generalized MG system with 21 delays, minima can be seen around $\tau = 25$, as well as around two and three times this value. For the EOO model, there is a local minimum around the average time delay.

Due to the chaotic behavior of the EOO model for 21 delays, a higher entropy is obtained (Fig. 4.3(b)). The time scale governing the dynamics for $M = 51$ for these models is less obvious from this PE plot. It can nevertheless be seen that the local minimum around the average of the delays for 21 delays is shifted to around $2\tau_{avg}$, along with a small dip at τ_{avg}.

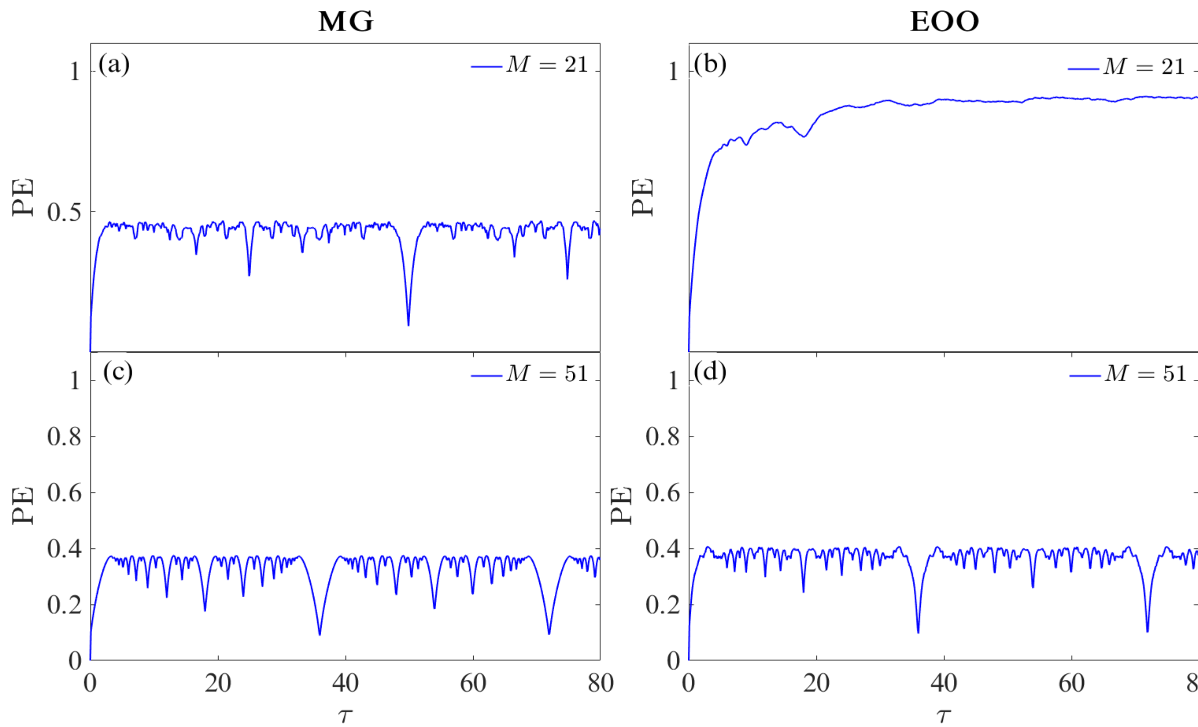

Figure 4.3: Permutation entropy of a generalized MG model (left panel) and EOO model (right panel) vs the scaled embedding delay ($\tau = \tau_{emb} \times h$ with τ_{emb} varying from 0 to 80,000) when τ_{avg} is fixed at 17 (scheme 1) and $\Delta\tau = 0.5$ for $M = 21$ in (a) and (b) and $M = 51$ in (c) and (d).

Next, we consider scheme 2 where τ_{avg} is increasing, while the minimum delay is fixed at $\tau_{min} = 17$, regardless of the number of delays. The corresponding attractor plots for

$M = 21$ and $M = 51$ are presented in Fig. 4.4. In contrast to the previous scheme, for 21 delays, both models now exhibit chaotic behavior. This is likely due in part to the increase in the mean delay compared to scheme 1, following the intuition that larger delays promote chaos in single-delay systems. Increasing M to 51 clearly reduces the complexity for the generalized MG model, and the same appears to occur for the EOO model. We should note that the change of dynamic behavior due to the number of delays strongly depends on $\Delta\tau$ for both delay configuration schemes. Our simulations reveal that for $\Delta\tau$ smaller than the value of 0.5 chosen here, a larger number of delays is needed to observe the complexity collapse (not shown), pointing to the necessity of having a sufficiently broad delay kernel to see simpler behavior. In both schemes for large M, a stable fixed point can be expected for both the generalized MG and EOO models.

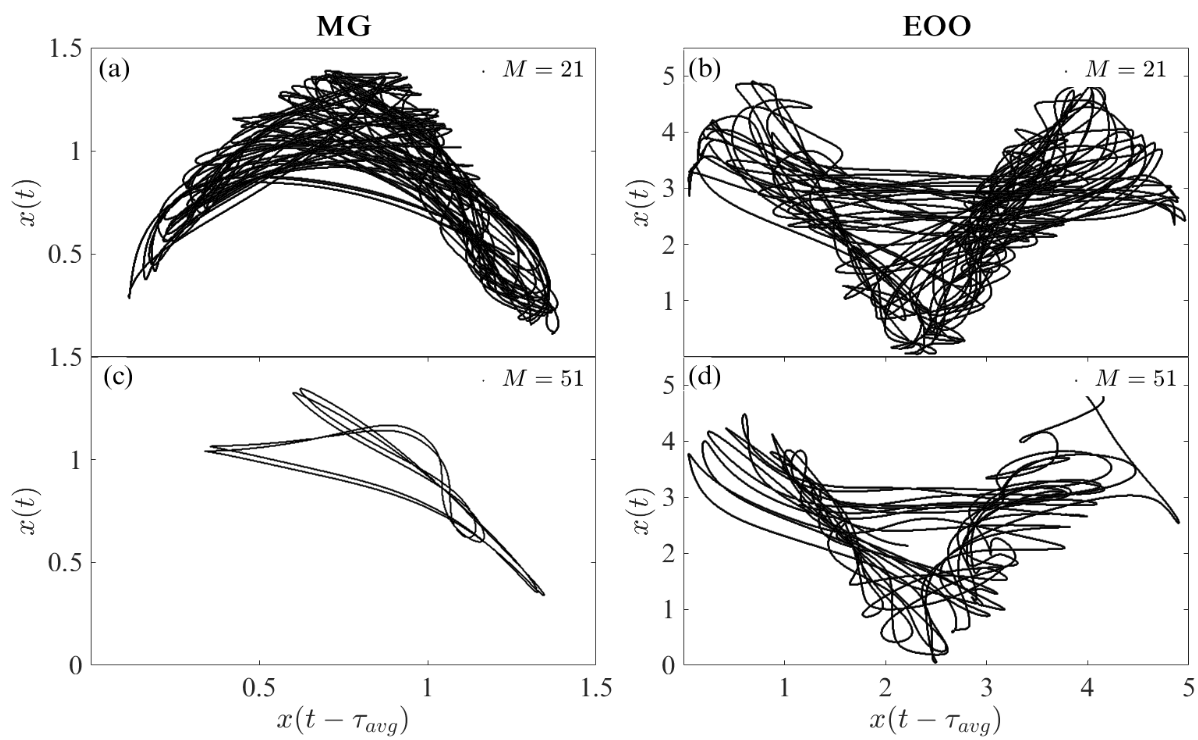

Figure 4.4: Attractor plots $x(t)$ vs $x(t-\tau_{avg})$ for the generalized MG model (left) and the EOO model (right) for $M = 21$ in (a) and (b) and $M = 51$ in (c) and (d) with $\tau_{min} = 17$. In this scheme 2, the average delay τ_{avg} of the delayed feedback term increases with M. The spacing between delays is $\Delta\tau = 0.5$.

The PEs corresponding to the dynamics with scheme 2 in Fig. 4.4 are shown in Fig. 4.5. When $M = 21$, a minimum can be detected for both the generalized MG and EOO models around τ_{avg} (Figs. 4.4(a) and 4.4(b)), but it is not as sharp as those seen in Fig. 4.3. When M increases to 51, the PE decreases for both models; shallow minima are seen around different times, and it is not clear what time scales govern those dips.

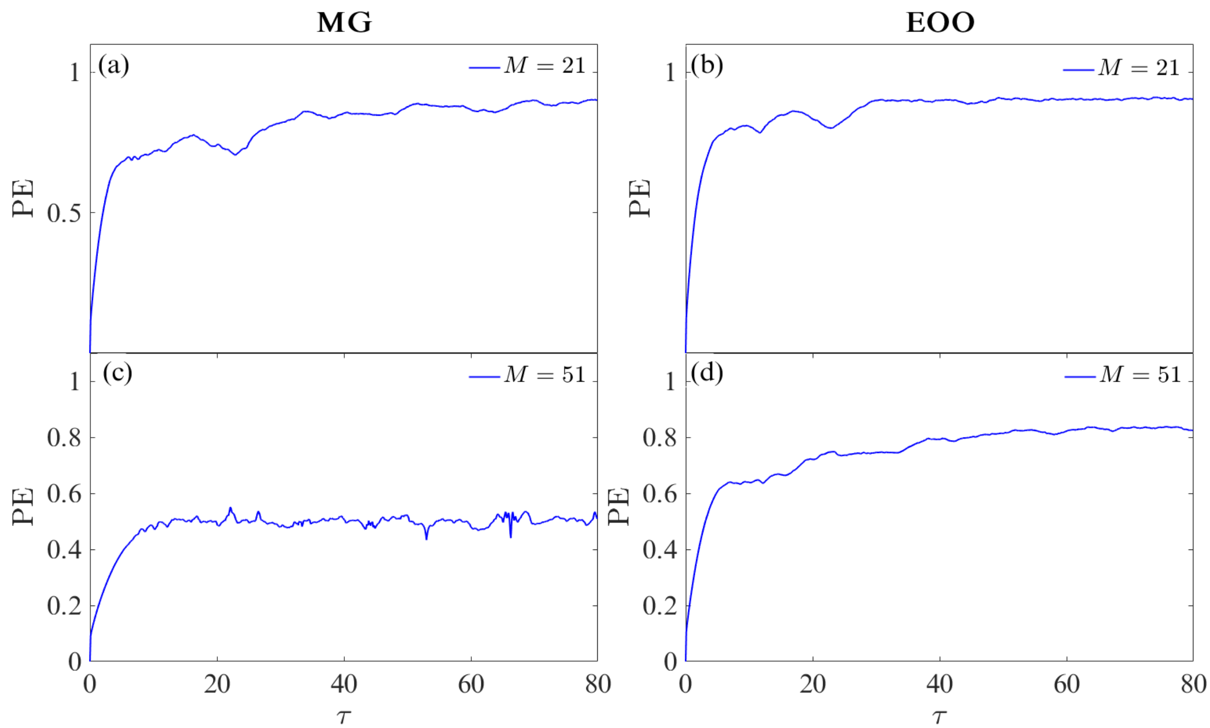

Figure 4.5: Permutation entropy of the generalized MG model (left panel) and the EOO model (right panel) vs the scaled embedding delay when $\tau_{min} = 17$ is fixed (scheme 2) and $\Delta\tau = 0.5$. The average delay τ_{avg} thus increases in going from $M = 21$ in (a) and (b) to $M = 51$ in (c) and (d), which is accompanied by a drop in complexity for both models. For these plots, τ is the multiplication of embedding delay by the integration time step.

In scheme 1 where τ_{avg} is constant, we notice that when the average delay is larger, a broader width of the delay distribution is needed in order to obtain a complexity collapse. Similarly, in scheme 2 where τ_{min} is constant, a larger value of τ_{min} requires a larger τ_{avg} to see collapse. Furthermore, these multi-delayed DDEs actually often exhibit *transient* *chaos*, and the periodic attractors are only seen after long transients have decayed (not shown).

To gain more insight into the dynamical behavior of these DDEs as M increases, we calculate the mean and standard deviation (SD) of the feedback term. It is known for the LK model with multiple delays that the mean and SD of the feedback decrease as M increases for fixed feedback strength; the probability density of this feedback becomes multi-modal after complexity collapse [27]. The mean and SD of the generalized MG and EOO model's feedback term are plotted vs M in Fig. 4.6. The "normalized" forms for the means and SDs are shown, which include the $1/M$ prefactor as in their defining dynamics.

We first note that the normalized means are of $O(1)$ across the large range of M that is explored. In other words, the feedback term does not vanish in the limit of large M. The means of the unnormalized feedback terms increase monotonically (not shown). However, the normalized SD drops monotonically when M increases beyond ~ 30 for the generalized MG model and ~ 37 for the EOO model in scheme 1. This SD also exhibits brief dips prior to these values of M - an effect that is linked to the periodic windows in the bifurcation diagrams, as we will see below. Thus, increasing M leads to an averaging that produces smaller chaotic fluctuations that drive the present time dynamics. Eventually, the SD goes to zero in both models in scheme 1 as the dynamics collapse onto a stable fixed point.

Although a slow decrease of the mean with M is seen in the EOO, the behavior of the mean and SD in both these models differs markedly from that for the LK model, where the mean and SD decrease drastically with M - in other words, the feedback term in LK essentially vanishes in the large M limit. This is a consequence of the fact that the feedback in the LK model is then a sum of complex exponentials with approximately random phases multiplied by the $1/M$ prefactor, making the whole feedback term tend toward zero [27]. The probability density of the feedback term for both the generalized MG and EOO models will also become multi-modal when periodic attractors occur at larger M (see below), as was the case for the LK model.

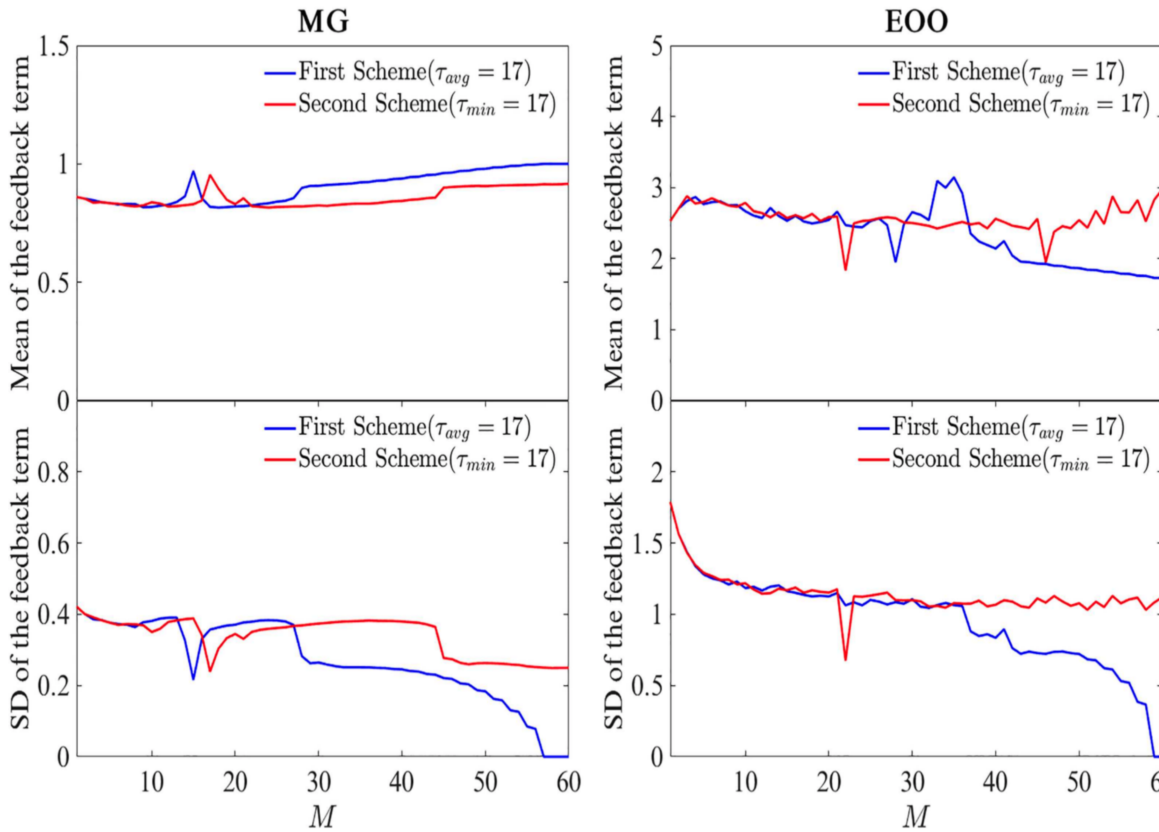

Figure 4.6: Mean (first row) and SD (second row) of the total feedback as a function of the number of discrete delays M for both the generalized MG model (left panels) and the EOO model (right panels). Results are shown for both schemes, i.e., with fixed mean delay (scheme 1 labeled "τ_{avg}") and varying mean delay but fixed minimal delay (scheme 2 labeled "τ_{min}"). Note that in scheme 1, the SD goes to zero when M passes a threshold; this indicates fixed point dynamics.

Employing the method described in Sect. 4.2, we calculate the four largest LEs for both the fixed τ_{avg} and increasing τ_{avg} schemes. This measurement helps us gauge the chaotic behavior for multi-delay DDEs as the number of delays increases. Figure 4.7 illustrates that when τ_{avg} is approximately constant, the LEs generally decrease. For the generalized MG model, this occurs rather sharply and at a smaller M compared to the EOO model. When the minimum delay is kept fixed as larger delays are added (bottom row of Fig. 4.7), the generalized MG model still shows the complexity collapse. Although the EOO model still has chaotic properties, the maximum LE decreases for an increasing number of delays, and other LEs become non-positive after $M = 40$.

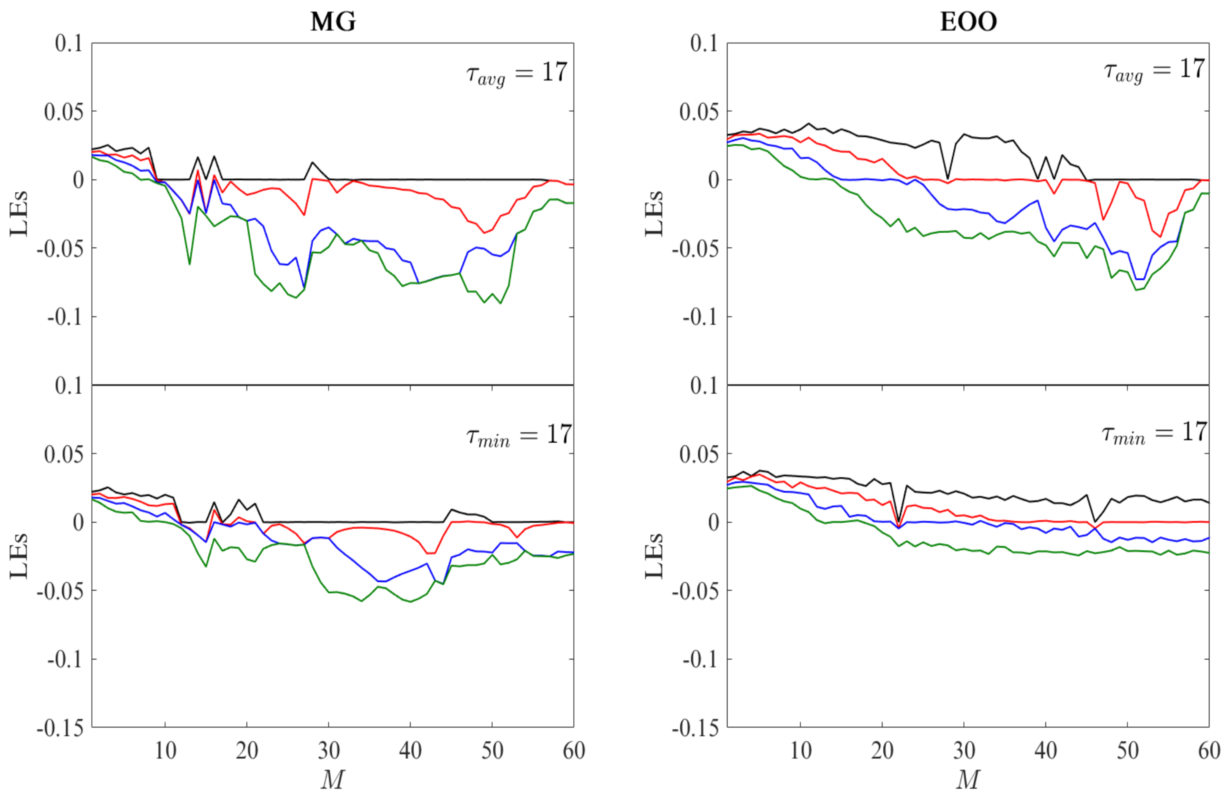

Figure 4.7: Four largest LEs of the generalized MG model (left panels) and the EOO model (right panels) as a function of the number of delays M when τ_{avg} is approximately 17 (scheme 1: first row) and τ_{min} is fixed at 17 (scheme 2: second row). The LEs are plotted in decreasing order with the corresponding colors black, red, blue, and green. Note the general trend where the dynamics start as hyperchaotic but eventually become periodic at sufficiently large M. Such periodic behavior is actually prominent even for moderate M in the case of the generalized MG model for both delay distribution schemes.

4.5 Effect of a delay distribuiton

Up until now, we observed that complexity collapse occurs no matter how the delays are picked as the number of delays increases. For the rest of the paper, we assume that the average of the delays can change (scheme 2) and in fact acts as a bifurcation parameter. For a fixed number of delays M, increasing τ_{avg} amounts to increasing the spacing between delays in the delay distribution and decreasing the delay density.

4.5.1 Mackey-Glass Model

We begin by plotting the bifurcation diagram for the generalized MG model. Local minima and maxima can be seen in Fig. 4.8 where simulations are carried out for $M = 10, 25, 50$ and 100 delays. The minimum delay in all cases is 17, but we varied the size of the spacing $\Delta\tau$ between delays. All plots span the same range of a τ_{avg} values. Thus, for a given value of M, increasing τ_{avg} means proportionally increasing the delay spacing, and the density of delays per unit time is smaller (sparse delay distribution). For a given value of τ_{avg}, the delay spacing is inversely proportional to M such that at higher M, the density of delays per unit time is higher. This is an alternative version of scheme 2.

For ten delays, the system exhibits different dynamical behaviors as M increases. The chaotic dynamics turns into a periodic attractor after increasing τ_{avg} to around 19. For $\tau_{avg} > 19$, there is an alternation of periodic and chaotic windows. For $M = 25$, most of the chaotic windows disappear and are replaced by limit cycles. However, a chaotic regime appears again in a narrow range between $\tau_{avg} = 95$ and $\tau_{avg} = 100$. A prevalence of simple dynamics can be seen when $M = 50$, where no chaotic behavior can be observed at values of τ_{avg} larger than approximately 30, after which only limit cycle or stable fixed point behavior are expected. In the presence of 100 delays, more simplification occurs for $\tau_{avg} > 75$ where the local maxima and minima get closer to each other, and eventually, the limit cycle bifurcates to a fixed point.

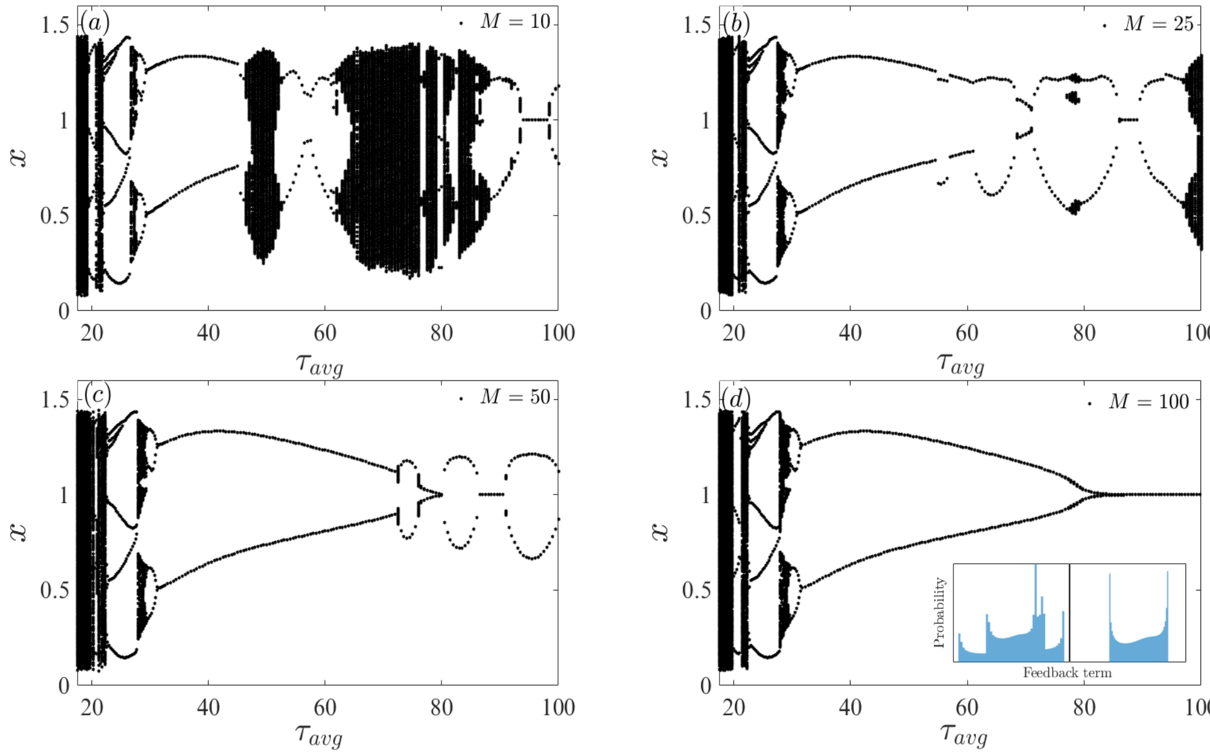

Figure 4.8: Bifurcation diagram in the generalized MG equation for (a) $M = 10$, (b) $M = 25$, (c) $M = 50$, and (d) $M = 100$ when the τ_{max} and $\Delta\tau$ are increasing and the τ_{min} is fixed at 17 (alternative version of scheme 2). Thus, a smaller value of M corresponds to a larger value of $\Delta\tau$, i.e., a bigger spacing between the delays or a smaller "density of delays" on the real axis. The points represent the local extrema in the solution. Hence, a fixed point appears as one value, and a bifurcation to a simple limit cycle produces two values. Insets in panel (d) depict the histogram of the feedback term just to the left ($\tau_{avg} = 30$) and right ($\tau_{avg} = 32$) sides of the inverse period-doubling bifurcation, respectively.

In Fig. 4.9 the mean and SD of the feedback term corresponding to the bifurcation diagrams in Fig. 4.8 are plotted. For the different numbers of delays, we do not see a significant difference in τ_{avg} between 17.5 and 45 in the feedback behavior. When τ_{avg} is larger, we notice abrupt drops in the mean and an increase in SD; but they tend to disappear when the number of delays increases such that for $M = 100$, the mean approaches the fixed point value and the SD approaches zero.

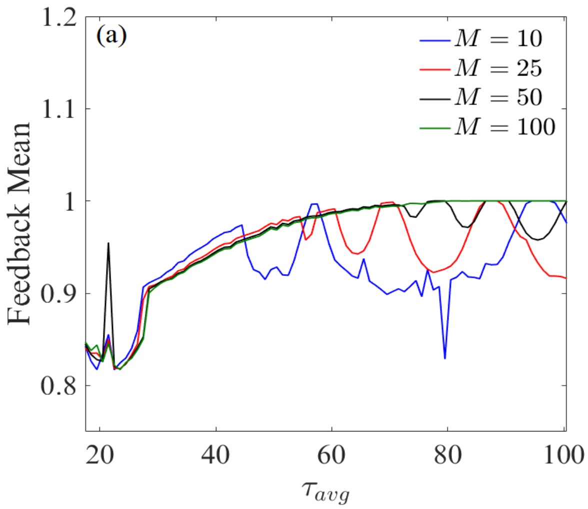

Figure 4.9: Mean of the feedback term (a) and SD of the feedback term (b) for different numbers of delays vs the increasing τ_{avg} (scheme 2).

The four largest LEs are illustrated in Fig. 4.10. At low τ_{avg}, all four LEs are positive, and for any choice of the number of delays, the system displays hyperchaotic behavior. For $M = 10$ and $M = 25$, LEs then go negative for a while, but chaos and even hyperchaos appear again over specific ranges of τ_{avg}. However, their value is not as high as for the low τ_{avg} values, and there are at most three positive LEs. These τ_{avg} regimes with positive LEs are in agreement with the bifurcation plot depicted in Fig. 4.8. For $M = 50$ and $M = 100$, the LEs converge and join up near zero at large values of τ_{avg}. In all cases, the LE values at larger $\Delta\tau$ are much smaller than for the higher delay densities obtained for lower values of the delay spacing. The general trend of LEs of multi-delay MG model for various $\Delta\tau$ implies that the larger the spacing between delays is, the less sensitive the dynamics is to the initial conditions.

Next, we performed a linear stability analysis around the fixed point using the DDE-Biftool software package [140]. The stability analysis was done only for $M = 50$, here at the steady-state $x^* = 1$. Figure 4.11 illustrates the numerically calculated eigenvalue spectrum for different values of τ_{avg}. One can see that for highly dense delays, i.e., when $\Delta\tau$ is small, there are several eigenvalues with a positive real part. As $\Delta\tau$ increases, more

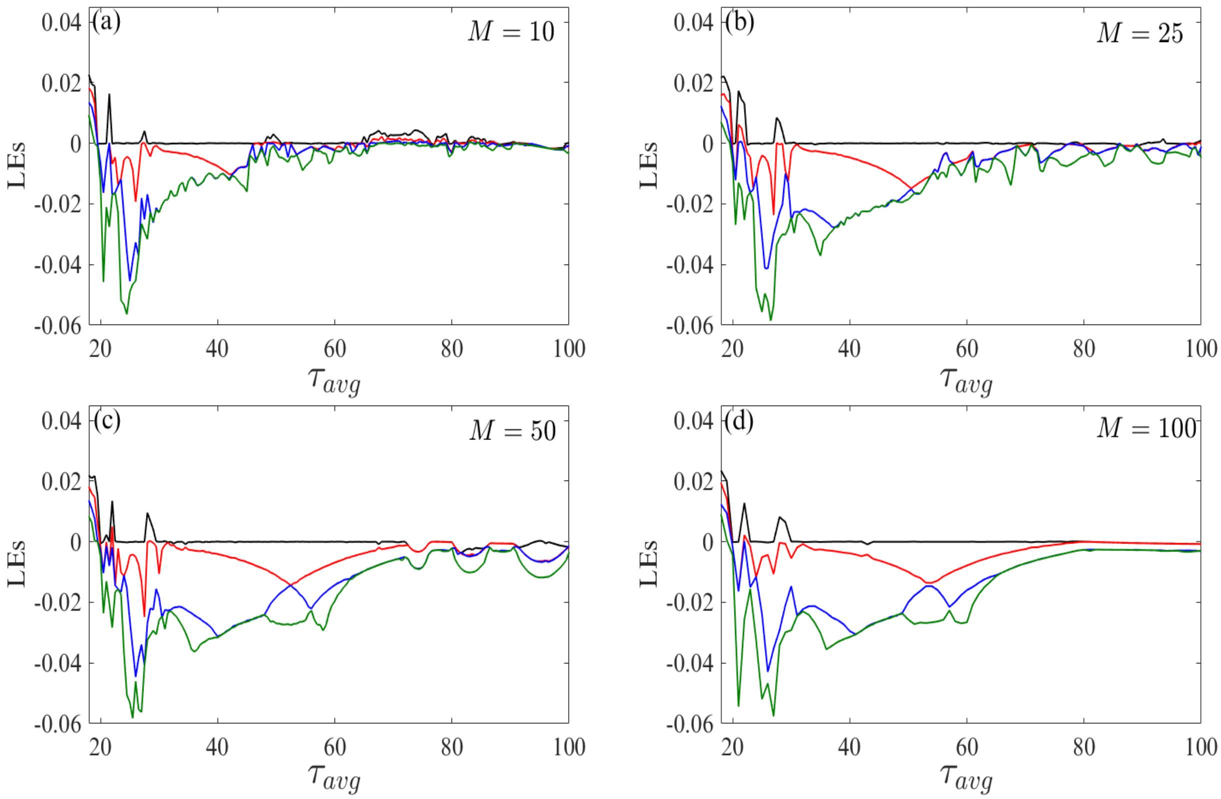

Figure 4.10: Four largest Lyapunov exponents of the generalized MG equation for (a) $M = 10$, (b) $M = 25$, (c) $M = 50$, and (d) $M = 100$ as the average delay τ_{avg} increases, i.e., as the spacing between delays $\Delta\tau$ increases or the density of delays decreases (alternative version of scheme 2). The LEs are plotted in decreasing order with the corresponding colors black, red, blue, and green. The chaotic windows seen in Fig. 4.8 clearly correspond to the positive excursions of at least one LE.

roots with a negative real part appear and the positive ones also start to move toward the negative axis. This change in the distribution profile of the roots continues as $\Delta\tau$ increases to the point where there appears to be no roots with a positive real part. However, we can see that there are two roots with very small real parts for $\tau_{avg} = 80$ and $\tau_{avg} = 100$ (Figs. 4.11 (h) and (i)), which correspond to the limit cycles shown in the bifurcation plot (Fig. 4.8(c)).

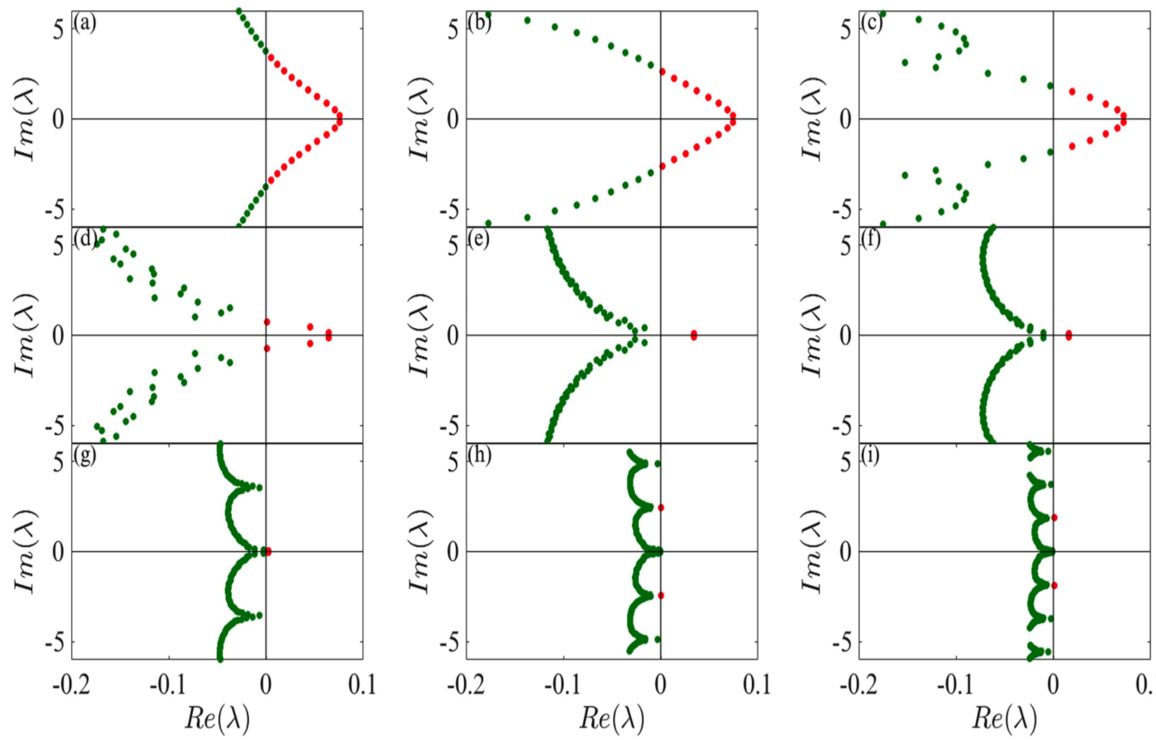

Figure 4.11: Roots of a characteristic equation of the generalized MG model for (a) $\tau_{avg} = 17.1$, (b) $\tau_{avg} = 17.5$, (c) $\tau_{avg} = 18$, (d) $\tau_{avg} = 20$, (e) $\tau_{avg} = 30$, (f) $\tau_{avg} = 40$, (g) $\tau_{avg} = 60$, (h) $\tau_{avg} = 80$, and (i) $\tau_{avg} = 100$ in scheme 2 with $\tau_{min} = 17$.

In the following, we explore more deeply the behavior of the characteristic roots. In general, first-order nonlinear DDEs with multiple delays can be written as

$$\frac{dx}{dt} = -x(t) + \sum_{j=1}^{M} \frac{F(x(t-\tau_j))}{M}\,. \tag{4.11}$$

The corresponding characteristic equation is

$$\Delta(\lambda) = -\lambda - 1 + \frac{F'(x^*)}{M} \sum_{j=1}^{M} e^{-\lambda\tau_j}, \tag{4.12}$$

where $\lambda = \mu + i\omega$. Separating Eq. 4.12 into its real and imaginary parts gives the following two equations:

$$\frac{\mu+1}{F'(x^*)} = \frac{e^{-\mu\tau_{min}}}{M}\sum_{j=1}^{M} e^{-\mu(j-1)\Delta\tau}\cos(\omega(\tau_{min}+(j-1)\Delta\tau)) \tag{4.13}$$

$$-\frac{\omega}{F'(x^*)} = \frac{e^{-\mu\tau_{min}}}{M}\sum_{j=1}^{M} e^{-\mu(j-1)\Delta\tau}\sin(\omega(\tau_{min}+(j-1)\Delta\tau))\,. \tag{4.14}$$

In the limit where the number of delays M tends to infinity and the space between delays is sufficiently small, we can approximate Eqs. 4.13 and 4.14 by the integral forms,

$$\frac{\mu+1}{F'(x^*)} \approx \frac{e^{-\mu\tau_{min}}}{T_M+\Delta\tau}\int_0^{T_M} e^{-\mu\tau'}\cos(\omega(\tau_{min}+\tau'))d\tau' \tag{4.15}$$

$$-\frac{\omega}{F'(x^*)} \approx \frac{e^{-\mu\tau_{min}}}{T_M+\Delta\tau}\int_0^{T_M} e^{-\mu\tau'}\sin(\omega(\tau_{min}+\tau'))d\tau' \tag{4.16}$$

where $T_M = (M-1)\Delta\tau = \tau_{max} - \tau_{min}$ is the span of delays in the delay distribution. Performing the integrations yields

$$\begin{aligned}\frac{\mu+1}{F'(x^*)} =& \frac{e^{-\mu\tau_{min}}}{(\omega^2+\mu^2)(T_M+\Delta\tau)} \\ &\times\Bigg\{\omega\Big[e^{-\mu T_M}\sin(\omega(\tau_{min}+T_M)) - \sin(\omega\tau_{min})\Big] \\ &+\mu\Big[\cos(\omega\tau_{min}) - e^{-\mu T_M}\cos(\omega(\tau_{min}+T_M))\Big]\Bigg\}\end{aligned} \tag{4.17}$$

$$\begin{aligned}-\frac{\omega}{F'(x^*)} =& \frac{e^{-\mu\tau_{min}}}{(\omega^2+\mu^2)(T_M+\Delta\tau)} \\ &\times\Bigg\{\omega\Big[\cos(\omega\tau_{min}) - e^{-\mu T_M}\cos(\omega(\tau_{min}+T_M))\Big] \\ &+\mu\Big[\sin(\omega\tau_{min}) - e^{-\mu T_M}\sin(\omega(\tau_{min}+T_M))\Big]\Bigg\}\end{aligned} \tag{4.18}$$

The space between delays $\Delta\tau$ is much smaller than T_M; therefore, it can be ignored. Equations 4.17 and 4.18 can be further simplified by ignoring their second term on the right-hand side as well as the μ^2 in the denominator, in which case the final equations read:

$$\frac{\mu+1}{F'(x^*)} = \frac{e^{-\mu\tau_{min}}\Big[e^{-\mu T_M}\sin(\omega(\tau_{min}+T_M)) - \sin(\omega\tau_{min})\Big]}{\omega T_M} \tag{4.19}$$

$$\frac{-\omega}{F'(x^*)} = \frac{e^{-\mu\tau_{min}}\Big[\cos(\omega\tau_{min}) - e^{-\mu T_m}\cos(\omega(\tau_{min}+T_m))\Big]}{\omega T_m} \tag{4.20}$$

The justification for the assumption that μ is small comes from Fig. 4.11 where it is seen to become smaller as the delay span $T_M = \tau_{max} - \tau_{min}$ increases. At first glance, we infer from Eq. 4.19 that the right-hand side of the equation for larger T_m approaches zero, while the left-hand side is always negative for positive μ and the maximum value that it can take is $\frac{1}{F'(x^*)}$. Similarly, this is true for multiple discrete delays in Eq. 4.13 when M is increasing.

We use Eqs. 4.19 and 4.20 for the MG model by subtracting their left and right sides as a function of μ and ω when the steady-state is $x^* = 1$ and $F'(x^*) = -4$. We rewrite Eq. 4.19 for the real part as $f(\mu,\omega) = 0$ and Eq. 4.20 for the imaginary part as $g(\mu,\omega) = 0$. The color plots of these functions are shown in Fig. 4.12 for three values of the average delay: $\tau_{avg} = 20$, $\tau_{avg} = 60$, and $\tau_{avg} = 100$ for $T_M = 6$, $T_M = 86$, and $T_M = 166$, respectively. To locate the roots of the characteristic equation, we also plotted the norm $H(\mu,\omega) = \sqrt{f(\mu,\omega)^2 + g(\mu,\omega)^2}$ in the third column; a value of $H(\mu,\omega)$ very close to zero implies that there is a characteristic root at (μ,ω). For $\tau_{avg} = 20$, there exist separate regions in $f(\mu,\omega)$ and $g(\mu,\omega)$ that become zero, i.e., no overlapping regions close to zero as required to have a root. Those roots were found to be in excellent agreement with those obtained by applying DDE-BIFTOOL to the original generalized MG system with large M and relatively small spacing between delays. The combination of our theory and Fig. 4.12 thus reveals that, by increasing the width of the delay distribution, the probability of finding roots with a positive real part decreases, especially for $f(\mu,\omega)$. Hence, as the number of delays and/or the spacing between delays increases, the roots move toward

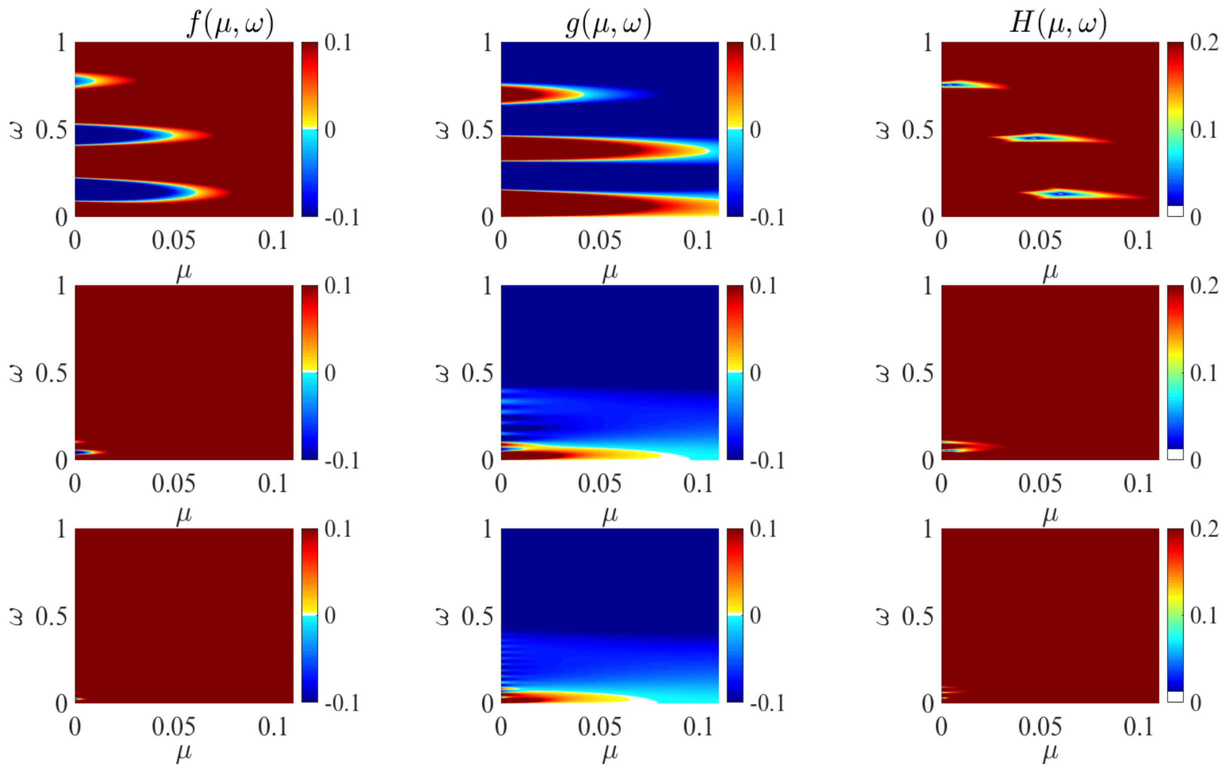

Figure 4.12: Real part $f(\mu,\omega)$) (first column) and imaginary part $g(\mu,\omega)$ (second column) of the characteristic equation, along with the norm $\sqrt{f(\mu,\omega)^2+g(\mu,\omega)^2}$ for $\tau_{avg}=20$ (first row), $\tau_{avg}=60$ (second row), and $\tau_{avg}=100$ (third row).

stability, a trend that underlies the complexity collapse.

Last, we compare the general trend of the characteristic roots to the behavior of the LEs. It has been shown that, for a large ratio of the time delay to the system's time response, the KS entropy (the sum of all the positive LEs) agrees approximately with the sum of the real parts of eigenvalues with a positive sign [17]. It can be seen in Fig. 4.13 that the KS entropy decreases as the spacing between delays increases. A similar trend can be observed for the sum of the positive real parts of the eigenvalues. The latter sum roughly follows the outline of the peaks of the LEs.

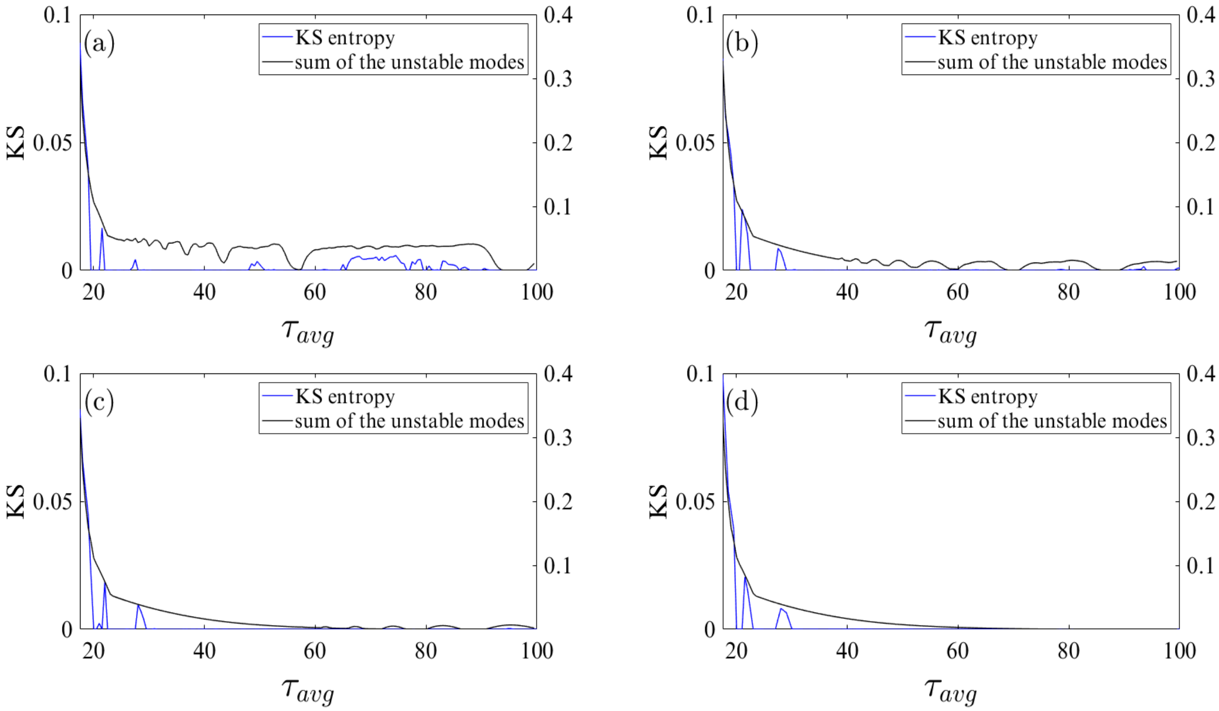

Figure 4.13: KS entropy (left y-axis) and the sum of positive real parts of eigenvalues with $\omega > 0$ (right y-axis) for the generalized MG model as a function of τ_{avg} for (a) $M = 10$, (b) $M = 25$, (c) $M = 50$, and (d) $M = 100$ (scheme 2).

4.5.2 Electro-Optic Oscillator Model

Next, we performed the same numerical investigations on the EOO model. The bifurcation plot is shown in Fig. 4.14. We observe a general simplifying trend with increasing M that is similar to the one for the generalized MG system in Fig. 4.8. For $M = 10$, increasing $\Delta\tau$ generally modifies the local maxima and minima's behavior in the bifurcation plot. There are chaotic regimes that appear for a specific range of τ_{avg}. The system dynamics reaches a stable fixed point between $\tau_{avg} = 90$ and $\tau_{avg} = 95$, and then it is followed by a limit cycle.

Increasing M to 25, the chaotic windows become tighter and smaller, and they occur at larger τ_{avg} compared to the $M = 10$ case. Further increasing the number of delays up to $M = 50$ replaces the recurring chaotic windows by limit cycles. For $M = 100$,

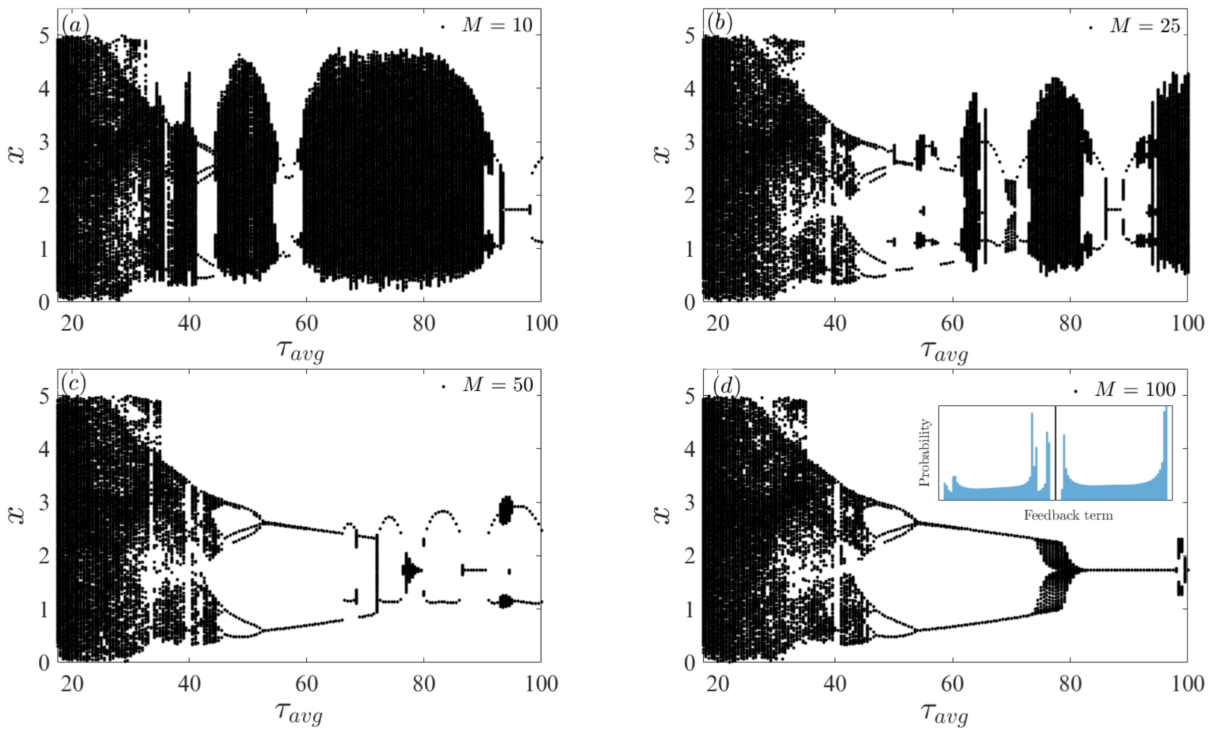

Figure 4.14: Bifurcation diagram in the EOO equation for (a) $M = 10$, (b) $M = 25$, (c) $M = 50$, and (d) $M = 100$ when the τ_{max} and $\Delta\tau$ are increasing and $\tau_{min} = 17$ (alternative version of scheme 2). The histograms of the feedback term just to the left ($\tau_{avg} = 52$) and right ($\tau_{avg} = 54$) sides of the inverse period-doubling bifurcation are shown in the insets of panel (d).

dynamics become even much simpler since for $\tau_{avg} > 80$, oscillations completely disappear and dynamics bifurcates to a stable fixed point. However, there is a periodic attractor regime again for $\tau_{avg} > 97$; our simulations indicate that those oscillations would disappear for a larger M (not shown). It should be noted that the bifurcation plot for all M up to $\tau_{avg} \approx 40$ shows qualitatively similar results.

Figure 4.15 shows the LEs of the multi-delayed EOO model for different τ_{avg} in scheme 2. When $M = 10$, increasing τ_{avg} (and thus the spacing $\Delta\tau$) decreases the maximum LE. Also, other LEs start to take on negative values. As seen in the bifurcation plot, some regimes show chaotic behavior. This can be seen in LEs as well, and it is also possible in

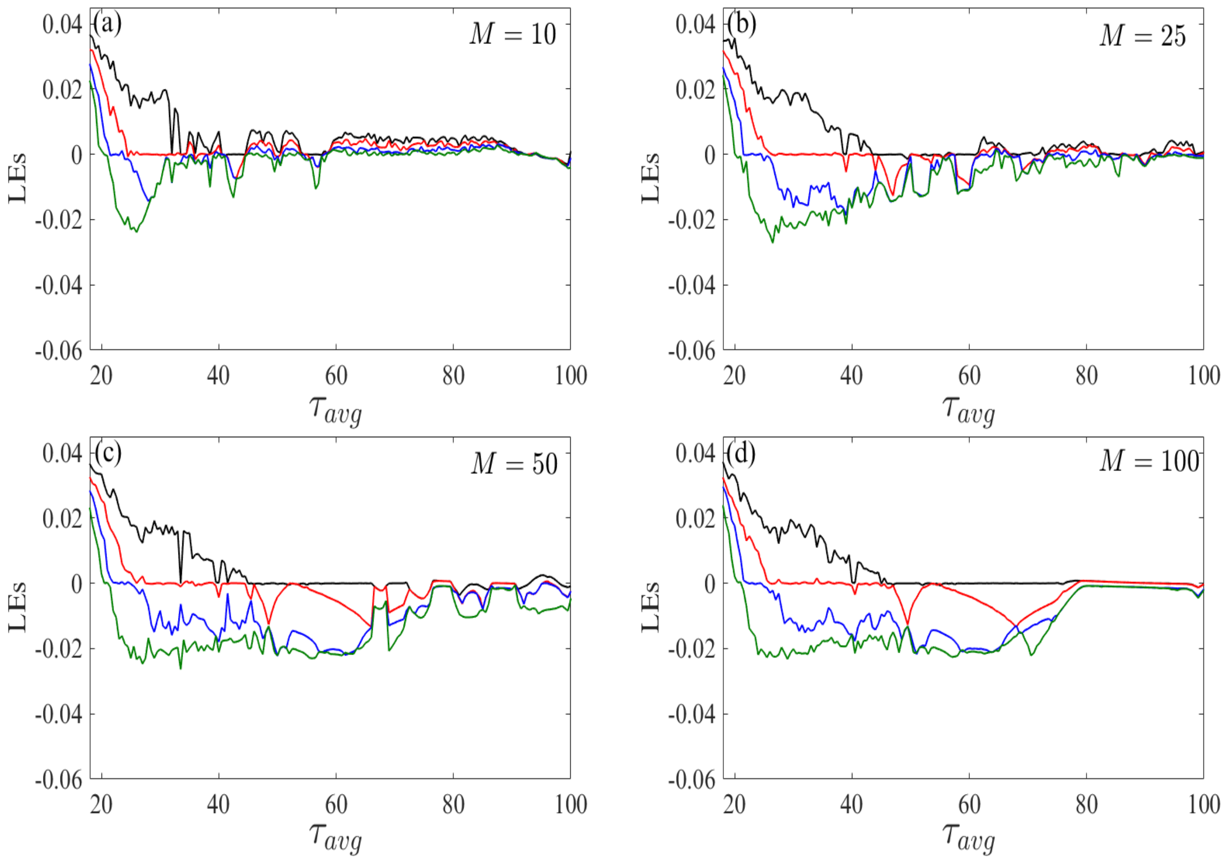

Figure 4.15: Four largest LEs of the EOO model for (a) $M = 10$, (b) $M = 25$, (c) $M = 50$, and (d) $M = 100$ as the spacing $\Delta\tau$ between delays is increasing and $\tau_{min} = 17$ (alternative scheme 2).

hyperchaotic behavior. However, the value of the LEs is much smaller compared to those for small τ_{avg}. For larger M, the LEs continue to behave in a qualitatively similar manner for $\tau_{avg} < 40$. However, for $\tau_{avg} > 40$, the LEs for the chaotic windows in the case of $M = 10$ decrease in value, up to a point where there are no longer any positive LEs. For all values of M, the LEs show convergence at large spacings.

Other dynamical invariant measurements, such as the eigenvalues and KS entropy, are pretty much in line with the generalized MG model's results (not shown). There is a slight difference due to higher nonlinearity in the EOO model such that the KS entropy is larger, and also, the characteristic equation has fewer more positive roots in most chaotic regions. However, the qualitative trend as a function of the difference between the delays for a different number of delays is quite similar.

4.6 Phase diagrams

Since the sum of the positive real parts of eigenvalues shows similar trends to the KS entropy in both models, it is less computationally intensive to construct an approximate phase diagram of system behavior by calculating the eigenvalues with DDE-BIFTOOL [140]. This would allow us to determine what to expect from given parameters. Usually, these stability diagrams are constructed by finding the domains where the roots of the characteristic equations are purely imaginary or their real part is positive [12, 142]. Here, we plotted the sum of the positive real parts of eigenvalues for different number of delays M and average delays τ_{avg} in Fig. 4.16 for both the EOO and generalized MG models. Dark blue regions represent where a stable fixed point or very low complexity behavior expected, while dark red regions correspond to expected hyperchaotic regimes. It can be seen that for any number of delays, at low τ_{avg} or low spacing (higher delay density), chaotic and highly unpredictable behavior is expected. As τ_{avg} increases, simpler dynamics appear. For $\tau_{avg} > 50$ and $M > 40$ in the case of the generalized MG model and for $\tau_{avg} > 55$ and $M > 55$ for the EOO model, the blue regions in fact occupy the whole space.

In order to better characterize the dynamical regimes, we introduce the time delay density for multi-delay systems with the following formula:

$$D = \frac{M}{(M-1)\Delta\tau} \,. \tag{4.21}$$

This formula is simply the number of delays divided by the range of delays, and becomes independent of M for large M. The dependency of the dynamics of these models on D and M is shown in the $M - D$ phase diagrams of Fig. 4.17. The same eigenvalue-based proxy for system complexity as in Fig. 4.16 is used for the computations. We can conclude from Fig. 4.17 that lower delay densities, obtained e.g., by increasing the spacing between

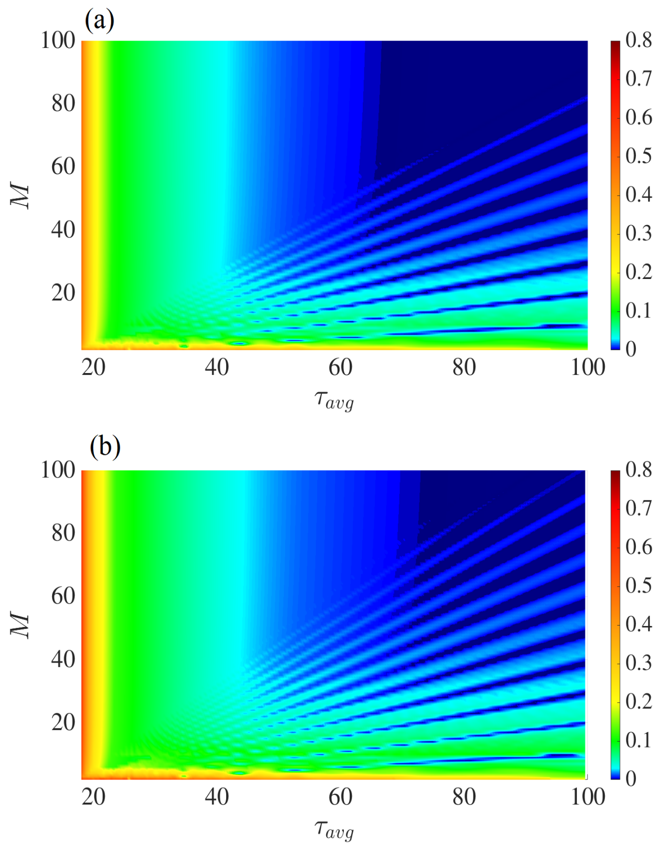

Figure 4.16: $M - \tau_{avg}$ phase diagrams obtained by computing the sum of the positive real parts of the eigenvalues for the (a) generalized MG and (b) EOO models. Scheme 2 is implemented with $\tau_{min} = 17$. The darkest blue color corresponds to stable fixed point or very low complexity behavior.

delays, is associated with simpler dynamics. This is in line with the right parts of the bifurcation diagrams in Figs. 4.8 and 4.14, as well as the behavior of the LEs (Figs. 4.10 and 4.15) and KS entropies (Fig. 4.13) at large τ_{avg}. Conversely, high delay densities imply a higher degree of chaos and entropy. *Thus, the collapse in complexity can be promoted by a low density of delays and a large number of delays.*

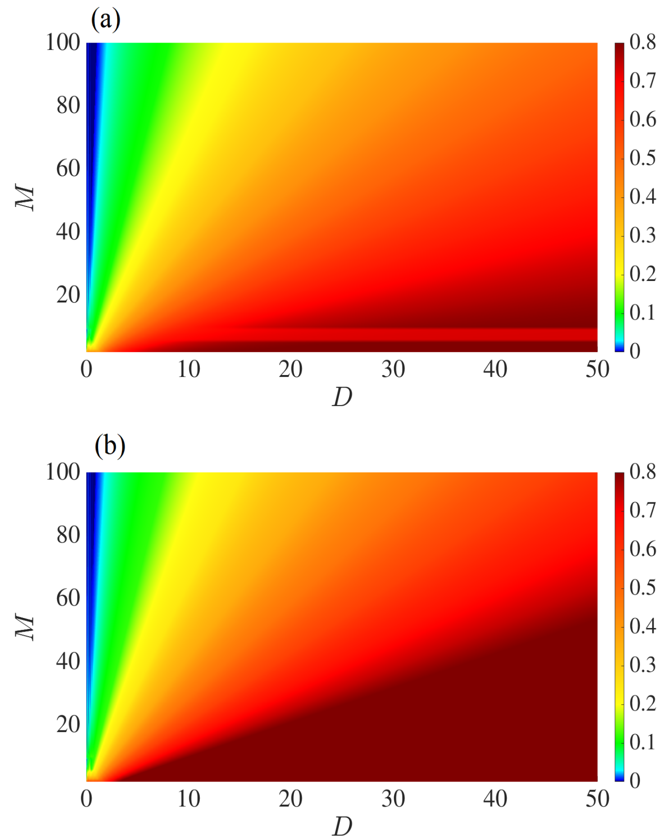

Figure 4.17: $M - D$ Phase diagram obtained by computing the sum of the positive real parts of eigenvalues for the (a) generalized MG and (b) EOO models in the subspace spanned by the delay density D (Eq. 4.21) and the number of delays M. Alternative scheme 2 is used with $\tau_{min} = 17$. The darkest blue color corresponds to stable fixed point behavior.

4.7 Discussion

We have investigated the role of the distribution of the discrete delays on the dynamical behavior of nonlinear first-order delay-differential equations. Stability analysis and numerically computed dynamical invariants reveal that the behavior of these models is highly dependent on the delay distribution. For very high densities of delays, which occur when many discrete delays are packed into a relatively small time range, chaos always exists, no matter how many delays are present. This requires that the minimum delay be sufficiently large; otherwise, chaos can not occur, as expected from single-delay DDEs. Thus, if the feedback involves values around a sufficiently distant and temporally narrow part of the past, complex behavior can ensue.

Intuitively, the map-like aspect of DDEs [132] caused by perturbations of the present state by past states at discrete times is thus retained in this picture; thus, chaos is possible even though there is only one variable (although in reality, the system is infinite dimensional as soon as there is a non-zero delay).

For lower delay densities, which occur when there is a small number of delays or large spacing between the delays, the complexity of the chaos decreases. The temporal spread of the perturbations from the past is then larger, and as a consequence, their joint impact is smeared out; the discrete-time map behavior is less pronounced, and the complexity is diminished. Essentially, since throughout all our study, the delayed feedback at any given time is an average over M past states, then this average will be more smoothed out when the delays cover a wide range in the low D case.

For a fixed spacing, this is even more so when there are more delays. Figure 4.6 shows that while M increases, the mean of the feedback is relatively constant for the generalized MG model, but its standard deviation decreases, especially in scheme 1, supporting the notion of more restrained fluctuations at larger M. Similarly, for the EOO model, the mean is also relatively constant (but decreases slightly in scheme 1), and the SD also decreases, especially in scheme 1. Intuitively, there are even more states to average over, causing more smoothing of the feedback in a moving-average manner and thus lower complexity [27]. In this limit, the DDE behaves increasingly as a distributed delay system, i.e., as an integro-differential system. Such systems are known to require more nonlinearity to exhibit limit cycles and chaos (see, e.g., Ref [118]). In a similar sense, it is as though the extra smoothing were caused by noise, which is always present in practical applications and is known to reduce the effective dimension of discrete and distributed delay systems [129].

For a moderate or large number of delays, almost all of the chaotic windows are replaced by periodic attractors. In those cases, the dynamics is governed by oscillatory feedback, and the density of this feedback variable is multimodal - including bimodal in the case of the simplest oscillation with no other extrema than the single maximum and minimum per period. We have shown that simplified dynamics is closely linked to the roots of the characteristic equation. Specifically, going from a high density to a lower density of delays corresponds to an increase in the number of roots with a negative real part as well as a decrease in the number of roots with a positive real part. For the oscillatory and weakly chaotic regimes, the positive real parts of the roots take on minimal values. This was shown to be parallel to behavior of the LEs, which were calculated here using an extension of the pseudo-spectral method based on Chebyshev nodes.

For a single large delay compared to the system's intrinsic response time, the real part of the eigenvalues scales with the time delay, and the eigenvalues can be expressed using a pseudo-continuous spectrum [143]. Future work should thus consider what happens to this scaling when multiple delays are considered in the nonlinear DDEs. It is also clear that the multi-delay feedback controls considered here provide a novel way to guide the complexity of the system, without explicitly controlling specific unstable periodic orbits with single or multiple delays [117]. In our opinion, this is a direction worth exploring, as is the impact of additive or multiplicative noise on the results presented here, which are likely to shift the bifurcations [144] and thus likely the complexity characteristics - including the collapse to simple dynamics. It would also be interesting to see whether multiple delays could expand the reservoir computing capabilities of single [26] or coupled delay systems [133]. Finally, there is the obvious task of exposing the precise mechanism by which period-doubling bifurcations and cascades can arise by reducing the number of discrete delays.

Chapter 5

Complexity Collapse, Fluctuating Synchrony, and Transient Chaos in Neural Networks with Delay Clusters

Abstract

Neural circuits operate with delays over a range of time scales, from a few milliseconds in recurrent local circuitry to tens of milliseconds or more for communication between populations. Modeling usually incorporates single fixed delays, meant to represent the mean conduction delay between neurons making up the circuit. We explore conditions under which the inclusion of more delays in a high-dimensional chaotic neural network leads to a reduction in dynamical complexity, a phenomenon recently described as multidelay complexity collapse (CC) in delay-differential equations with one to three variables. We consider a recurrent local network of 80% excitatory and 20% inhibitory rate model neurons with 10% connection probability. An increase in the width of the distribution of local delays, even to unrealistically large values, does not cause CC, nor does adding more local delays. Interestingly, multiple small local delays can cause CC provided there is a moderate global delayed inhibitory feedback and random initial conditions. CC then occurs through the settling of transient chaos onto a limit cycle. In this regime, there is a form of noise-

induced order in which the mean activity variance decreases as the noise increases and disrupts the synchrony. Another novel form of CC is seen where global delayed feedback causes "dropouts," i.e., epochs of low firing rate network synchrony. Their alternation with epochs of higher firing rate asynchrony closely follows Poisson statistics. Such dropouts are promoted by larger global feedback strength and delay. Finally, periodic driving of the chaotic regime with global feedback can cause CC; the extinction of chaos can outlast the forcing, sometimes permanently. Our results suggest a wealth of phenomena that remain to be discovered in networks with clusters of delays.

5.1 Introduction

Biological neural networks can involve delays below the millisecond time scale up to several tens of milliseconds [145]. A wide array of delays are involved in inter-areal communication [106]. A redundancy cancellation circuit in the cerebellum of the weakly fish involves delay distributions between 10 and 70 ms [146]. Local circuitry also involves delays, which are often neglected in modeling studies due to the added dynamical complexity they bring to the problem. But they have been shown to promote oscillations [104, 105, 147], and play important roles in synchronization phenomenon [137] and learning phenomenon [148]. They are of course omnipresent in large scale neural control systems where they can reach many hundreds of milliseconds, e.g., in reflex arcs [36].

What are the dynamical consequences of the existence of multiple delays, either centered around a single mean delay, or clustered into different groups? There is widespread belief that systems with many delays can be treated as ones with a single distribution of delays, i.e., a delay-differential equation with discrete delays can be replaced by an integro-differential equation with a suitably chosen delay or memory kernel. Accordingly, the presence of many delays with a sufficiently broad distribution should decrease the dynamical complexity [27, 118, 125, 149].

Recently it has been shown, using numerical experiments of simple model physical systems along with a novel Lyapunov spectrum estimation method for multi-delay nonlinear systems, that this complexity reduction can happen quite abruptly, and therefore be more aptly named complexity collapse [27]. The effect has been investigated by adding delays to standard one-delay systems in one variable, such as the Mackey-Glass equation and the electro-optic model, or the three-variable Lang-Kobayashi laser model. Our work here raises and provides first answers to the question of whether this multidelay complexity collapse (MDCC) can occur in chaotic neural networks with multiple neurons, i.e., with many state variables.

Note that we are distinguishing here between the number of state variables that describe the time-varying quantities in these models, and the infinite number of variables that relate to the delay per se; all differential-delay systems are infinite-dimensional by definition, regardless of the number of delays. Beyond this distinction, it therefore remains to be seen how a cluster of delays around some mean delay affects the chaotic properties of a neural network, and whether additional clusters further cause increases or decreases in dynamical complexity. While our previous study allowed for a more precise diagnostic of attractor properties, using permutation entropy and Lyapunov spectrum estimation, here the large number of state variables (around 1,000) make such computations prohibitively expensive. We thus resort to other simpler metrics that focus on the time-dependent mean and standard deviation of the activity variable averaged across the network.

Of particular interest to us is the question of under which conditions and with respect to which phenomena do delays matter in realistic neural systems. The particular aspect of this question that we focus on is the distribution of discrete delays. Such delays, even acting alone, are notorious for causing simple oscillations and, with the right shape and strength of nonlinearities, chaotic fluctuations; yet distributed delays are known to counteract some effects of nonlinearity [22, 118]. At which point should one think in terms of continuous delay distributions, and what is expected in the remaining vast domain between single and distributed delays? And how are these issues at play in chaotic neural nets? One expects that bifurcations can occur, but also novel forms of multistability and susceptibility to rhythms impinging from other brain areas. Such effects are indeed highlighted in the results presented below, along with their robustness to noise.

In Section 5.2, we introduce the model of interest, namely, a standard 80/20 excitatory-inhibitory (EI) model that has often been used to mimic the cortex. It has local delays between the E and I cells, but can also account for a global delayed inhibitory feedback to both populations with a larger delay (see Fig. 5.1, dashed lines). This global feedback mimics a longer route for inhibition that possibly involves other populations that are not explicitly modeled. It is considered here because the complexity collapse phenomenon (CC) does not occur in the EI network on its own, but does in this slightly more complex dynamical system with two delay clusters. In the section 5.3, we thus first probe how a single delay within and between these sub-populations affect the dynamics. In this network, neurons behave in a much more complex manner as the time delay becomes smaller. Next, we examine the activity and complexity of dynamics generated by neurons under the influence of the global inhibitory feedback term. We will present a novel form of behavior that is reminiscent of a chimera [57, 150, 151], but with space replaced by time. In other words, we report an alternation of asynchronous and synchronous epochs which seem to follow Poisson statistics. We further show a paradoxical effect in which the activity fluctuations are more constrained the higher the noise is, which is a form of noise-induced order [152]. As a consequence of the inclusion of the additive noise with sufficiently large intensity, synchronous activity can be suppressed. We further provide

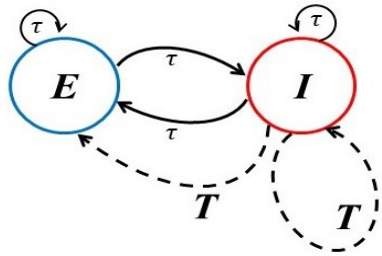

Figure 5.1: Network architectures. The solid lines provide the schematic of the basic excitatory-inhibitory (EI) network in which the connections can have multiple smaller delays (denoted here by τ) characteristic of local circuitry. The dashed lines account for an extra global inhibitory feedback with longer delay T from population I to itself and to the E population.

preliminary observations of the effect of periodic driving of the excitatory sub-population during synchronous epochs, finding that it can alter the dynamics of the whole network. Post-stimulation dynamics can be unpredictable, leading either to transient high-frequency oscillations followed by a return to chaotic dynamics with synchronous epochs, or to CC with periodic behavior. The possibility of observing CC in the presence of the global inhibitory feedback and external stimuli led us to finally study the dynamics of these sub-networks in the presence of multiple local time delays. The non-linear characteristic of this network prevents CC in the absence of the global inhibitory delayed feedback. However, this non-linearity is seemingly weaker when distributed delays in the local recurrent EI circuitry co-occur with a global delay. For a larger width of the distribution of delays, the transient chaos is replaced by a simple oscillation.

Note that, for the sake of brevity, none of the phenomena reported here are analyzed individually in great detail. We have rather opted for a presentation of a few novel effects related to CC that will hopefully guide future studies; all our results are linked by the existence of multiple delays in various clustered configurations.

5.2 Model and Methods

We consider an excitatory and an inhibitory sub-network of rate model neurons, each coupled within itself and to the other sub-network. The architecture corresponding to this network is shown in Fig. 5.1. The potential of an excitatory neuron is designated as u, and an inhibitory neuron as v. A similar model without local delay and global inhibitory feedback delay has been studied in [23]. In parts of our work, we go beyond this model by assuming that each of these sub-networks is also affected by global delayed inhibitory feedback from the inhibitory cells, with a global feedback strength κ; this global feedback delay is made longer than the local recurrent feedback delay. The delayed feedback aspects of our model are similar to those in [20, 22]. The dynamical equations for the potential of each unit in the network are:

$$\begin{aligned}\alpha_e^{-1}\frac{du_j}{dt} &= -u_j + \frac{1}{n_e}\frac{1}{M}\sum_{l=1}^{M}\sum_{k=1}^{N_e} w_{jk}^{ee}\phi(u_k(t-\tau_l)) + \frac{1}{n_i}\frac{1}{M}\sum_{l=1}^{M}\sum_{k=1}^{N_i} w_{jk}^{ie}\phi(v_k(t-\tau_l)) \\ &\quad + \frac{\kappa}{N_i}\sum_{k=1}^{N_i}\phi(v_k(t-T)) + \sigma\xi_E + S(t)\end{aligned} \tag{5.1a}$$

$$\begin{aligned}\alpha_i^{-1}\frac{dv_j}{dt} &= -v_j + \frac{1}{n_e}\frac{1}{M}\sum_{l=1}^{M}\sum_{k=1}^{N_e} w_{jk}^{ei}\phi(u_k(t-\tau_l)) + \frac{1}{n_i}\frac{1}{M}\sum_{l=1}^{M}\sum_{k=1}^{N_i} w_{jk}^{ii}\phi(v_k(t-\tau_l)) \\ &\quad + \frac{\kappa}{N_i}\sum_{k=1}^{N_i}\phi(v_k(t-T)) + \sigma\xi_I\end{aligned} \tag{5.1b}$$

where the τ_l's are the local conduction delays which may all be the same, or be taken from a discrete probability density. $\xi_{E,I}(t)$ denote Gaussian white noises, chosen for simplicity here as having the same strength $\sigma = \sqrt{2D}$ with $< \xi_{E,I}(t) > = 0$ and $< \xi_i(t)\xi_j(t') >= \delta_{ij}\delta(t-t')$. The firing rate function ϕ follows a sigmoidal function defined as:

$$\phi(u) = \frac{1}{1+e^{-\beta u}}\,. \tag{5.2}$$

All parameters are described in Table 5.1. Some of our last results consider the effect of a periodic input $S(t)$ of different frequencies to the excitatory population. In some of our simulations below, we will consider multiple delays chosen from a discrete density. This means that each unit is connected to all other units with these multiple delays.

Symbol	Definition A	Value
N_e	Number of excitatory units	800
N_i	Number of inhibitory units	200
α_i	Dendritic rate constant – inhibitory	$200Hz$
α_e	Dendritic rate constant – excitatory	$100Hz$
β	Response function gain	100
n_e	Number of excitatory connections for each neuron	80
n_i	Number of inhibitory connections for each neuron	20
w^{ee}	$e \rightarrow e$ Synaptic connection strength	15
w^{ei}	$e \rightarrow i$ Synaptic connection strength	15
w^{ie}	$i \rightarrow e$ Synaptic connection strength	-15.375
w^{ii}	$i \rightarrow i$ Synaptic connection strength	-15.375
κ	Global feedback strength	variable
M	Number of delays	variable
D	Intrinsic noise level	variable
dt	Integration timestep	0.1ms

Table 5.1: Parameters of the two-population model.

We assume that there are $N_e = 800$ excitatory units and $N_i = 200$ inhibitory units in the whole network, and that the probability of connection of any two neurons is 10%. Thus each neuron is connected on average to 100 other neurons. The weight matrix can be seen in Fig. 5.2 in which the excitatory connection weights are fixed at 15 and the inhibitory weights at -15.375 (the mean of the network and mean of the non-zero connections in the network are approximately zero). The initial conditions are picked randomly from a Gaussian distribution with zero mean and unit variance. This choice of values gives a slightly unbalanced network: there are 4 times more excitatory neurons than inhibitory neurons, but the inhibitory weight divided by the number of inhibitory connections ($\frac{w^{ii}}{n_i} = \frac{w^{ie}}{n_i}$) is 4.1 times the excitatory weight divided by the number of excitatory connections ($\frac{w^{ei}}{n_e} = \frac{w^{ee}}{n_e}$). We have checked that the phenomena reported here are robust in the sense that they are qualitatively the same when the network is set up with similar weight ratios, and in particular for the balanced case where the ratio is equal to 4, i.e., with $w^{ii} = w^{ie} = -15$. The results below are also qualitatively similar for the case where elements of the weight matrices are picked randomly from Gaussian distributions such that the mean of the excitatory neurons is 15 and the mean of the inhibitory neurons is -15.375. Also, in the absence of any delays, our network is in a chaotic state, as it is with small local delays in the absence of global feedback and noise. In the thermodynamic limit, the complexity of the dynamics decreases; however, complex dynamics can still be observed provided that smaller delay values are used (at least for the parameters $N = 10000$, $n_e = 800$, and $n_i = 200$ that we tested).

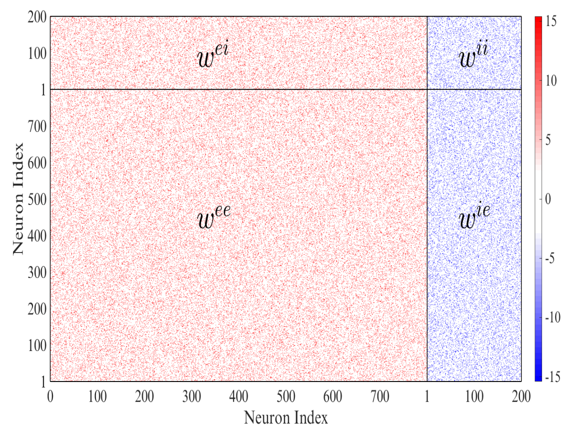

Figure 5.2: Network connectivity. Only 10 percent of the weights are non-zero.

5.3 Results

The mean of the activity of the excitatory sub-network for different time delays between interacting neurons can be seen in Fig. 5.3. For $\tau = 2$ ms, chaotic behavior can be observed, with no clear peak in the power spectrum, which in fact has power-law characteristics. As the time delay increases to 5 ms, a peak arises in the power spectrum at 70 Hz. This peak further shifts toward the lower frequency of 55 Hz as the delay increases. When the time delay between neurons in the local recurrent circuitry is increased to 10 ms, chaotic dynamics can no longer be seen, and harmonics appear in the power spectrum at integer multiples of 25.6 Hz. For this latter case, when the dynamic is affected by noise, one can use the mean-field method introduced in [20] to study the dynamical property of the network. It can be concluded that in this system, a larger delay leads to more coherence between the neurons' activities. We should mention that when we increase connection numbers n_e to 800 and n_i to 200, and the total number of units to 10000 for this set of parameters, the dynamical behavior becomes simpler; but chaotic behavior can still be achieved for smaller time delays.

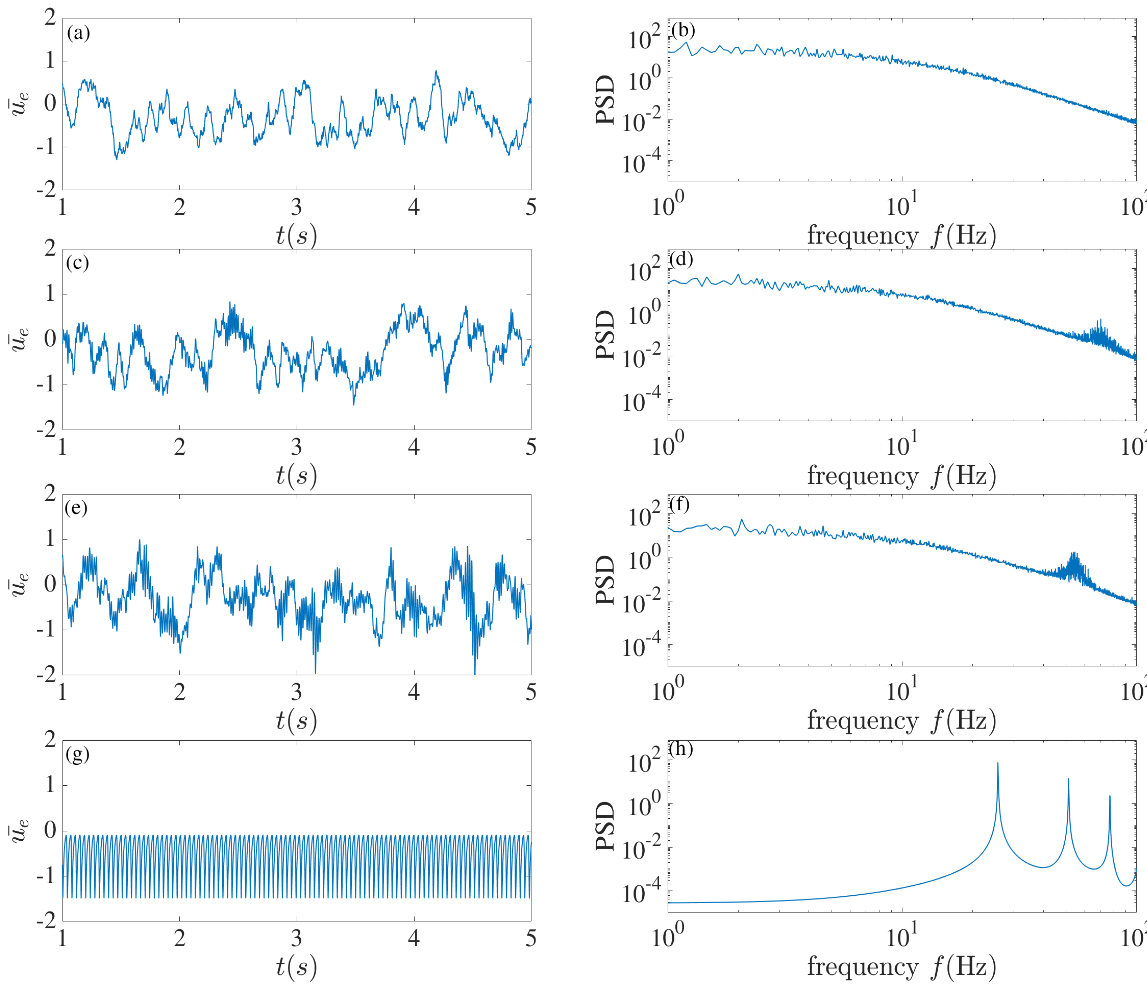

Figure 5.3: Local dynamics alone. The left column shows the mean activity of the excitatory sub-network, and the right column plots the corresponding power spectrum averaged over the activities in this sub-network. From top to bottom, the local time delay corresponds to (a,b) 2 ms, (c,d) 5 ms, (e,f) 7 ms, and (g,h) 10 ms.

In the next step, we examined how delayed global inhibitory feedback from inhibitory units influences network dynamics. In Fig. 5.4, the dynamical behavior of the excitatory network for different global feedback time delays and the smaller fixed local time delay is shown. Without local delayed interactions, the activity is a regular oscillation as is expected from purely inhibitory networks with delay. Here we took the local time delay $\tau = 2$ ms and did the simulation for the fixed value of the global feedback coefficient $\kappa = -5$ and variable global feedback time delay T. The global feedback tends to align the dynamical behavior of all units together, while the influence of the local time delays leads to chaotic fluctuations.

The existence of the global feedback, along with the small local delay, causes the appearance of a pattern of very low activity punctuated by random, sudden and brief jumps to larger values. We call these behaviors "dropout activities". They can be characterized by the time-dependent standard deviation (SD) of the activity across the units in the excitatory sub-network (Fig. 5.4, middle panels). A stronger global feedback tends to weaken the chaotic nature of the units. Each time that the dynamics enter the state of deficient firing rate activity, the standard deviation becomes very close to zero, meaning that the whole network is highly synchronized in this low activity state. Below we will see the paradoxical implications of this behavior for spiking activity using a spiking rule on top of the activities; spikes will be associated with the state of lower mean activity because they are caused by strong fluctuations, i.e., it is a fluctuation-driven spiking regime.

We can gain more insight by looking at the mean of the power spectrum of the excitatory sub-network's activity. As a result of increasing the global feedback time delay, we can observe that the peak around the $3-8$ Hz low-frequency component becomes sharper, and thus that there is enhanced more regular low-frequency activity, a feature that stands out from the time series. Furthermore, it can be seen in the insets that these dropout activities are associated with high-frequency oscillations with very low amplitude, which are also evident in the power spectrum. As the global feedback time delay increases, the higher frequency components become more prominent, such that for $T = 30$ ms there are more high-frequency peaks that are positioned approximately $30 - 40$ Hz from each other.

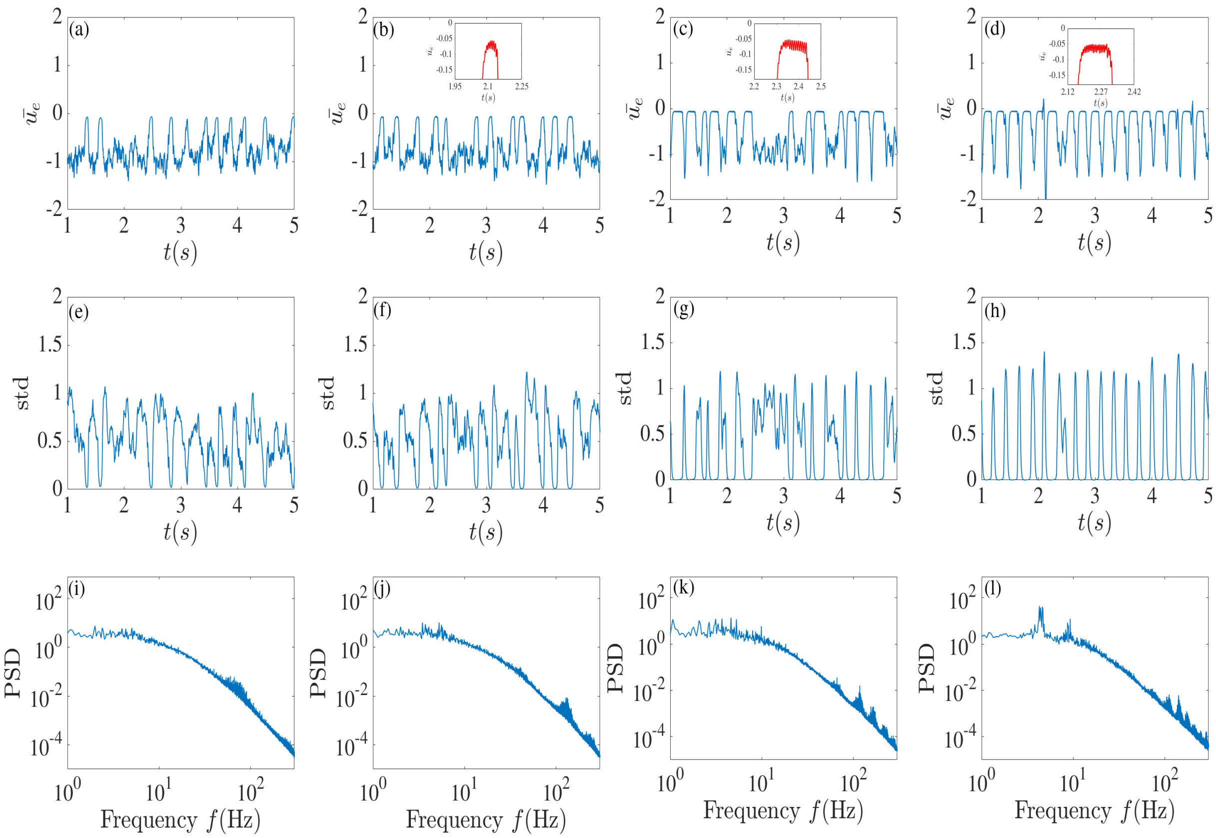

Figure 5.4: Higher global feedback delay causes activity dropouts. Mean of the excitatory sub-network activity (a-d), the standard deviation of the activities of its units (e-h), and the power spectrum averaged over the units in the excitatory sub-network (i-l) in the presence of global inhibitory feedback with fixed strength $\kappa = -5$ without noise. From left to right, the global feedback time delay T equals 5, 10, 20, and 30 ms. The pulse-like epochs in the solution correspond to "activity dropouts" where the sub-network is synchronized with a low firing probability. Paradoxically, between these dropouts, the time-dependent mean activity is lower but its time-dependent fluctuations are stronger. Insets in the figures in the first row show the high-frequency low-amplitude oscillations that occur during the dropouts. The more regular pulsing in (d) is associated with a low frequency peak and its harmonics riding on top of the broadband background.

We illustrate in Fig. 5.5 the influence of the global feedback strength and assume that the local and global feedback time delays are fixed. As for the previous case where the delay was increased, we observe that increasing the strength of the global feedback also promotes synchrony between units. In the power spectra, similar to the case of increasing delay, the high-frequency components become more evident as the units are more synchronized. The enhanced standard deviation outside dropouts raises the possibility for spiking, a fact that will be confirmed below.

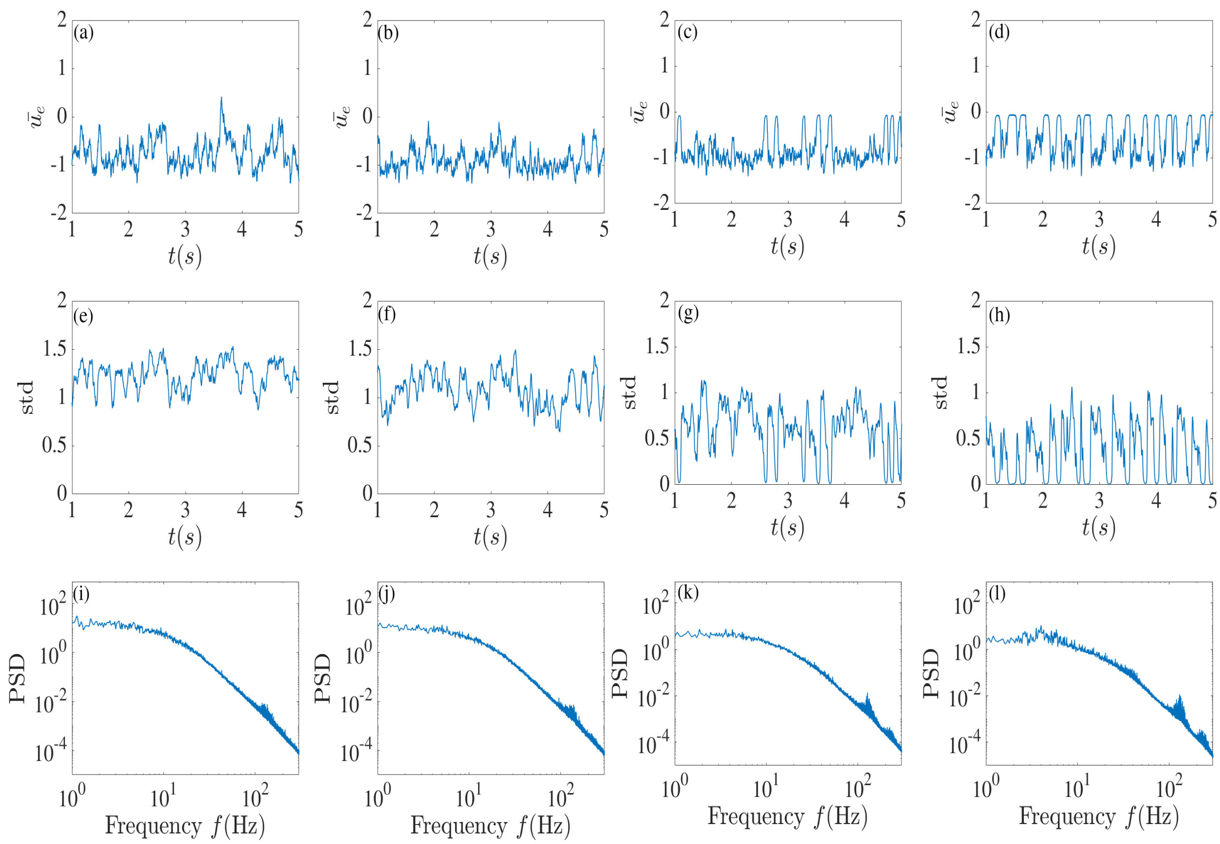

Figure 5.5: Higher global feedback strength causes activity dropouts. Mean (a-d) and standard deviation (e-h) of the excitatory sub-network activities, with the corresponding mean power spectrum (i-l) in the presence of global inhibitory feedback without noise. From left to right the global feedback strength κ equals -1,-2,-4, and -6 and in all cases, the global feedback time delay is $T = 10$ ms. Higher feedback strength causes more dropouts. As for the increased delay case, between dropouts the standard deviation increases.

So far, we have seen that either increasing the delay or the strength of the global feedback, the degree of complexity decreases. One difference between the two cases is that at large global feedback coupling, the dynamic will be stuck in a regime of high-frequency low-amplitude oscillation (not shown), while for large global feedback time delay, oscillation with low frequency is the dominant behavior of the sub-networks. The phase diagram for different κ and different global feedback time delay T is shown in Fig. 5.6. For this computation, we counted the number of activity drop-outs during 35 s following a 2-s transient, repeating the simulation for different κ-T pair.

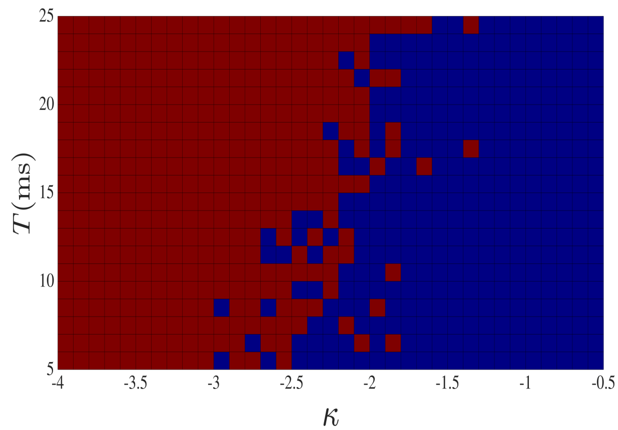

Figure 5.6: Activity drop-out phase diagram in κ-T space. Red squares correspond to the cases where at least one activity drop-out was observed during 35 s, and blue squares for the cases with no activity drop-out. Stronger and/or longer delay global feedback are seen to promote drop-outs.

The pattern of sudden low activities caused by the global feedback appears to be highly vulnerable as it can not be sustained in most cases, and asynchronous fluctuations may be reinstated. In Fig. 5.7, these patterns are still found for small noise intensities, while the standard deviation fluctuations in these cases are more constrained. As the noise intensity increases, these dropouts are less likely to occur. It can be noticed that for significant noise intensity, the variations of the time-dependent standard deviation become more confined around 0.5; thus at higher noise, both the mean and the standard deviation seem to stabilize. This appears to be a form of noise-induced order from a chaotic state [152]. A simple picture here is that the noise in fact breaks up the synchronous periods and makes the dynamics more homogeneously asynchronous. Despite the decreasing occurrence of activity dropouts, the power spectrum still shows peaks around the high-frequency component, although they are reduced in size. The power spectrum at low frequency also becomes flatter as D increases, with a clear transition to a power-law regime at higher frequencies.

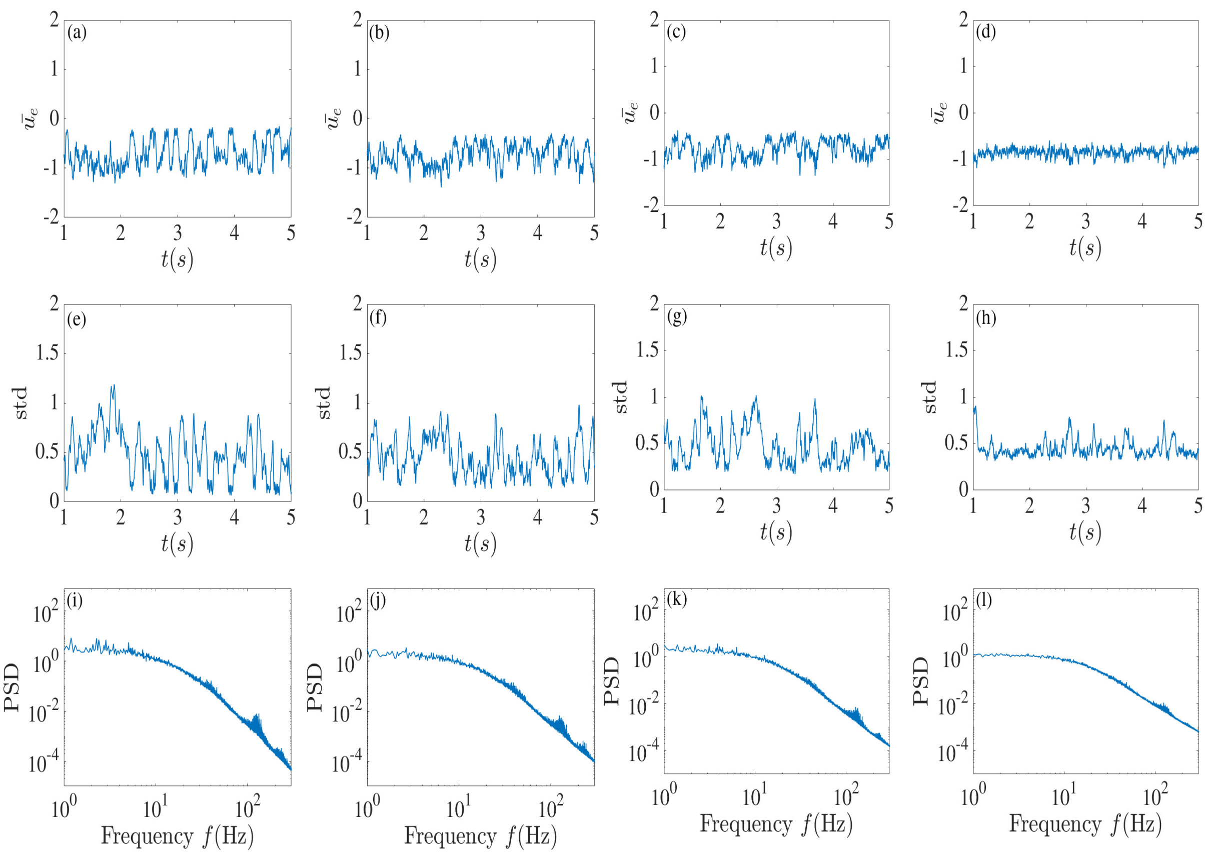

Figure 5.7: Noise suppresses activity dropouts. Mean activity (a-d), standard deviation (e-h) and power spectrum (i-l) averaged over the excitatory sub-network for increasing noise intensity D and fixed global inhibitory feedback with time delay $T = 10$ ms and strength $\kappa = -5$. From left to right, $D = 10^{-5}$, 5×10^{-5}, 10^{-4} and 5×10^{-4}. The dropouts seen in Fig. 5.4(b) are no longer seen, and the fluctuations of the standard deviation decrease at higher noise intensity.

From the raster plots in Fig. 5.8, we can understand better the dynamics of all the neurons in the two different sub-networks for different cases. In the absence of the global feedback (left column), the mean network activity fluctuates more around the zero value, and it occurs with higher amplitude. In this case, high spiking activity can be observed, where this spiking activity of individual neurons is based on the assumption that firing follows an inhomogeneous Poisson process with the rate $\phi(x)$ (x is either u or v) and the probability of firing in an interval $(t, t + dt)$ is given by [23]:

$$p(x) = 1 - e^{-\phi(x(t))dt} \,. \tag{5.3}$$

By taking into account the global delayed feedback (three right columns), activity dropouts can be seen in yellow bars in the activity rasters at the top. With a strong enough global feedback coefficient, and sufficiently long delay, the amplitude of the fluctuations decreases and the mean of network activity shifts down to more negative values. This makes sense given that the global feedback is inhibitory. As a consequence, the network spiking activity decreases. We can see clearly that the dropouts are associated with epochs of high mean activity but low standard deviation of activity - hence the name “dropout”. For stronger noise intensity, the probability of dropouts decreases, resulting in slightly more widespread spiking activity.

In the middle row, it can be seen that for this set of parameters, spiking activity is slightly higher in the inhibitory sub-network compared to the excitatory sub-network, and there would rarely be a spike during an epoch of dropout. With the decreasing of the amplitude of the fluctuations of the standard deviation through increasing noise intensity, we see that somehow the spiking activity spreads out, especially in the inhibitory sub-network.

The histogram of the time difference between the two dropout activities is shown in Fig. 5.9. The statistic is calculated in the following way. We first take the arbitrary threshold value of 0.06 for the standard deviation. We store the data for a duration between the time the standard deviation falls below 0.06 and the time that it rises above 0.1. During this interval, we record the time corresponding to the minimum value of standard deviation. This process is repeated up to $t = 1500$s.

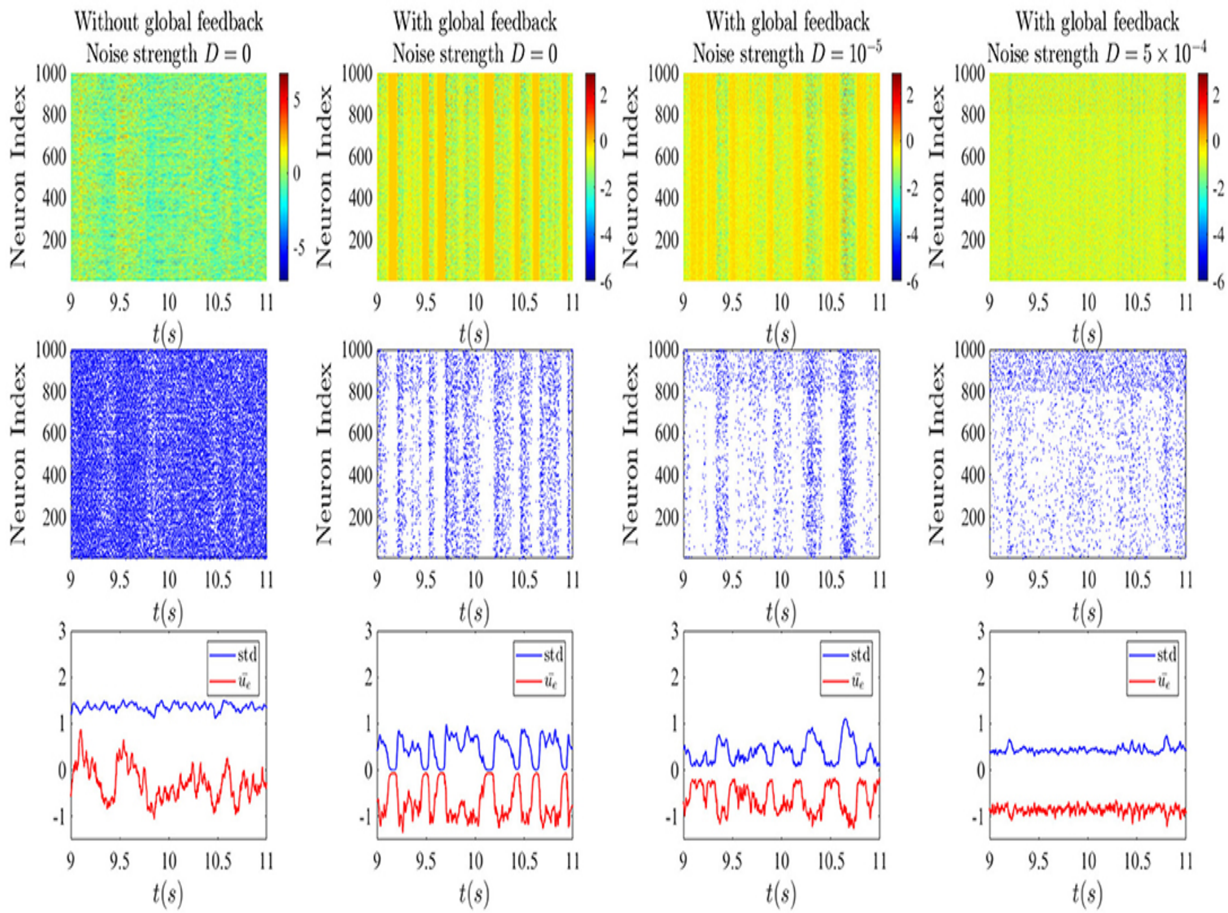

Figure 5.8: Effect of noise on chaotic global activity dropouts. Top: Raster plots of neuron activities from simulations of Equations 5.1a and 5.1b. Middle: Raster plots of neuron spiking obtained by applying the Poisson spiking rule Equation 5.3 to simulations in the top row. Bottom: time-dependent mean and standard deviation of the activities of units in the excitatory sub-network. In the left column, the noise and the global feedback are set to zero. In the second column, the global inhibitory feedback is added, leading to the random occurrence of epochs of strong synchrony due to activity dropouts. The last two columns correspond to the cases with additive weak and strong noise on the dynamics of the units. The global inhibitory feedback delay T is 10 ms and its strength κ is -5. The top rows show that the inhibitory sub-network exhibits qualitatively the same behavior as the excitatory one, but with a slightly higher spiking rate.

First, we only varied the global feedback strength κ from -4 to -6, and the effect of noise was only considered in the last panel of Fig. 5.9. Increasing the impact of global feedback on the dynamics coincides with the increase in the probability of these events in a shorter interval, and the statistic tends to be more Poissonian. Due to the noise, the fluctuation around the arbitrary threshold value increases and consequently, the time difference between these events decreases significantly. In general, however, greater noise levels tend to suppress dropout activity.

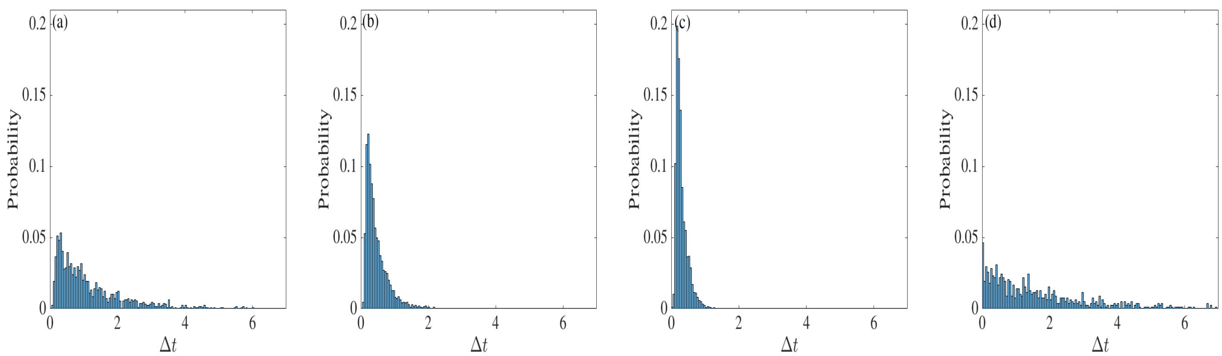

Figure 5.9: Frequency of chaotic activity dropouts increases with stronger feedback. The probability of intervals between successive low firing activity dropout events. In the first three columns (a-c), the noise strength is $D = 0$ and the global feedback strength κ changes from -4 to -5 to -6. In (d), separate noise terms, each with intensity $D = 10^{-5}$, are added to the excitatory and inhibitory dynamics. In all cases the global feedback time delay T is 10ms.

Externally applied stimuli can have a wide range of dynamical effects, including suppression of chaos, entrainment, etc [24, 153]. Of particular interest is the effect of external periodic stimuli (chosen here with an amplitude of 0.2) on the dynamics in the presence of dropout activities. In Fig. 5.10, the noise is turned off, and only the sinusoidal external input with different frequencies is applied for a duration of 1 s. It can be seen that after a low-frequency stimulus such as 5 Hz ceases, the chaotic network activity prior to stimulation is replaced by a high frequency oscillation of 130 Hz. The duration of these simplified dynamics beyond the stimulation is found to vary as a function of stimulation frequency. For example, for a 15 Hz stimulus, the duration elongates a little, but eventually the system recovers its natural dynamical properties. As seen third column in Fig. 5.10, when the stimulation frequency is relatively higher, the chaotic dynamics may not be recovered at all, or at least not for a much longer time. Because timing and duration of stimulation are crucial in applications, how the network responds to stimulation appears highly complex, and a full investigation is beyond the scope of this paper.

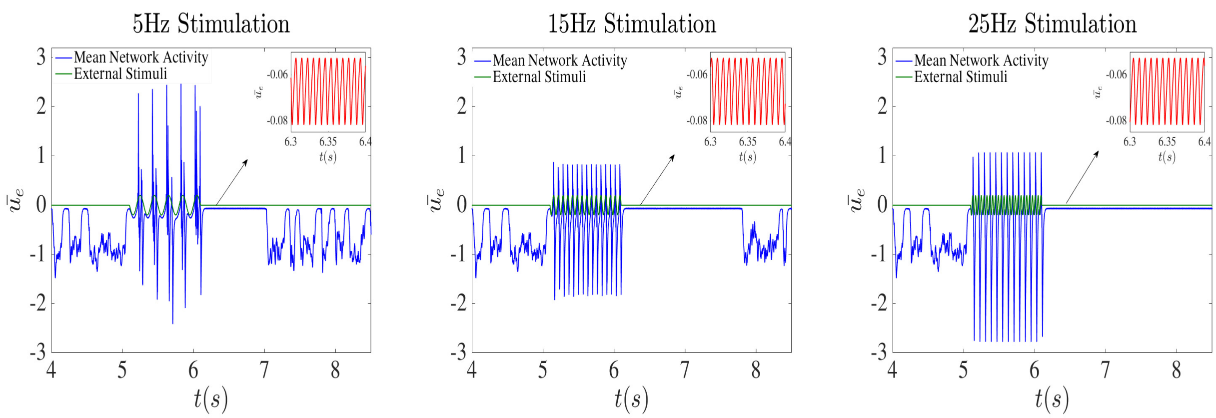

Figure 5.10: Frequency-dependent complexity collapse. Network dynamics when an external sinusoidal stimulation is activated for 1 s from $t = 5.1$ s until $t = 6.1$ s. Here the global feedback strength is $\kappa = -5$ and the corresponding time delay is 10 ms.

It has been shown [27] for many dynamical systems from lasers to biological feedback system that upon adding a sufficient number of delays to the dynamics, a transition from chaos to simpler behavior such as periodic motion, or even fixed-point behavior, can occur, provided that the range of delays is sufficiently broad. In Fig. 5.11, we show the behavior of the network activity when multiple local delays are included. Here we set the noise to zero, as well as the periodic stimulation and the global feedback. We assume that the minimum delay is equal to 2 ms, and more delays added at $\Delta\tau = 0.2$ ms increments up to a maximum delay of $[2 + 0.2(M - 1)]$ ms.

We carried out the simulation for $M = 6$, $M = 11$, $M = 16$ and $M = 21$. Fig. 5.11 shows that, in contrast to the aforementioned delayed dynamical systems, the dynamical properties are not affected so drastically upon adding more delays. This is likely due to the fact that the local EI recurrent dynamics have sufficient intrinsic non-linearity to support chaos without relying on the delay. Our simulations for unrealistically large local delays (with large spacing between delays, and up to a largest delay of 242 ms for 21 delays) revealed no dropout activity or complexity collapse when there was no delayed global feedback (not shown).

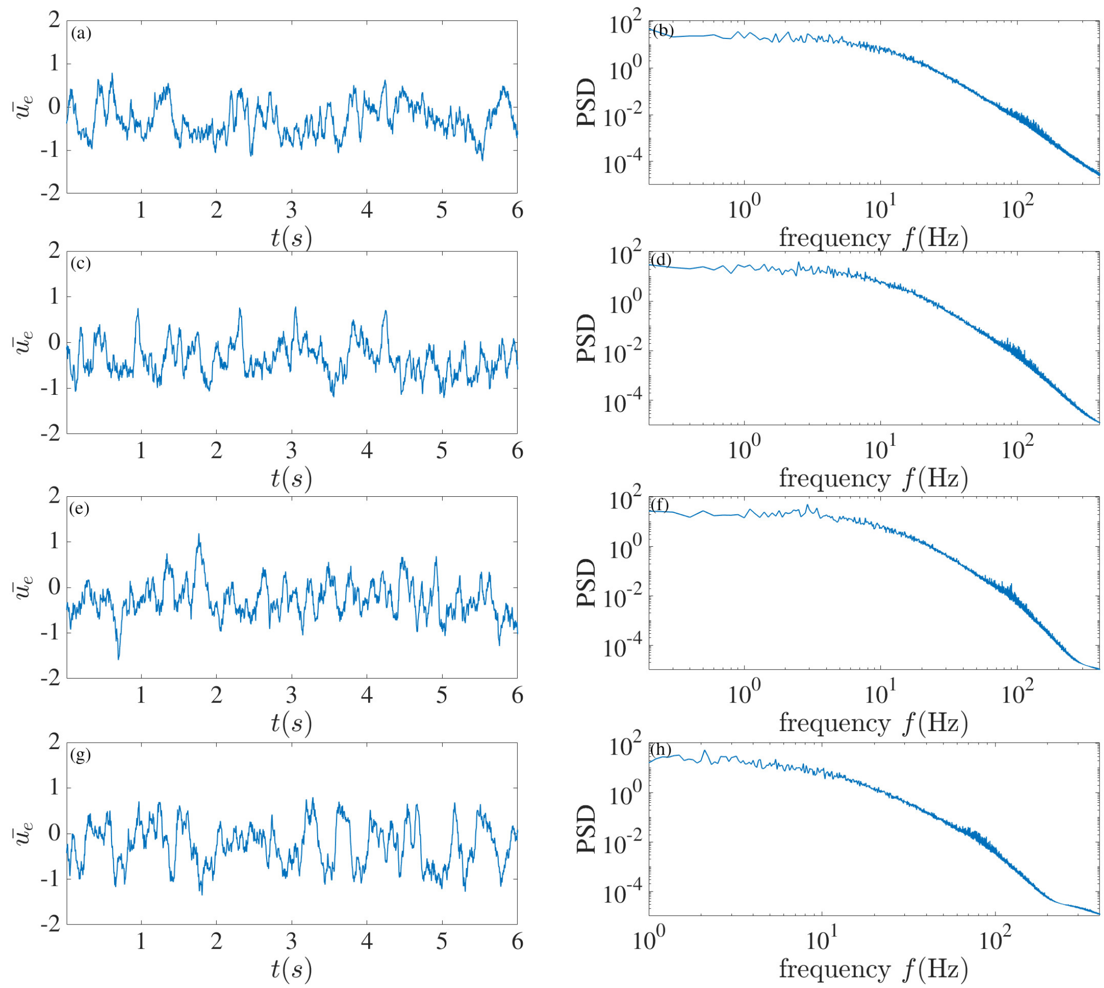

Figure 5.11: Broadening the local recurrent delay distribution has little effect in the absence of global delayed inhibition. Mean excitatory sub-network activity for different number of delays M. From top to bottom, $M = 6$ (a,b), 11 (c,d), 16 (e,f), and 21 (g,h). Here the global feedback and the noise are set to zero. The delays are confined to the interval $[2, 2 + 0.2(M - 1)]$ ms. No complexity collapse is seen, and the spectra are difficult to tell apart.

It is interesting that for a single delay case, as we saw in Fig. 5.3, and for large enough delay, dynamics are simple oscillatory. However, the presence of smaller local delays makes the oscillatory dynamics chaotic. As we saw earlier, global feedback delay can decrease the degree of complexity in the chaotic dynamics. Therefore, we consider the dynamics of the network with multiple local delays in the presence of the global delayed feedback to see whether we can observe the complexity reduction with multiple delays. Parameters used in Fig. 5.12 are the same as those used for Fig. 5.11.

A key finding is that in the presence of both local recurrent delayed feedback and global inhibitory delayed feedback, the dynamics are significantly affected by the multiple local delay times. Indeed, Fig. 5.12 reveals that, as the distribution of the time delays broadens, the system manifests transient chaos, which eventually converges to a periodic limit cycle attractor with the low amplitude oscillations. Hence, in the presence of a global inhibitory delayed feedback, the system exhibits CC; but it requires a longer delay inhibition to occur. The new feature with respect to the previously reported MDCC is that here the transition to simpler dynamical behavior involves transient chaos.

5.4 Discussion

We have focused on the properties of a rate-based neural network with a small number of short delays in the local sparsely connected EI recurrent circuitry, and how this is altered by a longer delay that acts globally through all-to-all feedback inhibition. Our goal was to investigate under which conditions, if any, a broadening of the local delay distribution can lead to a simplification of the chaotic dynamics seen for a single delay. By construction, the setup of this problem also allows a preliminary analysis of the effect of clusters of delays on local recurrent EI dynamics, although we have limited our study to two clusters, one of which contains only a single delay. But the means of these clusters are related by a factor of 2-3. Apart from being relevant to neural circuitry, the inclusion of the global feedback was found to be necessary to see CC in a chaotic EI neural network, if the local delays are not allowed to take on values that are too large.

Specifically, we first showed that an increase in the local time delay could lead to a

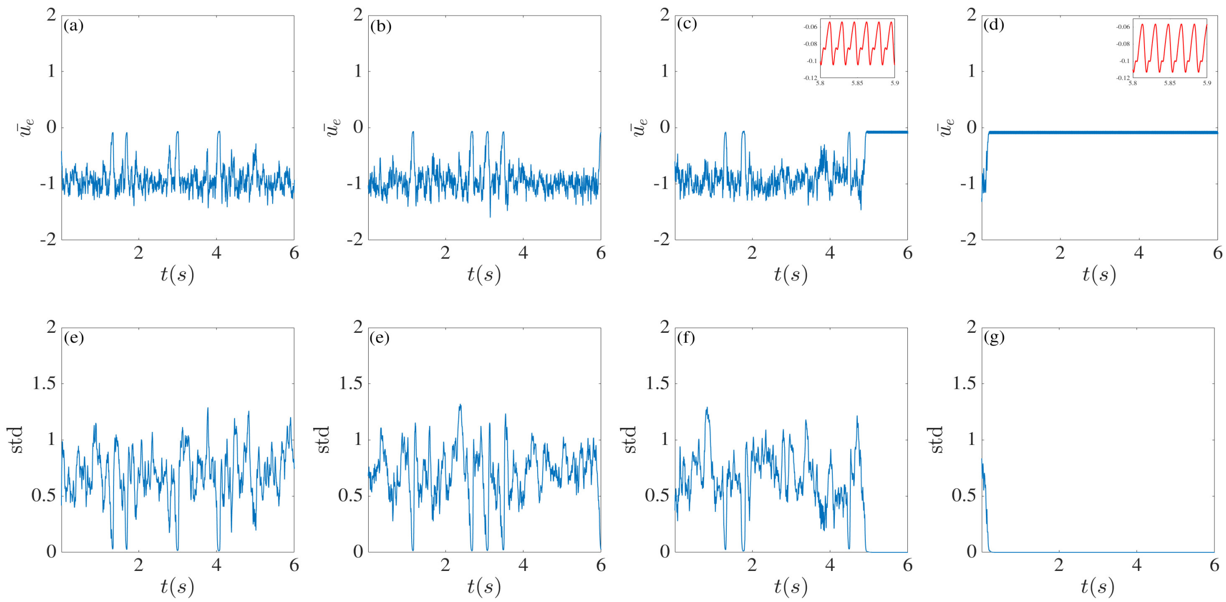

Figure 5.12: Broadening the local delay distribution initiates complexity collapse in the presence of global delayed feedback. Mean excitatory sub-network activity for different numbers M of local delays. From top to bottom, $M = 6$ (a,b), 11 (b,c), 16 (d,e) and 21 (f,g). The global feedback time delay T is 10 ms and the feedback strength κ is -4. The delays are confined to the interval $[2, 2+0.2(M-1)]$ ms. The CC occurs faster the stronger the delay is.

drastic change in the deterministic dynamics. When this delay is unique and is increased from 2 ms to 10 ms, chaotic dynamics are abruptly replaced by regular periodic synchronized network firing (Fig. 5.3). This is a first instance in which the complexity collapses in our network, although in a manner that does not rely on the inclusion of more delays [27]; rather it appears to simply arise from a bifurcation when the single delay parameter is increased.

Adding a delayed global inhibitory feedback can however lead to different interesting phenomena. The main one, show in Figs. 5.4, 5.5, features chaotic dynamics that exhibit sudden pulses which we have termed “activity dropouts.” This effect is more pronounced when the global feedback is strong or its delay is large. Interestingly it is also associated with a power law behavior of the mean activity over three orders of magnitude (only 2.5

orders are shown). These activities contain a high-frequency component that is embedded possibly an unstable orbit in the chaotic attractor due to the local time delay. This property becomes essential when other simplification factors are added to the system, such as increasing the number of local delayed interactions (Fig. 5.12) or correlated input. While adding uncorrelated input, such as white noise, does not destroy this component completely, it helps maintain the activity's chaotic nature due to the recurrent local interaction (Fig. 5.7). But paradoxically, additive noise on the dynamics also leads to a reduction in the size of the fluctuations in the time-varying standard deviation. This is a form of noise-induced order from a chaotic state first reported by Matsumoto and Tsuda (1983).

The activity dropouts are interesting because the global feedback makes the standard deviation (SD) of the solution on the attractor vary randomly (in fact, Poisson-distributed - see Fig. 5.9). The mean of the activity is higher during the periods of low SD, yielding minimal spikes - thus the term "dropout". During the periods of high SD, the mean activity is even lower, but the few cells that fluctuate the most are able to fire during the higher portions of these fluctuations, and their spikes drive the whole network activity. Note that the model does not explicitly run on spiking; the spikes are a derived quantity from Equation 5.3.

The more regularly aspects of the activity that involves dropouts is reminiscent of the stabilization of unstable periodic orbits using delayed feedback (Pyragas control), although the precise form of the global feedback used here differs from the one used in that chaos-control scheme. Nevertheless this global feedback may create or reveal an underlying slower rhythm embedded in the chaos and which becomes manifest as a lower frequency peak and its harmonics in the power spectra (see Fig. 5.4(l)).

Complexity collapse in the sense of that in [27] does appear in our work through the broadening of the local delay distribution as seen in Fig. 5.12; but for the parameter range where we found this effect, the global inhibitory feedback with longer delay must be present. It is possible that other regimes occur in which CC does not rely on the presence of this global feedback.

The novel behavior in Fig. 5.8 is striking in that there is a temporally random appearance of epochs of dropouts. The time between these dropouts are reminiscent of up-states seen experimentally in neuroscience, and the dropouts as down states. This appears to be a novel deterministic behavior that is synchronized across the network, i.e., it is not a chimera. It survives the presence of moderate noise. There is a sense in which the global inhibitory feedback introduces longer time scales in the network dynamics - the stronger it is, the less power there is at low frequencies (Fig. 5.5). This might share features and origins with the long time scales that arise from introducing population clusters - instead of delay clusters as done here - into EI networks in [154].

Delayed inhibitory feedback has also been reported to elicit transitions between quasi-periodic partial synchronization and collective chaos [155]. Our dynamics here appear to differ from that scenario in that the collective behavior here is not periodic (our network also has E and I coupling). Another point of comparison is the work in [156] where inhibition with long delay can bring on collective oscillations as we see here in Figs. 5.4, 5.5; it remains to be seen whether a winner-take-all mechanism is at work in our system as reported there.

The final point of interest is the fact that the broadening of the local delay distribution brings on a collapse from chaos to simple (limit cycle) dynamics in a time inversely proportional to the width of that distribution (Fig. 5.12). This is a form of transient chaos in neural networks [157] that relies here on delay clusters. It warrants a deeper investigation, especially of its dependence on the initial state of the network. It reflects special properties of the underlying attractor that are emphasized also in response to external inputs. Indeed we have uncovered a frequency-dependent silencing of the network activity, or frequency-dependent CC that can be temporary or even likely permanent, depending on the frequency. It is a different form of persistence from stimulation reported in [24]; in particular, the silencing time seems to depend on the timing of when the stimulus is applied (not shown). This will be investigated elsewhere. This may bear on the reaction of the activity of a neural network with delay clusters to extraneous rhythms or artificial stimulation.

Chapter 6

Boosting Reservoir Computer Performance with Multiple Delays

Abstract

Time delays play a significant role in dynamical systems, as they affect their transient behaviour and the dimensionality of their attractors. The number, values and spacing of these time delays influences the eigenvalues of a nonlinear delay-differential system at its fixed point. Here we explore a multi-delay system as the core computational element of a reservoir computer making predictions on its input in the usual regime close to fixed point instability. Variations in the number and separation of time delays are first examined to determine the effect of such parameters of the delay distribution on the effectiveness of time-delay reservoirs for nonlinear time series prediction. We demonstrate computationally that an optoelectronic device with multiple different delays can improve the mapping of scalar input into higher-dimensional dynamics, and thus its memory and prediction capabilities for input time series generated by low and high-dimensional dynamical systems. In particular, this enhances the suitability of such reservoir computers for predicting input data with temporal correlations. Additionally, we highlight the pronounced harmful resonance condition for reservoir computing when using an electro-optic oscillator model with multiple delays. We illustrate that the resonance point may shift depending on the task

at hand, such as cross prediction or multi-steps ahead prediction, in both single delay and multiple delays case.

6.1 Introduction

Predicting the time evolution of chaotic systems has been a challenging research topic for many decades due to their complexity and sensitive dependence on initial conditions. Various methods have been developed to learn and predict chaotic time series, including artificial neural networks and phase space reconstruction methods [158–160]. One of the innovative models for chaotic time series prediction is based on the brain-inspired formalism developed by Jaeger [161]. This "reservoir computing" (RC) model proposes a network with fixed randomly initialized weight connections. In this framework, an input is injected into the neurons, and only the weights of the connections from the reservoir to the output layer ('readout' weights) are trained. This system has demonstrated its effectiveness in classifying chaotic signals, including inputs comprising a combination of two chaotic signals from the Lorenz system with different parameters [162].

Appeltant et al. [26] later introduced an innovative approach for time series prediction and speech recognition that utilizes a single nonlinear node in the form of a nonlinear delay-differential system, which benefits from the high-dimensional properties of delay systems. This delay-based RC method has been extensively studied in various domains, including quantum dot lasers [163], electronic devices [164], photonic and opto-electronic devices [91, 165]. This architecture has been shown to achieve fast voice speech recognition when implemented with an opto-electronic device [166]. Furthermore, this architecture can be used for characterizing chaotic and hyperchaotic time series from data [167].

The rich dynamical properties of delay systems, such as a relatively large Kolmogorov-Sinai entropy in chaotic regimes, have thus opened up many possibilities for practical machine learning applications. Certain architectures clearly demonstrate the importance of high-dimensional, nonlinear dynamics in RC. In the Lang-Kobayashi (LK) system, modulation type significantly influences the reservoir's capability to map inputs to higher dimensions [168]. It has been demonstrated that phase modulation is more effective than intensity modulation in utilizing these high-dimensional properties. This was further analyzed through studying the behaviour of the steady states of the LK system.

Another example is the recently introduced deep time-delay reservoir computing, which enhances the time-series prediction capability [133]. This architecture displays characteristics analogous to those of convolutional neural networks, with each layer featuring a nonlinear delay system. Notably, in such multi-layered RC systems, the conditional Lyapunov exponents are influenced by the bifurcation point, which has implications for memory capacity [169]. In a more recent development, a novel neural network was introduced, utilizing modulated feedback loops [170]. This system incorporates the dynamics of a nonlinear delay differential equation, with multiple delayed feedbacks and modulation of their strength. By utilizing such features, gradient descent can be used to perform more sophisticated tasks.

The choice of time delay is a critical factor that significantly impacts the performance of a time delay RC. Generally, optimal delays cannot be determined a priori and may depend on the particular task; unsuitable delays can in fact degrade memory capacity and make time series predictions difficult [171, 172].

In this study, we investigate the performance of RC with multiple delays for various tasks. We further explore the optimal choice of parameters for this multi-delay system and study resonance phenomena in different scenarios, such as cross-prediction and multi-step ahead prediction. We illustrate that employing multiple delays can have the benefit of increasing linear memory capacity.

6.2 Multi-time Delay Reservoir Computer (MDRC)

We focus on delay reservoir computing built from the Electro-Optic Oscillator (EOO) model. In its simplest form, it is modeled as a first-order nonlinear delay differential equation with one delay. A schematic of the operation of the single delay reservoir with virtual nodes is shown in Fig. 6.1. The output of the nonlinear node (i.e. the laser) is sent through a delay loop (e.g. an optical fiber), and samples of the activity at specific "virtual nodes" along this loop are versions of the output of the nonlinear node delayed by a fraction of the whole loop delay τ. The high dimension of the phase space dynamics is such that the different virtual nodes behave approximately as independent variables. This is certainly the case in the chaotic regime, but also in the fixed point regime during transients caused by driving the system uni-directionally with inputs generated e.g. by external chaotic systems, and more so when such inputs are time-multiplexed with random masks, as we will now describe.

The single delay RC model operates by injecting multiplexed input into a nonlinear node, which then propagates through a series of virtual nodes equally spaced along the delay loop with a clock-cycle of T. The RC receives a time-varying input, such as a chaotic time series, in the form of a sequence of constant samples of the time series (sample-and-hold values). Each sample, lasting one clock-cycle, advances the input-driven dynamics through the delay loop. This sampling interval can be different from the time delay that couples the virtual nodes together. Figure 6.3 shows via the time arguments the states of the virtual nodes along the K-th cycle.

The constant value of the input during a sample is further modulated by a piecewise-constant random binary signal known as the mask; the same mask is used for each cycle. There are N piecewise-constant sections within each clock cycle T, corresponding to the N virtual nodes. The jumps between the mask values serve to excite complex transients in the nonlinear node, whose state would otherwise converge to a fixed point determined by the current value of the input sample. The product of the sampled input time series (e.g. from a chaotic system), $u(t)$, with this random binary mask constitutes the input forcing signal $J(t)$ to the reservoir computer. The amplitude of $J(t)$ is controlled by the scaling factor γ, which needs to be big enough to perturb the RC, but not too large to overwhelm it.

6.2.1 Stability Analysis of Multi-Delay EOO Model with Filter

In this paper, the single delayed feedback is replaced by multiple feedback paths, each with its own delay. For simplicity we consider the case of equally spaced delays, but we also briefly report on the consequence of deviating from this scheme. As we will see, the spacing between these delays is an important parameter. Recent work has shown that increasing the spacing between delays can effectively suppress chaotic dynamics, resulting in the emergence of periodic or even fixed point behavior in first-order and higher-order

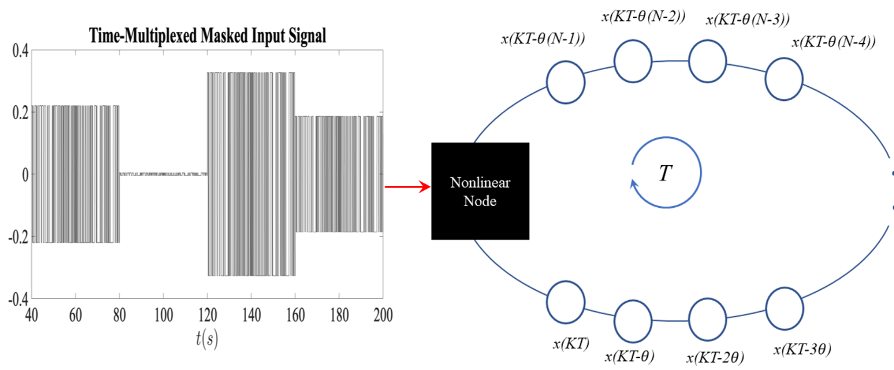

Figure 6.1: Schematic of the single delay RC. The time-multiplexed masked input is injected into the nonlinear node, and travels along the loop with a clock cycle of T, here made equal to the delay τ. The virtual nodes provide time series that are combined in the output layer of the reservoir computer. These nodes are separated by a time interval of $\theta = \frac{T}{N}$. The time arguments for the virtual nodes illustrate how they span the state of the nonlinear delay system across the time interval $(K-1)T$ to KT, where K is a positive integer. Only the first and last virtual nodes are shown.

nonlinear delay differential equations [27, 28]. In addition to the modified version of the model that incorporates multiple delayed feedback pathways, we consider a filter term. The system's dynamics is governed by the following equations:

$$\begin{aligned} \dot{x} &= -x(t) - \delta y(t) + \frac{\beta}{M}\sum_{i=1}^{M} \sin^2(x(t-\tau_i)+\phi) \\ \frac{dy}{dt} &= x(t) \end{aligned} \tag{6.1}$$

where β is the gain coefficient, ϕ is the phase offset and M represents the number of delays. Due to the presence of multiple time scales, this system can exhibit slow-fast dynamics. The filter term acts to eliminate any non-zero steady state solution for the variable x. Throughout this study, we considered $\delta = 1$ and $\phi = \frac{2\pi}{5}$. For the MDRC case, we picked delays as:

$$\tau_i = \tau_{min} + i\Delta\tau\,, \tag{6.2}$$

where $\Delta\tau$ is the spacing between the periodically arranged delays and $i = 1 \dots M$. We note here that this spacing is part of the dynamics of the core of the RC, and determines it eigenvalues and transients at the edge of chaos. It should not be confused with the other use of $\Delta\tau$ in the context of nonlinear time series analysis, namely, the embedding delay applied to a low-dimensional time series to embed it into a higher dimension and analyze its dynamical invariants such as correlation dimension and predictability.

We first consider the intrinsic dynamics of the nonlinear node, independently of the time-multiplexed input and of the output weight matrix applied to its virtual nodes. The nonlinear core of a reservoir computer typically operates in a stable fixed point regime, but close to the destabilization point where a bifurcation to a limit cycle occurs, and this is no different for time delay RCs. This avoids the divergence of the information about the input that would be caused by the sensitivity to initial conditions in a chaotic regime, or the imposition of regularity in a limit cycle regime.

The stability diagram of Eq. 6.1 around its unique fixed point is plotted in Fig. 6.2 for different β and $\Delta\tau$, for two as well as five delays. Increasing the number of delays, the peak of the stability region moves towards the lower spacing between delays and higher feedback coefficient β. For example, for $M = 2$, the peak is located at $\Delta\tau = 2.66$ and $\beta = 3.6$, while for $M = 5$ the peak located at $\Delta\tau = 1.6$ and $\beta = 6.1$. Note however that for both numbers of delays, the smallest spacings lead to loss of stability at smaller rather than larger β. For larger $\Delta\tau$, the boundary of the stabilized regime tends towards that for the single delay case. Here we refer to this latter regime as the large spacing regime. The regime where fixed point destabilization requires a stronger gain will be referred to as the "short spacing" regime. The multi-delay configurations that we tested are robust to adding small random values to the delays, as this had little effect on the destabilization boundary. The following sections will show that the regime needed for time series prediction can depend on the specifics of that task, such as the nature of the time series to be predicted.

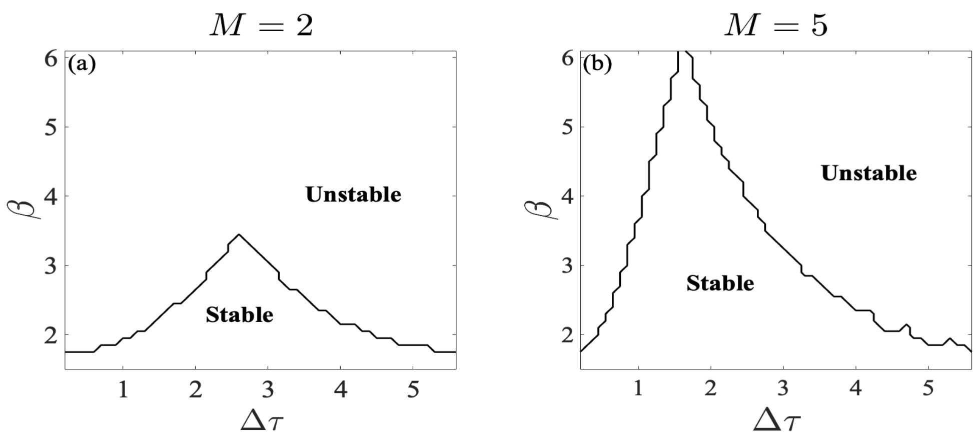

Figure 6.2: Linear stability analysis of equation 6.1 for a multi-delay RC for a system with (a) two delays and (b) five delays. As the number of delays increases, the peak of the stability region shifts towards smaller values of delay spacing $\Delta\tau$ and larger feedback strengths.

6.2.2 Effect of Time Delay and Architecture in Reservoir Computing

The dynamical equations for the EOO with filter can be expressed as follows when masked input is injected into the nonlinear node:

$$\begin{aligned} \dot{x} &= -x(t) - \delta y(t) + \frac{\beta}{M}\sum_{i=1}^{M} \sin^2(x(t-\tau_i) + \phi + \gamma J(t)) \\ \frac{dy}{dt} &= x(t) \end{aligned} \tag{6.3}$$

where γ is the input scaling and $J(t)$ denotes the multiplexed and masked version of the discrete input data $u(k)$. Here we considered a binary mask, consisting of a series of randomly chosen -1 or 1 values. More sophisticated mask functions, such as a chaotic mask or a multi-level mask, could be used to improve the performance of the RC [92]. We considered 200 virtual nodes that are evenly distributed with the temporal distance summing up to $T = 40$ (in other words, $\theta = 0.2$). The states of the nodes are stored in a matrix X. Ideally, we aim to find a weight matrix that linearly combines the node states in a way that minimizes the difference between the predicted output and the target output. In our work, we employ ridge regression to calculate this weight matrix, thereby mitigating the risks of overfitting:

$$\min(||XW - o||_2^2 + \lambda||W||_2^2)\,. \tag{6.4}$$

Here o represents the target output, λ is the Tikhonov regularization parameter, and $||.||_2^2$ is the Euclidean norm. We set the Tikhonov regularization parameter λ to 10^{-8} to mitigate overfitting. The minimization in the preceding equation leads to the desired output weight matrix for the RC:

$$W = (X^T X + \lambda I)^{-1}(X^T o)\,. \tag{6.5}$$

While linear regression is a well-established method for this minimization in RC, it has been shown that using an adaptive training weight matrix can offer significant improvements in reducing prediction errors [173].

Previous works have demonstrated that whenever the time delay τ and the clock cycle T are very close or equal, there is a resonance that is detrimental to the performance of RC as it leads to memory degradation [169, 171, 172]. This resonance effect was investigated analytically using the characteristic equation in [174]. The long delay approximation of the characteristic roots was used, which implies that the real part of the characteristic equation scales with the inverse of the time delay. Solving for the imaginary parts of the characteristic equation then yields:

$$\omega_k \approx \frac{\pi}{\tau}(2k - \nu) \tag{6.6}$$

with k being the index of the eigenvalue and ν taking values of either 0 or 1, the relative angular distance between two successive sample inputs in drive $J(t)$ is determined by ωT. Notably, when T is proportional to τ , this relative angular distance becomes a multiple of π, which diminishes the reservoir's ability to differentiate inputs efficiently [171, 174].

The temporal dependence of virtual nodes on the states of previous nodes, considering different values of time delays and a fixed clock cycle, is visualized in Fig. 6.3. The scheme is more subtle and intricate compared to the single delay RC. The resonance condition is depicted in Fig. 6.3(a) for a single delay case, while Fig. 6.3(b) illustrates the single delay case but in the desynchronized regime where τ and T are mismatched; this could serve as an alternative to avoid resonance. The simplest MDRC is with two delays, and is shown in Figs. 6.3(c) and 6.3(d). In Fig. 6.3(c), the time delays are multiples of the clock cycle, which may result in poor prediction performance, as we will discuss in the next sections. In Fig. 6.3(d), $\Delta\tau = T + \theta$ (specifically, $\tau_1 = T$ and $\tau_2 = 2T + \theta$), which represents an alternative for the multi-delay case. Adjusting the spacing between delays could enhance forecasting accuracy, even when one of the delays is equal to the clock cycle. However, as we will see, these results highly depend on the complexity of the data, the correlation between input data, and the objectives of the reservoir, such as cross-prediction or multi-step ahead prediction.

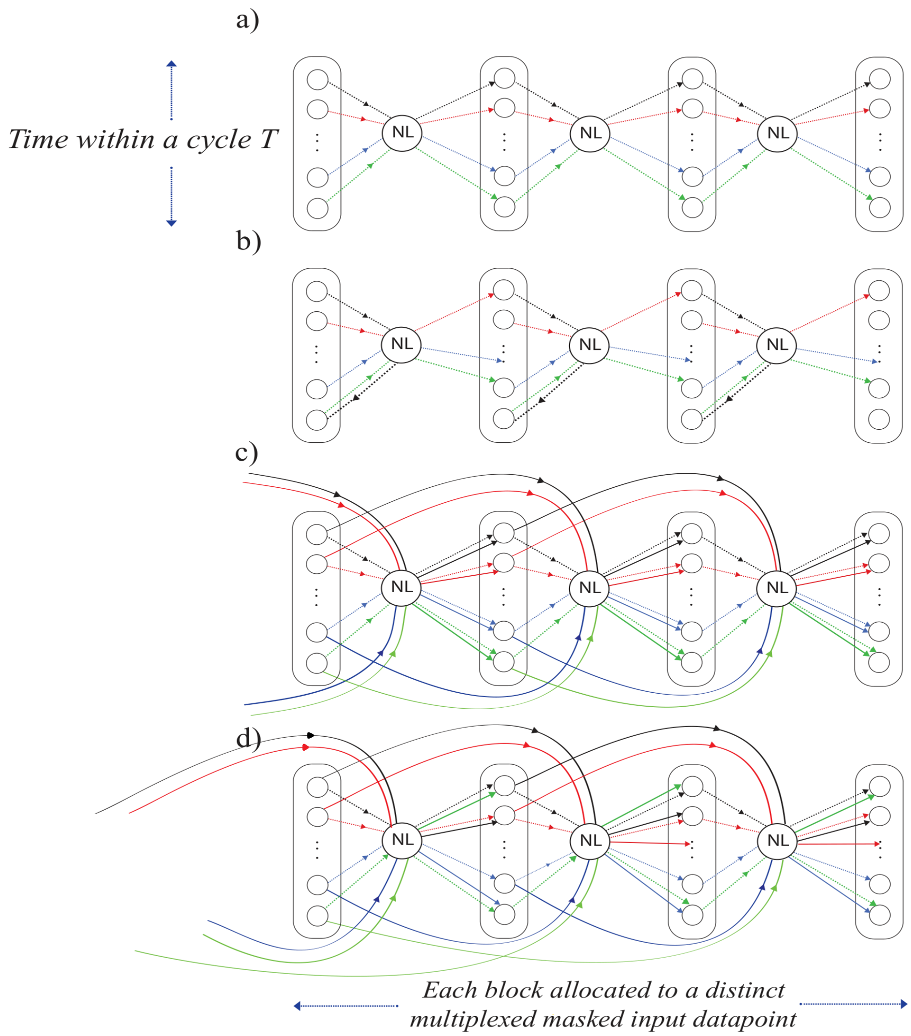

Figure 6.3: Visualizing time-delay couplings between virtual nodes in the loop depicted in Fig. 6.1, showcasing various combinations of single and two delays with different time delay values and spacing between delays. Each vertical block (i.e. cycle of duration T) corresponds to a distinct input data point, which is a sample of the driving time series. Within each block, there are N virtual nodes with a spacing of $\theta = \frac{T}{N}$. A single time delay is assumed in panels (a) and (b). In panel (a), the time delay is set to the clock cycle ($\tau = T$). The dynamics can then be seen as mapping (i.e. affecting the dynamics of) each virtual node in one block to itself in the next block. In panel (b), the time delay is $\tau = T - \theta$, resulting in inner couplings where each virtual node maps backwards by θ; the first node of each block also affects the dynamics of the last node in the same block. Panels (c) and (d) depict cases where each node's dynamics are affected by two delayed

Figure 6.3: (Continued) states. In these panels, solid lines indicate a larger time delay, while dashed lines indicate a smaller delay. In panel (c), $\tau_1 = T$ and $\tau_2 = 2T$ ($\Delta\tau = T$), corresponding to the resonance case for single-step ahead prediction in multi-delay reservoir computing; this case is more susceptible to poor performance. In panel (d), the spacing between delays is $\Delta\tau = T + \theta$, with $\tau_1 = T$ and $\tau_2 = 2T + \theta$.

6.3 Multi-Delay Reservoir Computer's Performance for Different Inputs

In this Section, we examine this multi-delay reservoir computing for signals originating from various sources with distinct properties. We show that in some cases, choosing short spacing between delays outperforms large spacing, and vice versa. Given that many parameters affect the performance of the RC, we limit our study to parameters near the resonance regimes. The parameters are presented in Table 6.1. We used 10,000 data inputs for the training process, followed by testing on 5,000 data inputs for each input. The metric that we used to analyze the error is the normalized root mean square error:

$$\text{NRMSE} = \sqrt{\frac{1}{K}\frac{\sum_{i=1}^{K}(o(i) - \hat{o}(i))^2}{\text{VAR}(o)}}\,. \tag{6.7}$$

Here the sum is over the number of target data points. The variable $\hat{o}(i)$ represents the predicted values, while $o(i)$ corresponds to the target output values. Additionally we compared the linear memory capacity (MC) of the RC, i.e. the ability to recall the past inputs, for the single and multiple delay cases.

Our strategy to choose delay parameters and focus our exploration of the large parameter space is as follows. Our initial stability analysis guided our selection for short delay spacings. We aimed to investigate the differences between short delay spacings - where feedback destabilization is notably higher than in the single delay case - and large delay spacings, where the feedback strength's destabilization threshold is close to that of a single-delay system. As a case in point, we chose $\Delta\tau = 2.66$ for systems with two delays and $\Delta\tau = 1.6$ for systems with five delays, based on observed peaks of destabilization with the highest feedback strength for each case. For large delay spacings, we followed a more empirical approach. We initially plotted performance plots in the $\gamma - \beta$ space for different spacings near the clock-cycle value of 40 to find optimal parameters. After identifying these parameters, we then plotted the performance error for different spacings and selected the most favorable ones for Figures 4, 5, and 6 below.

6.3.1 Input from Lorenz Model

We begin our study with the Lorenz model, a chaotic dynamical system, characterized by the following equations:

$$\dot{x} = \sigma(y(t) - x(t)) \tag{6.8}$$

$$\dot{y} = -x(t)z(t) + \rho x(t) - y(t) \tag{6.9}$$

$$\dot{z} = x(t)y(t) - bz(t) \tag{6.10}$$

We used the standard parameters $\sigma = 10$, $\rho = 28$, $b = 8/3$, and sampled the data every 0.05 seconds. Initially, we focus on predicting the x component of the Lorenz system with a 1-step ahead prediction. The x component of the Lorenz system has the highest complexity and its auto-correlation function reveals little correlation between data points. The performance of the RC for this input is illustrated in Fig. 6.4. In this figure, we carefully selected the best parameters for RC by first plotting the performance in the $\gamma - \beta$ parameter space for various spacing between time delays close to the clock-cycle (not shown) and identifying the optimal β and γ values. Subsequently, we investigated the impact of different minimum time delays on the performance of RC, and the results are presented in Fig. 6.4.

It is evident in Fig. 6.4(a) that when $\tau_{min} < 15$ or so, the performance of the RC is superior for both large and small spacing between delays compared to the single delay case. However, as the minimum time delay value increases and approaches the clock cycle $T = 40$, the performance of the RC with single delay surpasses that of the RC with multiple delays with large spacing. Notably, the RC with 5 delays and small spacing exhibits the

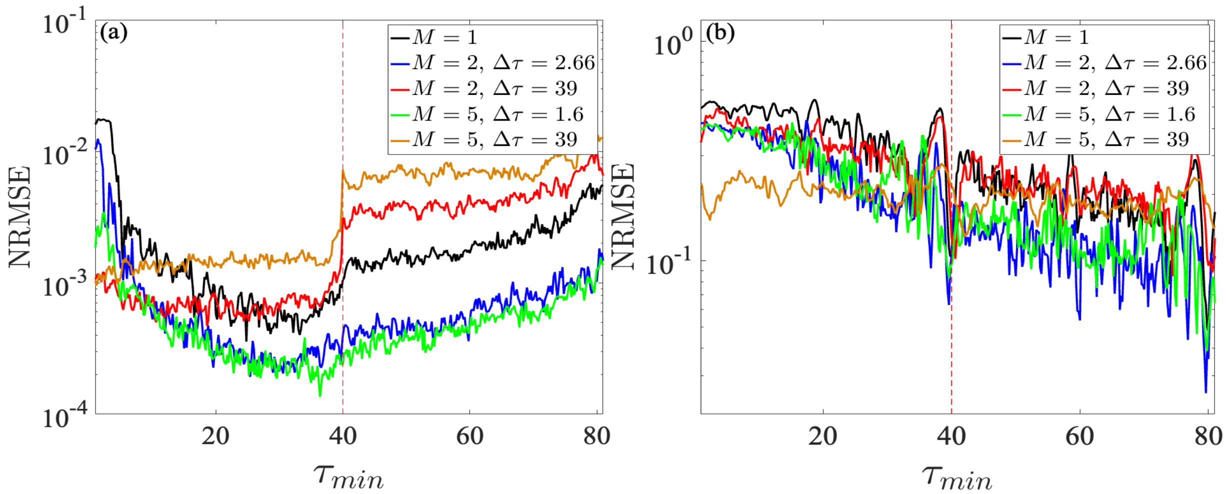

Figure 6.4: Multiple delay RC can improve prediction and cross-prediction compared to single delay RC. (a) One-step ahead time series prediction error of the lorenz x-component as a function of τ_{min} for 1, 2 and 5 time delay RC. (b) Same as in (a) but for one-step ahead cross-prediction of the lorenz z-component with the input being the lorenz x-component. The vertical red dashed lines indicate the value of the cycle time $T = 40$. Parameters are in Table 6.1 and $\theta = 0.2$.

best performance. In Fig. 6.4(b), we present the cross-prediction error for the z component of the Lorenz signal, with the x component as the input. Cross-prediction is feasible for the Lorenz system when using the x component as the input [175], but the errors are significantly larger, as seen here. The sharp drop in error is observed at $\tau_{min} = T - \theta$ and $\tau_{min} = 2T - \theta$.

When considering the z-component of the Lorenz system as the input, the trends observed are similar to those observed when the input was the x-component, as depicted in Fig. 6.5. As the minimum time delay approaches the clock cycle, the error increases across all cases. When the spacing between the delays is set to be equal to the clock cycle, i.e. at the resonance condition, the error increases, which is not observed in the case where the input is the lorenz x-component and predictions are made on the same component (not shown).

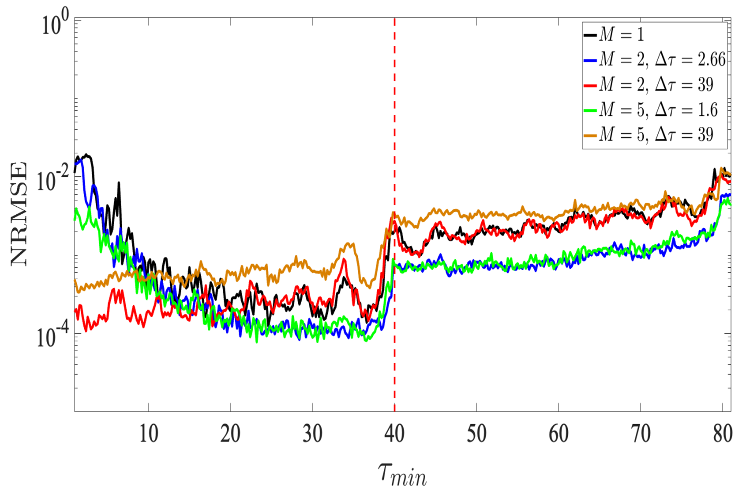

Figure 6.5: One-step ahead time series prediction of the lorenz z-component when the input is the lorenz z-component for different τ_{min}. The parameters used are in Table 6.1.

6.3.2 Input from Mackey-Glass Model

The Mackey-Glass equation is a nonlinear delay differential equation that exhibits high-dimensional chaotic behavior whenever the time delay is large compared to its response time. Here, we consider the standard parameters for the Mackey-Glass model of $a = 0.1$ and $b = 0.2$ and the time delay of 17 in the following equation:

$$\frac{dx}{dt} = -ax(t) + \frac{bx(t-\tau)}{1 + x^{10}(t-\tau)} \,. \tag{6.11}$$

For these parameters, the MG solution exhibits a much longer autocorrelation time than the Lorenz system used above. The differences in the prediction properties likely relate to the differing correlation times between these two systems. We illustrate in Fig. 6.6 the performance of the RC for the Mackey-Glass model input, where we try to predict 34 steps ahead for this equation ($o(i) = u(i + 34)$, where u represents the input and $o(i)$ represents the target output datapoint, which is equivalent to the input datapoint 34 steps ahead).

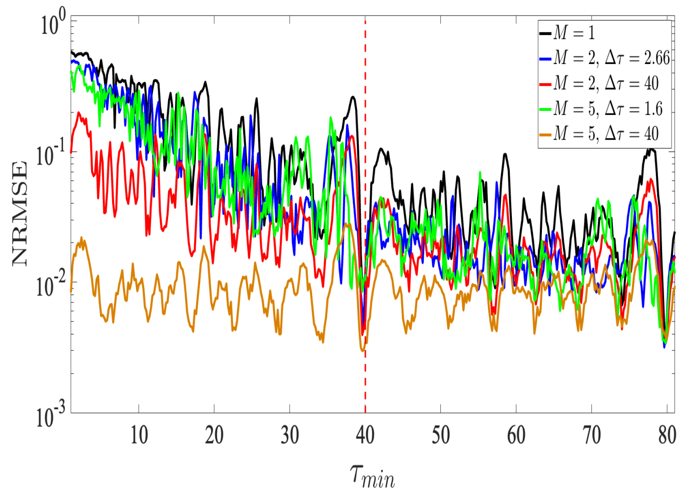

Figure 6.6: The normalized root mean square (NRMSE) for a 34-step ahead prediction of the Mackey-Glass time series. The spacing between delays, denoted as $\Delta\tau$, is given in the inset.

In contrast to the Lorenz time series, the use of large spacing between delays yields superior results for the Mackey-Glass input. As shown in Fig. 6.6, the prediction error for the Mackey-Glass time-series with 5 delays and a large delay spacing can be up to two orders of magnitude better than the error for the single delay case or for short delay spacing. However, it is worth noting that there is a specific case where the error drops drastically for both short delay spacing and the single delay case. This occurs when $\tau_{min} = 79.8$ (equivalent to $2T - \theta$), similar to the lorenz z when the input was lorenz x.

Table 6.1: Parameter values used for the simulation of Figs. 6.4-6.6

	lorenz x			lorenz z			MG		
	β	γ	$\Delta\tau$	β	γ	$\Delta\tau$	β	γ	$\Delta\tau$
$M = 1$	1.2	0.2	-	1.35	0.16	–	1.6	0.28	–
$M = 2$	2.3	0.24	2.66	2.2	0.16	2.66	3	0.2	2.66
$M = 2$	1.25	0.16	39	1.5	0.22	39	1.6	0.24	40
$M = 5$	4.1	0.24	1.6	3.5	0.12	1.6	5.5	0.16	1.6
$M = 5$	1.3	0.16	39	1.5	0.2	39	1.6	0.3	40

6.3.3 Narma10 Task

The Narma10 task is a standard task used to evaluate RC performance. It involves generating a discrete target output based on an input sequence u_k, which is randomly drawn from a uniform distribution in the interval [0,0.5]. The equation for the Narma10 task is:

$$o_{n+1} = 0.3o_n + 0.05o_n(\sum_{i=0}^{9} o_{n-i}) + 1.5u_{n-9}u_n + 0.1 \tag{6.12}$$

The above equation illustrates the dependency of target output values on past target output data. As noted earlier, a larger spacing between delays is observed to enhance prediction accuracy for correlated inputs, such as those in the Mackey-Glass model. To identify optimal time delays and spacing, we plotted the prediction error for the Narma10 task in Fig. 6.7. We considered minimum time delays ranging from 36 to 44 and $\Delta\tau$ values ranging from 76 to 84. The most accurate forecasting was achieved when $\Delta\tau = 2T \pm \theta$ and τ_{min} was equal to or close to T. A significant increase in forecasting error was observed at $\Delta\tau = 2T$ regardless of the value of τ_{min}. This error increase occurs periodically when $\Delta\tau$ is an integer multiple of the clock cycle, which corresponds to the resonance case for the multi-delay system (Fig. 6.3(c)).

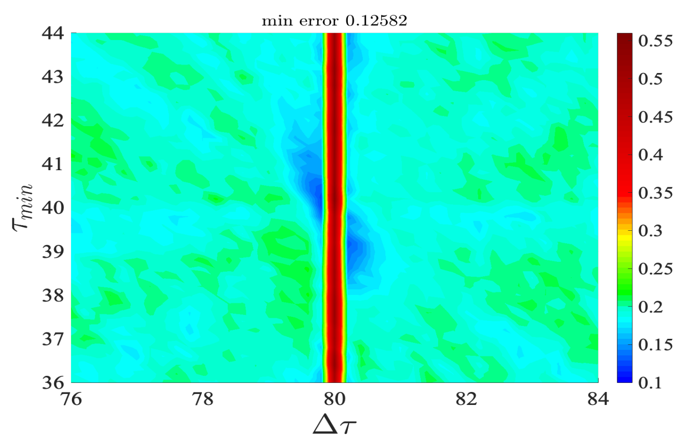

Figure 6.7: Prediction error of a RC system with five delays, as a function of the parameters τ_{min} and $\Delta\tau$, where the EOO parameters are $\beta = 1.35$ and $\gamma = 0.5$.

To evaluate the performance of the multi-delay system, we compare its memory capacity (MC) with that of the single delay case in Fig. 6.8. To analyze MC, the target is set equal to the ith input in the past ($o(k) = u(k-i)$, where u is the input) and the correlation between the target output and the recalled input is numerically computed:

$$m(i) = corr[o_i(k), \hat{o}_i(k)] \tag{6.13}$$

Results indicate that the multi-delay RC can recall up to 20 steps with a correlation between the recalled value and the target close to or equal to 1, while the single delay RC can only recall up to 11 steps before. The total memory capacity can be determined by calculating the area under the graph, which is clearly greater for the multi-delay RC. Overall, the results demonstrate that the multi-delay RC outperforms the single delay RC in terms of memory capacity.

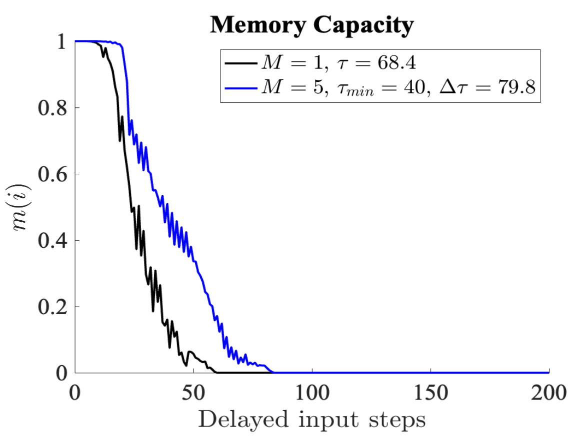

Figure 6.8: Memory capacity of a RC system for the Narma10 task, comparing single delay (black) and five delays (blue) schemes. For the single delay case, parameters were set to $\beta = 1.35$, $\gamma = 0.25$, and $\tau_{min} = 68.4$. For the five delays case, parameters were set to $\beta = 1.35$, $\gamma = 0.5$, $\tau_{min} = 40$, and $\Delta\tau = 79.8$. These parameters were chosen because they provide the lowest error on the respective Narma10 prediction tasks.

We further compared the performance of the RCs in the $\gamma - \beta$ parameter space in Fig. 6.9. We considered three cases: single delay ($\tau_{min} = 68.4$), five delays with short spacing between them ($\Delta\tau = 1.6$ and $\tau_{min} = 68.4$), and five delays with large spacing between them ($\Delta\tau = 79.8$ and $\tau_{min} = 40$). The values of τ for the single delay case, and τ_{min} for the five delays case with short spacing, are chosen such that to minimize the error. However, it remains unclear why these specific delay values yield the lowest error for both the single delay and multiple delay cases with short spacing. Like in the case of the Mackey-Glass input, we observe that the prediction for multiple delays with large spacing outperformed the other two cases. The system maintains a higher linear memory capacity (MC) in this scenario, resulting in higher prediction accuracy. The use of multiple delays with large spacing necessitates higher input scaling compared to the other cases, indicating the need for incorporating higher nonlinearity. Furthermore, employing multiple delays with large spacing offers the advantage of a broader range of parameter choices in the $\gamma - \beta$ space.

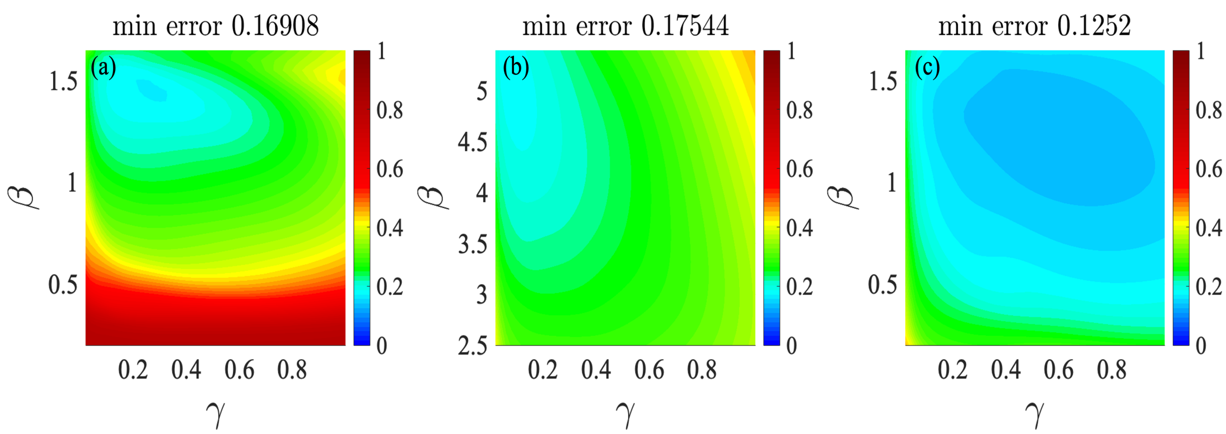

Figure 6.9: The Narma10 prediction error of a RC system for different reservoir configurations. (a) Prediction error for a single delay case ($M = 1$) and $\tau = \tau_{min} = 68.4$. (b) Prediction error for a five delay case ($M = 5$) with $\Delta\tau = 1.6$, and $\tau_{min} = 68.4$. (c) Prediction error for five delays ($M = 5$), $\Delta\tau = 79.8$, and $\tau_{min} = 40$. In each panel, the performance is shown for different input scaling and feedback strength values.

6.4 Discussion

While time delay RCs have demonstrated success in predicting chaotic time series through numerical and experimental approaches, identifying optimal time delays is critical for tackling more complex objectives, such as multi-step ahead prediction or prediction of individual signals within a mixed input signal. Further research is needed to explore ways of improving the performance of Reservoir Computing for more complicated prediction challenges. In particular, our results show that a thorough understanding of the input data properties is essential to successfully implement a multi-time delay RC for time series prediction.

Predicting multiple steps ahead for high-order complex signals like the Lorenz signal can be challenging. When predicting one step ahead, selecting a time delay equal to the clock cycle of the RC often leads to poor outcomes. However, the optimal time delay may vary depending on the correlation between the input and output. For example, in the case of cross-prediction where the input is lorenz x and the target is lorenz z, We found that the resonance shifts to a smaller time delay value, and significant improvement is observed at $\tau = T$, as shown in Fig. 6.4. Previous studies have shown that using a delayed input method can improve RC performance for cross-prediction, and the lowest error can be achieved by delaying the input by multiple steps due to the correlation between the x component and the z component [175].

In the context of the multi-delay reservoir computing analyzed in our work, it is more crucial to choose delays with spacing unequal to the clock cycle (see Fig. 6.7). For the Narma10 task, we observed that the error decreased significantly around the resonance case. However, we should note that this might not be true for multiple step-ahead prediction.

In general, our results reveal that the reservoir computing prediction performance is expected to improve as the number of delays increases. This is often true, especially when the minimum time delay approaches the resonance condition value found in the single delay case. However, there may be values of the single time delay for which reservoir computer exhibits performance comparable to multi-delay systems. Overall, it is likely that a delay configuration can be found for the multi-delay system which presents a broader parameter space compared to the single delay case. This increased parameter space enhances the chances of achieving optimal reservoir performance, depending on the specific properties of the task.

While choosing the proper time delay is crucial, it's not the only factor that can enhance system performance. One potential approach to enhancing memory capacity involves adding layers to the RC architecture. By considering the same number of virtual nodes for each layer, the total number of nodes increases, which in turn results in a reduction in prediction error [169]. Furthermore, we have observed that feeding the input into multiple parallel lasers and then collecting the states of the virtual nodes from all lasers into a single matrix can further enhance the RC's performance [91].

It is interesting to note that increasing the complexity of the reservoir's architecture, such as using multi-layers, can result in a greater difference in error between single-delay and multi-delay systems (unpublished data). Preliminary results indicate that even when a mixture of signals is present, with the dynamically simpler signal being the dominant one in the mixture, the reservoir can still predict the more complex signal with acceptable accuracy.

Finally, our results only apply to the case where delays are picked with a uniform spacing from one another. Small deviations from this scheme lead to similar results (not shown), but it is clear that it would be of interest to investigate whether a multi-delay RC with random delays leads to better results. There are many parameters underlying the operation of these RCs. While we have presented dominant features of their performance, a full description of the dependence of the error on the type and parameters of the node dynamics as well as the type and parameters of the external input is beyond the scope of the present work, and may itself benefit from machine learning techniques for parameter tuning.

6.5 Predicting Signals that are Linearly Mixed

In the final section of this chapter, we present some preliminary findings from ongoing research that are not included in the paper that we submitted. They form the basis for another paper.

Classification of individual signals that comprise a signal mixture can be challenging. It is an interesting topic with brain-related examples such as the cocktail party problem and redundant input cancellation [146]. Reservoir computers are capable of embedding input signals into higher dimensions due to the dynamics of their interacting nodes, making them good candidates for tackling this problem. For example, mutually coupled semiconductor lasers were used to classify sinusoidal and square wave signals with high accuracy using reservoir computing [176].

However, predicting two separate chaotic signals can be more challenging, since the RC must somehow separate and individually predict the original time series that are in the mixture. In this section, we report on an experiment that we conducted to evaluate the performance of a reservoir computer on signal mixtures. This problem has been studied in the context of an echo state network in [162], with the input $u = \sqrt{s}u_1 + \sqrt{1-s}u_2$, where u_1 and u_2 are two different independent signals, and s is a mixing ratio. The goal is to predict $o_1(k) = u_1(k+1)$ and $o_2(k) = u_2(k+1)$. For simplicity we limit our analysis to the simple case where only two signals are mixed linearly, and the resulting mixture is fed to the RC. It would likely be easier to feed two separate mixtures (as obtained from a 2x2 mixing matrix) to the RC, although that would require more choices about how to drive the RC with two such signals.

We considered two different cases. In both cases, we chose the dominant signal to be the lorenz x, since it's not possible to predict both signals when the signal with lower complexity is the dominant signal.

Table 6.2: Parameter values used for the simulation of the Figs. 6.10 and 6.11

	lorenz x + lorenz z			lorenz x + MG		
	β	γ	$\Delta\tau$	β	γ	$\Delta\tau$
$M=1$	1.3	0.2	-	1.2	0.32	–
$M=2$	2.6	0.16	2.66	3	0.2	2.66
$M=2$	1.5	0.48	40	1.4	0.2	40
$M=5$	4.7	0.16	1.6	5.1	0.12	1.6
$M=5$	1.5	0.52	40	1.2	0.4	40

We plotted the prediction signal for the mixture of the lorenz x (u_1) and lorenz z (u_2) in Fig. 6.10. In general, all cases of multiple delays work better than the single delay case. For $\tau_{min} < T$, the large spacing is the superior one, but at $\tau_{min} = T$, there is a sharp enhancement for short spacing between the delays for both $M = 2$ and $M = 5$, similar to the trend that we saw earlier for cross prediction.

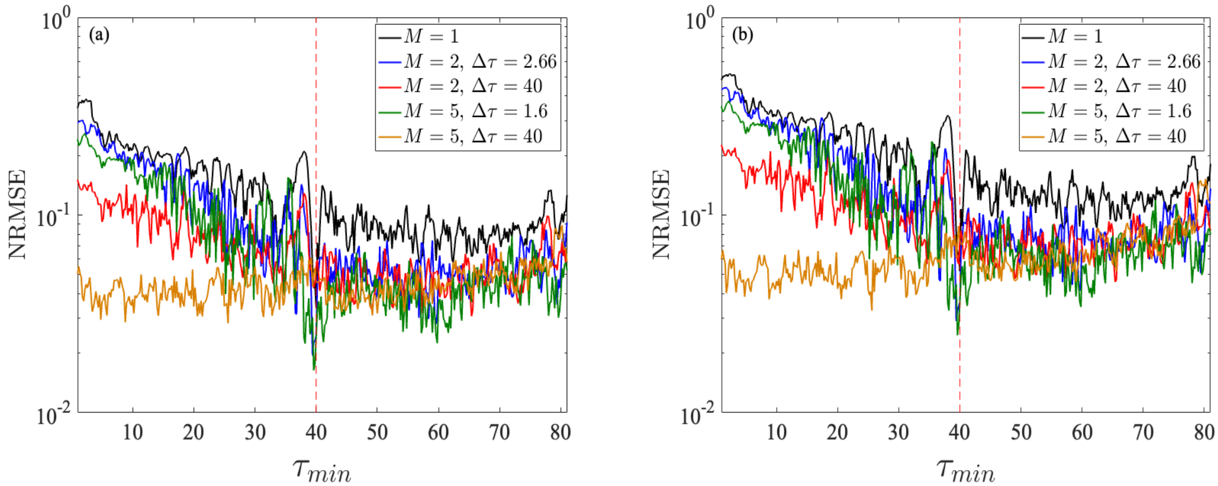

Figure 6.10: Prediction errors of a RC system for individual signals comprising the input, with an input mixing ratio of $s = 0.7$: (a) for the Lorenz x signal, and (b) for the Lorenz z signal. The rest of the parameters for the two cases are summarized in Table 6.2.

As a second example, we consider the case where two totally unrelated signals, namely, a Mackey-Glass and a lorenz x, are mixed and injected into the reservoir. In Fig. 6.11, we observe that the reservoir was able to predict the second signal with weaker intensity for an acceptable error (NRMSE$\approx$ 0.4) for a 5-delay system with large delay spacing, and this for many different minimum time delays. The lowest error for the multiple delay case was approximately 0.42, while for the single delay case it was approximately 0.49 for the prediction of the Mackey-Glass input. Interestingly, due to the presence of the Mackey-Glass input, the large spacing between delays worked better for prediction, while in the previous section without signal mixtures, this architecture performed much worse than the short spacing for lorenz x prediction.

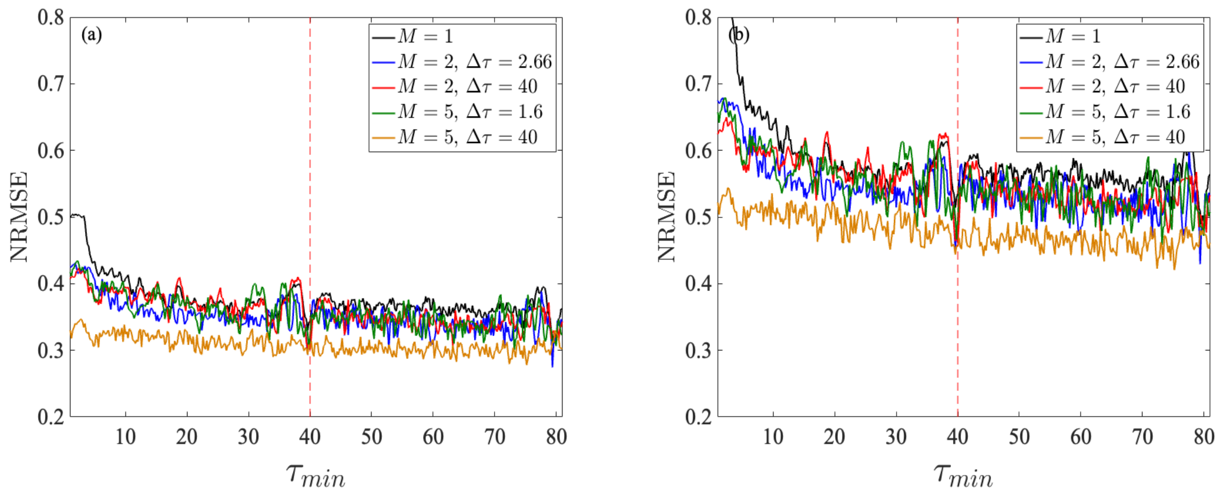

Figure 6.11: Prediction errors of a RC system for individual signals comprising the input, with an input mixing ratio of $s = 0.7$: (a) for the Lorenz x signal, and (b) for the Mackey-Glass time series.

In general, our preliminary results show that the simultaneous prediction of both signals works well for large spacing between delays. We mentioned that it is not possible to predict the more complex signal when it does not dominate. Interestingly, another study currently underway finds that adding layers to the reservoir (with multiple delays in each layer) can in fact help in the prediction of the more complex signal when it does not dominate the mixture. Furthermore, considering a multi-level mask instead of a binary mask might also increase the ability to separate such inputs. Improving these capabilities might help to better construct and separate the phase space attractors of the individual signals, similar to what has been shown in [177].

Chapter 7

Conclusion and Summary

Throughout this thesis, we comprehensively analyzed the impact of multiple delays on the dynamics of various nonlinear delay differential equations. The equations we studied cover different real-world systems, from laser systems to neuroscience to physiological feedback models.

In Chapter 3, we explored the impact of multiple delays on the dynamics of semiconductor lasers with optical feedback. We used various methods, including ACF, Kolmogorov-Sinai entropy, and permutation entropy, to quantify the chaos in this system. The highest nonlinearity exists in semiconductor lasers with optical feedback when the ACF values around the time delay are minimized. Time delay signature in the ACF of the intensity time series of the semiconductor laser with optical feedback poses a challenge for applications such as random bit generator devices, which require minimizing this peak to prevent detection of the signature. Previous studies have shown that signatures appear in the ACF around the average of the time delays and the individual delays for the Lang-Kobayashi model with two delays. We found that even with a few delays randomly drawn from the uniform distribution, despite the fact that delayed states affect the system's dynamics, the ACF of the intensity did not exhibit a clear signature of time delays [27].

However, as we further increased the number of delays for any fixed feedback strength, we observed a transition from highly complex dynamics to simpler ones, such as torus, limit cycle, and stable fixed point. In the case of the torus attractor, we observed two main time scales: the relaxation oscillation period and the average of the time delays. As the number of delays approached a very large limit, we thus expected to observe, and did observe, a limit cycle (with the relaxation oscillation frequency) and a stable fixed point, respectively. Despite excluding noise in our simulations, we found that the addition of noise did not impact our findings regarding the changes in complexity as the number of delays and feedback strength varied. To assess the complexity behavior of the system in the presence of noise, we tracked changes in the value of the time delay signature obtained from the ACF (not shown).

To further examine the relationship between the unpredictability of the dynamics of the semiconductor laser with optical feedback and the number of delays, we obtained Lyapunov exponent estimates by extending the Pseudo-spectral differentiation for multiple delays. This method involved a series of ODEs between each pair of delays to capture the system's dynamical evolution between delayed and current states. By using more Chebyshev polynomial nodes, higher accuracy could be achieved.

The degree of unpredictability of the LK model with multiple delays showed a non-monotonic dependency on the number of delays. Multiple delays can destroy the signature in the ACF, a useful property for preventing approximate periodicity in the random bit sequence generated by a semiconductor laser with optical feedback. Yet the highest value of the Kolmogorov-Sinai entropy of the multiple delay case was not significantly higher than that for the single delay case (Fig. 3.8(b)). Whether higher Kolmogorov-Sinai entropy can be obtained with other forms of delays and delay distributions has yet to be explored.

Moreover, we investigated the Lang-Kobayashi model in the form of distributed delay differential equation with a uniform kernel. We observed that the chaotic dynamics disappear at a specific points as the width of the delay distribution increases (as illustrated in Fig. 3.4(b)). These stable regimes arise due to the dynamics of the phase equation, and they occur periodically as the kernel width increases. This phenomenon can also be observed in the LK model with discrete delays considering a unique spacing between delays and adding more delays. In between these non-chaotic regimes, the dynamics tend to be chaotic with high entropy. However, further increasing the width of the delay distribution results in a decrease in the degree of complexity, and there would be no chaotic dynamics at some limit. Notably, neither regular nor random delays exhibited chaotic dynamics as the number of delays approached a large limit. The stabilized regimes at specific kernel widths, or in the case of multiple discrete delays with a unique spacing between them, in the LK model might make them proper regimes for implementing reservoir computing, as by definition, the reservoir computer operates the best at the edge of the chaos.

In summary, the dynamics of the LK model with a large number of delays closely resemble those of the distributed delay case when the spacings between delays are identical and sufficiently small. In scenarios where delays are selected randomly from uniform distributions, we consistently observed a transition to simpler dynamics as the number of delays increased. This observation could aid in cancelling unwanted fluctuations in the dynamics of semiconductor lasers with optical feedback. In cases where enhanced chaos is advantageous in certain applications requiring a high degree of unpredictability, the presence of multiple delays can help achieve this goal. However, signatures of the relaxation oscillation period may still be present.

In addition to our analysis of semiconductor lasers with optical feedback in Chapter 3, we also investigated the impact of delays from a uniform distribution on first-order nonlinear time-delay systems in Chapters 3 and 4. Specifically, we showed that for the Mackey-Glass model, when picking delays randomly while keeping the average of the delays approximately fixed, increasing the number of delays or the width of the delay distribution produces a monotonous decrease in complexity followed by some abrupt collapse. However, this monotonic decrease in complexity may not be true for all first-order nonlinear time delay systems, such as the Ikeda model. The impact of adding delays on the complexity of nonlinear systems is highly dependent on the feedback term's nonlinear function. Similar to the Lang-Kobayashi model, adding a few delays to the Ikeda-type equation might initially enhance chaos, followed by a decrease in complexity. The non-oscillatory nature of the feedback function in the Mackey-Glass equation might explain the lack of increase in entropy. However, we note that we did not extensively explore the effect of feedback strength on the complexity of the Mackey-Glass model; there may be other feedback choices that increase complexity when delays are added.

In Chapter 4, we delved deeper into the influence of time delays in two primary first-order nonlinear delay differential equations: the Mackey-Glass model and the Electro-optic Oscillator model (an Ikeda-type equation). In Chapter 3, we observed complexity collapse when the average of the time delays was approximately fixed upon adding more delays. However, in this case, the minimum time delay decreased with respect to the response time, resulting in a decrease in entropy. Therefore, in Chapter 4, we tackled the problem differently by selecting delays to ensure the minimum delay remained constant while increasing the average of the delays with the addition of more delays. Our simulations revealed that the suppression of chaos is still possible by adding delays, especially for the Mackey-Glass model (as demonstrated in Fig. 4.4).

The impact of time delays on the dynamics of these systems can be better understood by examining the characteristic equation. For first-order nonlinear DDEs, the characteristic equation shows that increasing the number of delays results in additional modes in solutions, with the peaks of these modes spaced proportionally to the spacing between delays. The way the roots of the characteristic equation behaved led us to investigate the case where the number of delays is fixed, and increase the average of the delays by varying the spacing between delays. In this case, when the spacing increases, the roots with the rightmost positive real part move toward the negative side and in general, all roots get closer to the origin. We also demonstrated that roots at the boundary between the stable and unstable regions began to fluctuate by varying the spacing between delays. Our observations were further supported by our numerical study of the bifurcation, which revealed windows of stable fixed point and limit cycle behaviour between the chaotic windows as we increased the width of the distribution of delays, even for ten delays (see Fig 4.8). The more delays are present in these systems, the higher the probability of stable fixed points appearing in the limit of large enough spacing between the delays.

Furthermore, in Chapter 4 we showed that the trend of the Kolmogorov-Sinai entropy was very similar to the summation of the unstable modes, a behavior previously shown in [17]. In this thesis, we used this similarity as a proxy for calculating the complexity. How the complexity of the first-order nonlinear DDEs depends on the ratio of the time delays to response time and how it can be related to the density of delays deserves more attention in future investigations. Moreover, for the single delay case, this system can be compared to a map-like behavior [132]; whether this can also be done in the limit of the large spacing between delays has yet to be discovered.

What time scales govern the dynamics of multi-delay first-order nonlinear DDEs requires further investigation. Our permutation entropy analysis showed that the dominant time scale is not related to the time delays nor the spacing between them. Future exploration could help determine what drives these regimes' dynamics. In single-time delay first-order nonlinear systems, the ratio of the time delay to response time can reveal much helpful information. Finding the dominant time scales in the first-order nonlinear multi-delay system might help us draw links between the time scale of the intrinsic dynamical response, the mean delay and standard deviation of the delay distribution.

Chapter 5 was motivated by wanting to see multi-delay complexity collapse in more sophisticated systems such as neural networks. For example, we considered the spiking neural network with an 80/20 E-I ratio. Previous research has shown that time delays can induce Hopf bifurcations in spiking recurrent neural networks, altering their dynamics significantly [20].

We demonstrated in the network we studied a synchronous spiking activity in the presence of noise for a large enough delay. However, incorporating small time delays resulted in chaotic dynamics and irregular fluctuations. Increasing the number of delays did not suppress the chaotic behaviour, i.e. we could not see the phenomenon we had previously found in the Lang-Kobayashi model and the first-order nonlinear time-delay systems. To further explore this issue, we introduced another connection from a longer pathway to all neurons from an inhibitory population. The dynamics of this network with the additional long delayed negative feedback were highly complex. The novel behaviour that stood out consists in random periods of synchronous activity within the chaotic dynamics. Spiking activity decreased significantly during these periods, and high-frequency, low-amplitude oscillations emerged. The occurrence of these synchronous activities depended heavily on the global feedback time delay and strength. We demonstrated that with stronger global feedback, the distribution of the intervals between epochs of activity became more Poissonian.

During the synchronous activity, periodic perturbations significantly impacted the system's dynamics, causing it to become trapped in the synchronous activity regime. Even after the external stimuli were removed, the high-frequency, low-amplitude oscillations persisted for an uncertain amount of time before eventually returning to chaotic dynamics.

Additionally, we found that this type of neural network, with its global feedback inhibition on top of short-delay local recurrent excitatory and inhibitory feedback, is capable of exhibiting multi-delay complexity collapse in the presence of multiple local delays with a uniform distribution. In such cases, there is transient chaos, but eventually, the network's dynamics settle into simple oscillations.

We should also emphasize that with global excitatory feedback, the dynamics stabilized to a fixed point (not shown). none of the behaviors observed with delayed global inhibitory feedback were evident. We also explored scenarios where the synaptic weights are incorporated inside the activation function, reminiscent of the approach in the Wilson-Cowan model. In this model, the influence of synaptic connections is considered before the values undergo activation—a pre-activation influence. Notably, under this structure, the suppression of complex dynamics became feasible when combined with multiple local time delays and global inhibitory delayed feedback.

In summary, in Chapter 5 we explored various methods for suppressing chaotic activity, which can be achieved with large time delays in the absence of global feedback, or via external stimuli and multiple local feedback time delays in the presence of global feedback time delay. However, the cause and properties of abrupt synchronous activities within the chaotic dynamics in the presence of global feedback time delay still requires further investigation. Additionally, the duration of these synchronous activities induced by stimulation depends on several factors, such as the timing, frequency, and amplitude of the stimulation, as well as the duration of the activation. This phenomenon is complex, and its underlying mechanisms are far from being fully understood.

Chapter 6 focuses on the critical role of multiple time delays in time delay reservoir computing using the Electro-Optic Oscillator model. We investigated how time delays influence the performance of the reservoir for different tasks. Our analysis revealed that depending on the task, various architectures might be employed to minimize prediction error.

Our analysis revealed that the addition of delays when there is a band-pass filter (which causes the Electro-Optic Oscillator model to have one steady state) creates a stabilized regime, and destabilization requires a higher gain for small delay spacing. However, for large delay spacings, the gain threshold for destabilizing is the same as for a single delay, but the eigenvalue spectra differ.

The resonance phenomenon in delay reservoir computing has been extensively studied in the literature. Resonances have been linked to eigenvalue properties. For example, it has been suggested that in order to avoid poor predictions, the time delay should differ from the clock cycle [174]. While this concept holds true in general, our analysis in Chapter 6 revealed cases that violate the time delay-clock cycle resonance. For instance, we observed an increase in error around the time delay equal to the clock cycle for the Lorenz x component prediction, but for cross-prediction for the Lorenz z (where the input is Lorenz x, but the target is Lorenz z), the minimum error occurred when the time delay was equal to the clock cycle (shown in Fig. 6.4(b)). However, we note that we selected the parameters in Fig. 6.4 to obtain the lowest error for Lorenz x prediction. We should also note that a short spacing between delays and a high gain coefficient work better than a single delay for a single-step-ahead prediction of the Lorenz time series. Our analysis in Chapter 6 sheds light on the complexity of the resonance phenomenon in delay reservoir computing and highlights the need for a task-specific approach to achieve optimal performance.

Our analysis revealed that for tasks such as Narma10 (a difference equation) and multiple steps ahead prediction for Mackey-Glass (a DDE) (where in both cases, the input data is determined from past input data), large spacing between delays performed better than a short spacing. Specifically, for the Narma10 task, we observed a significant (5 percent) reduction in forecasting error with a larger spacing. Furthermore, for Mackey-Glass, using multiple delays with large spacings decreased the forecasting error in comparison to the single delay case, with one notable exception; When the time delay was set to a specific value ($\tau_{min} = 2T - \theta$), the difference in error between the single delay case and the multiple delay case with large spacing between delays was very small.

While the resonance condition was observable for the Narma10 task, we found that for multi-steps ahead prediction for Mackey-Glass input, the resonance shifted to a smaller time delay value. Our findings suggest that task-specific approaches are necessary to achieve optimal performance in delay reservoir computing. We gained important insights that can inform future research in this field by investigating the impact of time delay spacings on different tasks. Whether all the methods reported for improving the performance of the reservoir computing are true for all tasks should be explored more, for example, using a multi-level mask.

In the final part of our study, we presented some preliminary results on our ongoing work aimed at predicting individual signals from a mixture that feeds into a nonlinear node. This task becomes particularly challenging when the dominant signal is simpler than the other. Our initial findings indicate that using multi-layers with multiple delays in each layer significantly improves performance compared to multilayered reservoir computing with a single delay in each layer, which only marginally reduces prediction error. However, demixing becomes especially difficult when the two signals originate from the same source, such as two chaotic x-components from Lorenz dynamical systems. Unfortunately, our simulations have not yet produced satisfactory predictions for this scenario, but we continue to work on improving our methods.

Our study provided valuable insights into the effects of multiple delays drawn from a uniform distribution on various dynamical systems with time delays. We highlighted the importance of selecting delays carefully, as this can significantly alter system dynamics and influence practical applications. Further research can expand on our findings by exploring the underlying mechanisms in greater detail and testing our methods experimentally.

References

[1] G. Orosz, R. E. Wilson, and G. Stépán, "Traffic jams: dynamics and control," *Philosophical Transactions of the Royal Society A: Mathematical, Physical and Engineering Sciences*, vol. 368, no. 1928, pp. 4455–4479, 2010.

[2] L. Davis, "Modifications of the optimal velocity traffic model to include delay due to driver reaction time," *Physica A: Statistical Mechanics and its Applications*, vol. 319, pp. 557–567, 2003.

[3] J. G. Milton, T. Ohira, J. L. Cabrera, R. M. Fraiser, J. B. Gyorffy, F. K. Ruiz, M. A. Strauss, E. C. Balch, P. J. Marin, and J. L. Alexander, "Balancing with vibration: A prelude for "drift and act" balance control," *PLOS ONE*, vol. 4, pp. 1–11, 10 2009.

[4] J. Milton, J. L. Cabrera, T. Ohira, S. Tajima, Y. Tonosaki, C. W. Eurich, and S. A. Campbell, "The time-delayed inverted pendulum: Implications for human balance control," *Chaos: An Interdisciplinary Journal of Nonlinear Science*, vol. 19, 06 2009. 026110.

[5] V. Annovazzi-Lodi, G. Aromataris, M. Benedetti, and S. Merlo, "Private message transmission by common driving of two chaotic lasers," *IEEE Journal of Quantum Electronics*, vol. 46, no. 2, pp. 258–264, 2010.

[6] A. Uchida, K. Amano, M. Inoue, K. Hirano, S. Naito, H. Someya, I. Oowada, T. Kurashige, M. Shiki, S. Yoshimori, K. Yoshimura, and P. Davis, "Fast physical random bit generation with chaotic semiconductor lasers," *Nature Photonics*, vol. 2, no. 12, pp. 728–732, 2008.

[7] C. Gros, "Entrenched time delays versus accelerating opinion dynamics: are advanced democracies inherently unstable?," *The European Physical Journal B*, vol. 90, no. 11, p. 223, 2017.

[8] S. Guillouzic, I. L'Heureux, and A. Longtin, "Small delay approximation of stochastic delay differential equations," *Phys. Rev. E*, vol. 59, pp. 3970–3982, Apr 1999.

[9] T. D. Frank, "Delay fokker-planck equations, novikov's theorem, and boltzmann distributions as small delay approximations," *Phys. Rev. E*, vol. 72, p. 011112, Jul 2005.

[10] A. Longtin, "Stochastic delay-differential equations," in *Complex Time-Delay Systems* (F. Atay, ed.), Understanding Complex Systems, pp. 109–146, Berlin, Heidelberg: Springer, 2009.

[11] D. V. Ramana Reddy, A. Sen, and G. L. Johnston, "Time delay induced death in coupled limit cycle oscillators," *Phys. Rev. Lett.*, vol. 80, pp. 5109–5112, Jun 1998.

[12] T. Erneux, *Applied Delay Differential Equations*. New York: Springer-Verlag, 2009.

[13] K. Pyragas, "Continuous control of chaos by self-controlling feedback," *Physics Letters A*, vol. 170, no. 6, pp. 421–428, 1992.

[14] F. M. Atay and A. Hutt, "Neural fields with distributed transmission speeds and long-range feedback delays," *SIAM Journal on Applied Dynamical Systems*, vol. 5, no. 4, pp. 670–698, 2006.

[15] F. M. Atay, "Distributed delays facilitate amplitude death of coupled oscillators," *Phys. Rev. Lett.*, vol. 91, p. 094101, Aug 2003.

[16] A. Thiel, H. Schwegler, and C. W. Eurich, "Complex dynamics is abolished in delayed recurrent systems with distributed feedback times," *Complexity*, vol. 8, no. 4, pp. 102–108, 2003.

[17] B. Mensour and A. Longtin, "Power spectra and dynamical invariants for delay-differential and difference equations," *Physica D: Nonlinear Phenomena*, vol. 113, no. 1, pp. 1 – 25, 1998.

[18] B. Mensour and A. Longtin, "Synchronization of delay-differential equations with application to private communication," *Physics Letters A*, vol. 244, no. 1, pp. 59–70, 1998.

[19] Y. Xu, M. Zhang, L. Zhang, P. Lu, S. Mihailov, and X. Bao, "Time-delay signature suppression in a chaotic semiconductor laser by fiber random grating induced random distributed feedback," *Opt. Lett.*, vol. 42, pp. 4107–4110, Oct 2017.

[20] A. Hutt, A. Mierau, and J. Lefebvre, "Dynamic control of synchronous activity in networks of spiking neurons," *PLOS ONE*, vol. 11, pp. 1–15, 09 2016.

[21] V. E. Bondarenko, "Information processing, memories, and synchronization in chaotic neural network with the time delay," *Complexity*, vol. 11, no. 2, pp. 39–52, 2005.

[22] C. S. Herrmann, M. M. Murray, S. Ionta, A. Hutt, and J. Lefebvre, "Shaping intrinsic neural oscillations with periodic stimulation," *Journal of Neuroscience*, vol. 36, no. 19, pp. 5328–5337, 2016.

[23] S. Rich, A. Hutt, F. K. Skinner, T. A. Valiante, and J. Lefebvre, "Neurostimulation stabilizes spiking neural networks by disrupting seizure-like oscillatory transitions," *Scientific Reports*, vol. 10, p. 15408, Sep 2020.

[24] S. H. Park, J. D. Griffiths, A. Longtin, and J. Lefebvre, "Persistent entrainment in non-linear neural networks with memory," *Frontiers in Applied Mathematics and Statistics*, vol. 4, p. 31, 2018.

[25] J. Wang, B. Deng, T. Gao, J. Wang, G. Yi, and R. Wang, "Frequency-dependent response in cortical network with periodic electrical stimulation," *Chaos: An Interdisciplinary Journal of Nonlinear Science*, vol. 30, no. 7, p. 073130, 2020.

[26] L. Appeltant, M. C. Soriano, G. Van Der Sande, J. Danckaert, S. Massar, J. Dambre, B. Schrauwen, C. R. Mirasso, and I. Fischer, "Information processing using a single dynamical node as complex system," *Nature Communications*, vol. 2, no. 1, pp. 1–6, 2011.

[27] S. K. Tavakoli and A. Longtin, "Multi-delay complexity collapse," *Phys. Rev. Research*, vol. 2, p. 033485, Sep 2020.

[28] S. Kamyar Tavakoli and A. Longtin, "Dynamical invariants and inverse period-doubling cascades in multi-delay systems," *Chaos: An Interdisciplinary Journal of Nonlinear Science*, vol. 31, no. 10, p. 103129, 2021.

[29] S. K. Tavakoli and A. Longtin, "Complexity collapse, fluctuating synchrony, and transient chaos in neural networks with delay clusters," *Frontiers in Systems Neuroscience*, vol. 15, 2021.

[30] Y. Xie, L. Chen, Y. M. Kang, and K. Aihara, "Controlling the onset of hopf bifurcation in the hodgkin-huxley model," *Phys. Rev. E*, vol. 77, p. 061921, Jun 2008.

[31] L. Kocarev and U. Parlitz, "General approach for chaotic synchronization with applications to communication," *Phys. Rev. Lett.*, vol. 74, pp. 5028–5031, Jun 1995.

[32] A. Argyris, D. Syvridis, L. Larger, V. Annovazzi-Lodi, P. Colet, I. Fischer, J. García-Ojalvo, C. R. Mirasso, L. Pesquera, and K. A. Shore, "Chaos-based communications at high bit rates using commercial fibre-optic links," *Nature*, vol. 438, pp. 343–346, Nov. 2005.

[33] C. Zhou and C.-H. Lai, "Extracting messages masked by chaotic signals of time-delay systems," *Phys. Rev. E*, vol. 60, pp. 320–323, Jul 1999.

[34] D. S. Coffey, "Self-organization, complexity and chaos: The new biology for medicine," *Nature Medicine*, vol. 4, no. 8, pp. 882–885, 1998.

[35] N. Macdonald, *Cambridge studies in mathematical biology: Biological delay systems: Linear stability theory series number 9.* Cambridge, England: Cambridge University Press, Jan. 2008.

[36] A. Longtin, J. G. Milton, J. E. Bos, and M. C. Mackey, "Noise and critical behavior of the pupil light reflex at oscillation onset," *Phys. Rev. A*, vol. 41, pp. 6992–7005, Jun 1990.

[37] A. Hastings, C. L. Hom, S. Ellner, P. Turchin, and H. C. J. Godfray, "Chaos in ecology: Is mother nature a strange attractor?," *Annual Review of Ecology and Systematics*, vol. 24, no. 1, pp. 1–33, 1993.

[38] K. McCann, A. Hastings, and G. R. Huxel, "Weak trophic interactions and the balance of nature," *Nature*, vol. 395, pp. 794–798, October 1998.

[39] M. H. Adhikari, E. A. Coutsias, and J. K. McIver, "Periodic solutions of a singularly perturbed delay differential equation," *Physica D: Nonlinear Phenomena*, vol. 237, no. 24, pp. 3307–3321, 2008.

[40] S. Madruga, S. Boccaletti, and M. A. Matías, "Effect of a variable delay in delayed dynamical systems," *International Journal of Bifurcation and Chaos*, vol. 11, no. 11, pp. 2875–2880, 2001.

[41] D. Müller-Bender and G. Radons, "Laminar chaos in systems with quasiperiodic delay," *Phys. Rev. E*, vol. 107, p. 014205, Jan 2023.

[42] T. Jüngling, A. Gjurchinovski, and V. Urumov, "Experimental time-delayed feedback control with variable and distributed delays," *Phys. Rev. E*, vol. 86, p. 046213, Oct 2012.

[43] W.-H. Kye, M. Choi, S. Rim, M. S. Kurdoglyan, C.-M. Kim, and Y.-J. Park, "Characteristics of a delayed system with time-dependent delay time," *Phys. Rev. E*, vol. 69, p. 055202, May 2004.

[44] T. Cassidy, "Distributed delay differential equation representations of cyclic differential equations," *SIAM Journal on Applied Mathematics*, vol. 81, no. 4, pp. 1742–1766, 2021.

[45] Y. N. Kyrychko, K. B. Blyuss, and E. Schöll, "Amplitude and phase dynamics in oscillators with distributed-delay coupling," *Philosophical Transactions of the Royal Society A: Mathematical, Physical and Engineering Sciences*, vol. 371, no. 1999, p. 20120466, 2013.

[46] Y. N. Kyrychko, K. B. Blyuss, and E. Schöll, "Synchronization of networks of oscillators with distributed delay coupling," *Chaos: An Interdisciplinary Journal of Nonlinear Science*, vol. 24, no. 4, p. 043117, 2014.

[47] B. Rahman, K. B. Blyuss, and Y. N. Kyrychko, "Dynamics of neural systems with discrete and distributed time delays," *SIAM Journal on Applied Dynamical Systems*, vol. 14, no. 4, pp. 2069–2095, 2015.

[48] J. Be'lair, *Population models with state-dependent delays*, vol. 131 of *Lecture notes in pure and applied mathematics*. Dekker. New York, 1991.

[49] R. C. Calleja, A. R. Humphries, and B. Krauskopf, "Resonance phenomena in a scalar delay differential equation with two state-dependent delays," *SIAM Journal on Applied Dynamical Systems*, vol. 16, no. 3, pp. 1474–1513, 2017.

[50] N. Brunel, *Principles of Neural Coding*, ch. 25, pp. 489–512. CRC Press, Boca Raton, 2013.

[51] E. Wall, F. Guichard, and A. R. Humphries, "Synchronization in ecological systems by weak dispersal coupling with time delay," *Theoretical Ecology*, vol. 6, pp. 405–418, Nov 2013.

[52] U. Ernst, K. Pawelzik, and T. Geisel, "Synchronization induced by temporal delays in pulse-coupled oscillators," *Phys. Rev. Lett.*, vol. 74, pp. 1570–1573, Feb 1995.

[53] A. C. Martí and C. Masoller, "Delay-induced synchronization phenomena in an array of globally coupled logistic maps," *Phys. Rev. E*, vol. 67, p. 056219, May 2003.

[54] B. Dorizzi and B. Grammaticos, "Delay-induced desynchronization in neuronal oscillations," *Phys. Rev. A*, vol. 44, pp. 6958–6961, Nov 1991.

[55] S. Huang, J. Zhang, M. Wang, and C.-K. Hu, "Firing patterns transition and desynchronization induced by time delay in neural networks," *Physica A: Statistical Mechanics and its Applications*, vol. 499, pp. 88–97, 2018.

[56] E. Schöll, G. Hiller, P. Hövel, and M. A. Dahlem, "Time-delayed feedback in neurosystems," *Philosophical Transactions of the Royal Society A: Mathematical, Physical and Engineering Sciences*, vol. 367, no. 1891, pp. 1079–1096, 2009.

[57] L. Larger, B. Penkovsky, and Y. Maistrenko, "Virtual chimera states for delayed-feedback systems," *Phys. Rev. Lett.*, vol. 111, p. 054103, Aug 2013.

[58] V. Semenov, A. Zakharova, Y. Maistrenko, and E. Schöll, "Delayed-feedback chimera states: Forced multiclusters and stochastic resonance," *Europhysics Letters*, vol. 115, p. 10005, aug 2016.

[59] B. K. Bera and D. Ghosh, "Chimera states in purely local delay-coupled oscillators," *Phys. Rev. E*, vol. 93, p. 052223, May 2016.

[60] S. Kim, S. H. Park, and C. S. Ryu, "Multistability in coupled oscillator systems with time delay," *Phys. Rev. Lett.*, vol. 79, pp. 2911–2914, Oct 1997.

[61] J. Foss, A. Longtin, B. Mensour, and J. Milton, "Multistability and delayed recurrent loops," *Phys. Rev. Lett.*, vol. 76, pp. 708–711, Jan 1996.

[62] A. N. Pisarchik and U. Feudel, "Control of multistability," *Physics Reports*, vol. 540, no. 4, pp. 167–218, 2014. Control of multistability.

[63] C. Masoller, "Noise-induced resonance in delayed feedback systems," *Phys. Rev. Lett.*, vol. 88, p. 034102, Jan 2002.

[64] O. D'Huys, T. Jüngling, and W. Kinzel, "Stochastic switching in delay-coupled oscillators," *Phys. Rev. E*, vol. 90, p. 032918, Sep 2014.

[65] X. Tang, Z. M. Wu, J. G. Wu, T. Deng, L. Fan, Z. Q. Zhong, J. J. Chen, and G. Q. Xia, "Generation of multi-channel high-speed physical random numbers originated

from two chaotic signals of mutually coupled semiconductor lasers," *Laser Physics Letters*, vol. 12, p. 015003, nov 2014.

[66] G. Van der Sande, M. C. Soriano, I. Fischer, and C. R. Mirasso, "Dynamics, correlation scaling, and synchronization behavior in rings of delay-coupled oscillators," *Phys. Rev. E*, vol. 77, p. 055202, May 2008.

[67] B. Dorizzi, B. Grammaticos, M. Le Berre, Y. Pomeau, E. Ressayre, and A. Tallet, "Statistics and dimension of chaos in differential delay systems," *Phys. Rev. A*, vol. 35, pp. 328–339, Jan 1987.

[68] J. Lei and M. C. Mackey, "Deterministic brownian motion generated from differential delay equations," *Phys. Rev. E*, vol. 84, p. 041105, Oct 2011.

[69] S. A. Campbell, *Time Delays in Neural Systems*, pp. 65–90. Berlin, Heidelberg: Springer Berlin Heidelberg, 2007.

[70] T. Erneux, L. Larger, M. W. Lee, and J.-P. Goedgebuer, "Ikeda hopf bifurcation revisited," *Physica D: Nonlinear Phenomena*, vol. 194, no. 1, pp. 49–64, 2004.

[71] T. E. Murphy, A. B. Cohen, B. Ravoori, K. R. B. Schmitt, A. V. Setty, F. Sorrentino, C. R. S. Williams, E. Ott, and R. Roy, "Complex dynamics and synchronization of delayed-feedback nonlinear oscillators," *Philosophical Transactions of the Royal Society A: Mathematical, Physical and Engineering Sciences*, vol. 368, no. 1911, pp. 343–366, 2010.

[72] K. Kanno and A. Uchida, "Finite-time lyapunov exponents in time-delayed nonlinear dynamical systems," *Phys. Rev. E*, vol. 89, p. 032918, Mar 2014.

[73] J. Doyne Farmer, "Chaotic attractors of an infinite-dimensional dynamical system," *Physica D: Nonlinear Phenomena*, vol. 4, no. 3, pp. 366–393, 1982.

[74] K. Pyragas, "Synchronization of coupled time-delay systems: Analytical estimations," *Phys. Rev. E*, vol. 58, pp. 3067–3071, Sep 1998.

[75] D. Breda and S. D. Schiava *Discrete Continuous Dynamical Systems - B*, vol. 23, p. 2727, 2018.

[76] S. Torkamani and E. A. Butcher, “Delay, state, and parameter estimation in chaotic and hyperchaotic delayed systems with uncertainty and time-varying delay,” *International Journal of Dynamics and Control*, vol. 1, pp. 135–163, Jun 2013.

[77] A. Uchida, *Optical Communication with Chaotic Lasers.*

[78] K. Kanno, A. Uchida, and M. Bunsen, “Complexity and bandwidth enhancement in unidirectionally coupled semiconductor lasers with time-delayed optical feedback,” *Physical Review E*, vol. 93, no. 3, pp. 1–11, 2016.

[79] M. Zanin, L. Zunino, O. A. Rosso, and D. Papo, “Permutation entropy and its main biomedical and econophysics applications: A review,” *Entropy*, vol. 14, p. 1553–1577, Aug 2012.

[80] C. Bandt and B. Pompe, “Permutation entropy: a natural complexity measure for time series,” *Physical Review Letters*, vol. 88, no. 17, p. 4, 2002.

[81] L. Zunino, O. A. Rosso, and M. C. Soriano, “Characterizing the hyperchaotic dynamics of a semiconductor laser subject to optical feedback via permutation entropy,” *IEEE Journal of Selected Topics in Quantum Electronics*, vol. 17, no. 5, pp. 1250–1257, 2011.

[82] N. Li, W. Pan, A. Locquet, and D. S. Citrin, “Time-delay concealment and complexity enhancement of an external-cavity laser through optical injection,” *Opt. Lett.*, vol. 40, pp. 4416–4419, Oct 2015.

[83] B. R. R. Boaretto, R. C. Budzinski, K. L. Rossi, T. L. Prado, S. R. Lopes, and C. Masoller, “Discriminating chaotic and stochastic time series using permutation entropy and artificial neural networks,” *Scientific Reports*, vol. 11, p. 15789, Aug 2021.

[84] D. Rontani, A. Locquet, M. Sciamanna, D. S. Citrin, and S. Ortin, "Time-delay identification in a chaotic semiconductor laser with optical feedback: A dynamical point of view," *IEEE Journal of Quantum Electronics*, vol. 45, no. 7, pp. 879–1891, 2009.

[85] T. Heil, I. Fischer, W. Elsäßer, and A. Gavrielides, "Dynamics of semiconductor lasers subject to delayed optical feedback: The short cavity regime," *Phys. Rev. Lett.*, vol. 87, p. 243901, Nov 2001.

[86] J. Mørk, J. Mark, and B. Tromborg, "Route to chaos and competition between relaxation oscillations for a semiconductor laser with optical feedback," *Phys. Rev. Lett.*, vol. 65, pp. 1999–2002, Oct 1990.

[87] D. Rontani, A. Locquet, M. Sciamanna, and D. S. Citrin, "Loss of time-delay signature in the chaotic output of a semiconductor laser with optical feedback," *Opt. Lett.*, vol. 32, pp. 2960–2962, Oct 2007.

[88] J.-G. Wu, G.-Q. Xia, X. Tang, X.-D. Lin, T. Deng, L. Fan, and Z.-M. Wu, "Time delay signature concealment of optical feedback induced chaos in an external cavity semiconductor laser," *Opt. Express*, vol. 18, pp. 6661–6666, Mar 2010.

[89] R. M. Nguimdo, M. C. Soriano, and P. Colet, "Role of the phase in the identification of delay time in semiconductor lasers with optical feedback," *Opt. Lett.*, vol. 36, pp. 4332–4334, Nov 2011.

[90] K. Kanno and A. Uchida, "Consistency and complexity in coupled semiconductor lasers with time-delayed optical feedback," *Phys. Rev. E*, vol. 86, p. 066202, Dec 2012.

[91] C. Sugano, K. Kanno, and A. Uchida, "Reservoir computing using multiple lasers with feedback on a photonic integrated circuit," *IEEE Journal of Selected Topics in Quantum Electronics*, vol. 26, no. 1, pp. 1–9, 2020.

[92] J. Nakayama, K. Kanno, and A. Uchida, "Laser dynamical reservoir computing with consistency: an approach of a chaos mask signal," *Opt. Express*, vol. 24, pp. 8679–8692, Apr 2016.

[93] M. Tateno and A. Uchida, "Nonlinear dynamics and chaos synchronization in mackey-glass electronic circuits with multiple time-delayed feedback," *Nonlinear Theory and Its Applications, IEICE*, vol. 3, no. 2, pp. 155–164, 2012.

[94] J. Losson, M. C. Mackey, and A. Longtin, "Solution multistability in first-order nonlinear differential delay equations," *Chaos: An Interdisciplinary Journal of Nonlinear Science*, vol. 3, no. 2, pp. 167–176, 1993.

[95] S. Sano, A. Uchida, S. Yoshimori, and R. Roy, "Dual synchronization of chaos in mackey-glass electronic circuits with time-delayed feedback," *Phys. Rev. E*, vol. 75, p. 016207, Jan 2007.

[96] P. Amil, C. Cabeza, C. Masoller, and A. C. Martí, "Organization and identification of solutions in the time-delayed mackey-glass model," *Chaos: An Interdisciplinary Journal of Nonlinear Science*, vol. 25, no. 4, p. 043112, 2015.

[97] L. Weicker, T. Erneux, O. D'Huys, J. Danckaert, M. Jacquot, Y. Chembo, and L. Larger, "Slow–fast dynamics of a time-delayed electro-optic oscillator," *Philosophical Transactions of the Royal Society A: Mathematical, Physical and Engineering Sciences*, vol. 371, no. 1999, p. 20120459, 2013.

[98] J. D. Hart, L. Larger, T. E. Murphy, and R. Roy, "Delayed dynamical systems: networks, chimeras and reservoir computing," *Philosophical Transactions of the Royal Society A: Mathematical, Physical and Engineering Sciences*, vol. 377, no. 2153, p. 20180123, 2019.

[99] B. Romeira, F. Kong, W. Li, J. M. L. Figueiredo, J. Javaloyes, and J. Yao, "Broadband chaotic signals and breather oscillations in an optoelectronic oscillator incorporating a microwave photonic filter," *Journal of Lightwave Technology*, vol. 32, no. 20, pp. 3933–3942, 2014.

[100] Y. Chembo Kouomou, P. Colet, L. Larger, and N. Gastaud, "Chaotic breathers in delayed electro-optical systems," *Phys. Rev. Lett.*, vol. 95, p. 203903, Nov 2005.

[101] Y. K. Chembo, M. Jacquot, J. M. Dudley, and L. Larger, "Ikeda-like chaos on a dynamically filtered supercontinuum light source," *Phys. Rev. A*, vol. 94, p. 023847, Aug 2016.

[102] L. Larger, M. C. Soriano, D. Brunner, L. Appeltant, J. M. Gutierrez, L. Pesquera, C. R. Mirasso, and I. Fischer, "Photonic information processing beyond turing: an optoelectronic implementation of reservoir computing," *Opt. Express*, vol. 20, pp. 3241–3249, Jan 2012.

[103] L. Larger, J.-P. Goedgebuer, and F. Delorme, "Optical encryption system using hyperchaos generated by an optoelectronic wavelength oscillator," *Phys. Rev. E*, vol. 57, pp. 6618–6624, Jun 1998.

[104] C. Bimbard, E. Ledoux, and S. Ostojic, "Instability to a heterogeneous oscillatory state in randomly connected recurrent networks with delayed interactions," *Phys. Rev. E*, vol. 94, p. 062207, Dec 2016.

[105] J. Bélair, S. A. Campbell, and P. van den Driessche, "Frustration, stability, and delay-induced oscillations in a neural network model," *SIAM Journal on Applied Mathematics*, vol. 56, no. 1, pp. 245–255, 1996.

[106] G. Deco, V. Jirsa, A. R. McIntosh, O. Sporns, and R. Kötter, "Key role of coupling, delay, and noise in resting brain fluctuations," *Proceedings of the National Academy of Sciences*, vol. 106, no. 25, pp. 10302–10307, 2009.

[107] H. Wernecke, B. Sándor, and C. Gros, "Chaos in time delay systems, an educational review," *Physics Reports*, vol. 824, pp. 1–40, 2019. Chaos in time delay systems, an educational review.

[108] M. C. Soriano, L. Zunino, O. A. Rosso, I. Fischer, and C. R. Mirasso, "Time scales of a chaotic semiconductor laser with optical feedback under the lens of a permutation

information analysis," *IEEE Journal of Quantum Electronics*, vol. 47, no. 2, pp. 252–261, 2011.

[109] L. P. Shayer and S. A. Campbell, "Stability, bifurcation, and multistability in a system of two coupled neurons with multiple time delays," *SIAM J. Appl. Math*, vol. 61, pp. 673–700, 2000.

[110] J. D. Hart, R. Roy, D. Müller-Bender, A. Otto, and G. Radons, "Laminar chaos in experiments: Nonlinear systems with time-varying delays and noise," *Phys. Rev. Lett.*, vol. 123, p. 154101, Oct 2019.

[111] C. Masoller and A. C. Martí, "Random delays and the synchronization of chaotic maps," *Phys. Rev. Lett.*, vol. 94, p. 134102, Apr 2005.

[112] T. Dahms, P. Hövel, and E. Schöll, "Stabilizing continuous-wave output in semiconductor lasers by time-delayed feedback," *Phys. Rev. E*, vol. 78, p. 056213, Nov 2008.

[113] I. Fischer, O. Hess, W. Elsäβer, and E. Göbel, "High-dimensional chaotic dynamics of an external cavity semiconductor laser," *Phys. Rev. Lett.*, vol. 73, pp. 2188–2191, Oct 1994.

[114] A. Többens and U. Parlitz, "Dynamics of semiconductor lasers with external multicavities," *Phys. Rev. E*, vol. 78, p. 016210, Jul 2008.

[115] B. Mensour and A. Longtin, "Controlling chaos to store information in delay-differential equations," *Physics Letters A*, vol. 205, no. 1, pp. 18–24, 1995.

[116] J. E. S. Socolar, D. W. Sukow, and D. J. Gauthier, "Stabilizing unstable periodic orbits in fast dynamical systems," *Phys. Rev. E*, vol. 50, pp. 3245–3248, Oct 1994.

[117] A. Ahlborn and U. Parlitz, "Stabilizing unstable steady states using multiple delay feedback control," *Phys. Rev. Lett.*, vol. 93, p. 264101, Dec 2004.

[118] A. Longtin, "Oscillation onset in neural delayed feedback," p. 130–136, 1990.

[119] J. Mork, B. Tromborg, and J. Mark, "Chaos in semiconductor lasers with optical feedback: theory and experiment," *IEEE Journal of Quantum Electronics*, vol. 28, no. 1, pp. 93–108, 1992.

[120] L. Zunino, M. C. Soriano, I. Fischer, O. A. Rosso, and C. R. Mirasso, "Permutation-information-theory approach to unveil delay dynamics from time-series analysis," *Phys. Rev. E*, vol. 82, p. 046212, Oct 2010.

[121] D. Rontani, E. Mercier, D. Wolfersberger, and M. Sciamanna, "Enhanced complexity of optical chaos in a laser diode with phase-conjugate feedback," *Opt. Lett.*, vol. 41, pp. 4637–4640, Oct 2016.

[122] Y. Xu, L. Zhang, P. Lu, S. Mihailov, L. Chen, and X. Bao, "Time-delay signature concealed broadband gain-coupled chaotic laser with fiber random grating induced distributed feedback," *Optics Laser Technology*, vol. 109, pp. 654–658, 2019.

[123] X. Porte, O. D'Huys, T. Jüngling, D. Brunner, M. C. Soriano, and I. Fischer, "Autocorrelation properties of chaotic delay dynamical systems: A study on semiconductor lasers," *Phys. Rev. E*, vol. 90, p. 052911, Nov 2014.

[124] S. Heiligenthal, T. Dahms, S. Yanchuk, T. Jüngling, V. Flunkert, I. Kanter, E. Schöll, and W. Kinzel, "Strong and weak chaos in nonlinear networks with time-delayed couplings," *Phys. Rev. Lett.*, vol. 107, p. 234102, Nov 2011.

[125] C. W. Eurich, A. Thiel, and L. Fahse, "Distributed delays stabilize ecological feedback systems," *Phys. Rev. Lett.*, vol. 94, p. 158104, Apr 2005.

[126] D. Breda, *Stability of Linear Delay Differential Equations A Numerical Approach with Matlab*. 2015.

[127] A. Pikovsky and A. Politi, *Lyapunov Exponents: A Tool to Explore Complex Dynamics*. Cambridge University Press, 2016.

[128] T. Mikami, K. Kanno, K. Aoyama, A. Uchida, T. Ikeguchi, T. Harayama, S. Sunada, K.-i. Arai, K. Yoshimura, and P. Davis, "Estimation of entropy rate in a fast physical

random-bit generator using a chaotic semiconductor laser with intrinsic noise," *Phys. Rev. E*, vol. 85, p. 016211, Jan 2012.

[129] A. René and A. Longtin, "Mean, covariance, and effective dimension of stochastic distributed delay dynamics," *Chaos: An Interdisciplinary Journal of Nonlinear Science*, vol. 27, no. 11, p. 114322, 2017.

[130] M. C. Soriano, J. García-Ojalvo, C. R. Mirasso, and I. Fischer, "Complex photonics: Dynamics and applications of delay-coupled semiconductors lasers," *Rev. Mod. Phys.*, vol. 85, pp. 421–470, Mar 2013.

[131] S. Petkoski and V. K. Jirsa, "Transmission time delays organize the brain network synchronization," *Philosophical Transactions of the Royal Society A: Mathematical, Physical and Engineering Sciences*, vol. 377, no. 2153, 2019.

[132] B. Mensour and A. Longtin, "Chaos control in multistable delay-differential equations and their singular limit maps," *Phys. Rev. E*, vol. 58, pp. 410–422, Jul 1998.

[133] B. Penkovsky, X. Porte, M. Jacquot, L. Larger, and D. Brunner, "Coupled nonlinear delay systems as deep convolutional neural networks," *Phys. Rev. Lett.*, vol. 123, p. 054101, Aug 2019.

[134] M. Inubushi and K. Yoshimura, "Reservoir computing beyond memory-nonlinearity trade-off," *Scientific Reports*, vol. 7, no. 1, pp. 1–10, 2017.

[135] G. Kiss and G. Röst, "Controlling Mackey–Glass chaos," *Chaos: An Interdisciplinary Journal of Nonlinear Science*, vol. 27, no. 11, p. 114321, 2017.

[136] E. Schöll and H. G. Schuster, *Handbook of Chaos Control.* John Wiley and Sons, 2008, 2008.

[137] S. Coombes and C. Laing, "Delays in activity-based neural networks," *Philosophical Transactions of the Royal Society A: Mathematical, Physical and Engineering Sciences*, vol. 367, no. 1891, pp. 1117–1129, 2009.

[138] D. Müller, A. Otto, and G. Radons, “Laminar chaos,” *Phys. Rev. Lett.*, vol. 120, p. 084102, Feb 2018.

[139] R. Vicente, J. Dauden, P. Colet, and R. Toral, “Analysis and characterization of the hyperchaos generated by a semiconductor laser subject to a delayed feedback loop,” *IEEE Journal of Quantum Electronics*, vol. 41, no. 4, pp. 541–548, 2005.

[140] K. Engelborghs, T. Luzyanina, and D. Roose, “Numerical bifurcation analysis of delay differential equations using dde-biftool,” *ACM Trans. Math. Softw.*, vol. 28, p. 1–21, Mar. 2002.

[141] L. Larger, P.-A. Lacourt, S. Poinsot, and M. Hanna, “From flow to map in an experimental high-dimensional electro-optic nonlinear delay oscillator,” *Phys. Rev. Lett.*, vol. 95, p. 043903, Jul 2005.

[142] G. Stepan, *Retarded Dynamical Systems: Stability and Characteristic Functions.* Harlow: Longman, 1989.

[143] S. Yanchuk and P. Perlikowski, “Delay and periodicity,” *Phys. Rev. E*, vol. 79, p. 046221, Apr 2009.

[144] A. Longtin, “Noise-induced transitions at a hopf bifurcation in a first-order delay-differential equation,” *Phys. Rev. A*, vol. 44, pp. 4801–4813, Oct 1991.

[145] M. Madadi Asl, A. Valizadeh, and P. A. Tass, “Dendritic and axonal propagation delays may shape neuronal networks with plastic synapses,” *Frontiers in Physiology*, vol. 9, p. 1849, 2018.

[146] K. Bol, G. Marsat, E. Harvey-Girard, A. Longtin, and L. Maler, “Frequency-tuned cerebellar channels and burst-induced ltd lead to the cancellation of redundant sensory inputs,” *Journal of Neuroscience*, vol. 31, no. 30, pp. 11028–11038, 2011.

[147] N. Brunel and V. Hakim, “Fast global oscillations in networks of integrate-and-fire neurons with low firing rates,” *Neural Computation*, vol. 11, no. 7, pp. 1621–1671, 1999.

[148] W. Gerstner, R. Kempter, J. L. van Hemmen, and H. Wagner, "A neuronal learning rule for sub-millisecond temporal coding," *Nature*, vol. 383, pp. 76–78, Sep 1996.

[149] V. K. Jirsa and M. Ding, "Will a large complex system with time delays be stable?," *Phys. Rev. Lett.*, vol. 93, p. 070602, Aug 2004.

[150] S. Majhi, B. K. Bera, D. Ghosh, and M. Perc, "Chimera states in neuronal networks: A review," *Physics of Life Reviews*, vol. 28, pp. 100–121, 2019.

[151] J. Sawicki, S. Ghosh, S. Jalan, and A. Zakharova, "Chimeras in multiplex networks: Interplay of inter- and intra-layer delays," *Frontiers in Applied Mathematics and Statistics*, vol. 5, p. 19, 2019.

[152] K. Matsumoto and I. Tsuda, "Noise-induced order," *Journal of Statistical Physics*, vol. 31, pp. 87–106, Apr 1983.

[153] K. Rajan, L. F. Abbott, and H. Sompolinsky, "Stimulus-dependent suppression of chaos in recurrent neural networks," *Phys. Rev. E*, vol. 82, p. 011903, Jul 2010.

[154] A. Litwin-Kumar and B. Doiron, "Slow dynamics and high variability in balanced cortical networks with clustered connections," *Nature Neuroscience*, vol. 15, pp. 1498–1505, Nov 2012.

[155] D. Pazó and E. Montbrió, "From quasiperiodic partial synchronization to collective chaos in populations of inhibitory neurons with delay," *Phys. Rev. Lett.*, vol. 116, p. 238101, Jun 2016.

[156] S. Luccioli, D. Angulo-Garcia, and A. Torcini, "Neural activity of heterogeneous inhibitory spiking networks with delay," *Phys. Rev. E*, vol. 99, p. 052412, May 2019.

[157] R. Zillmer, N. Brunel, and D. Hansel, "Very long transients, irregular firing, and chaotic dynamics in networks of randomly connected inhibitory integrate-and-fire neurons," *Phys. Rev. E*, vol. 79, p. 031909, Mar 2009.

[158] H. D. I. Abarbanel, R. Brown, and J. B. Kadtke, "Prediction in chaotic nonlinear systems: Methods for time series with broadband fourier spectra," *Phys. Rev. A*, vol. 41, pp. 1782–1807, Feb 1990.

[159] G. Xiaofeng and C. H. Lai, "Improvement of the local prediction of chaotic time series," *Phys. Rev. E*, vol. 60, pp. 5463–5468, Nov 1999.

[160] L. Maguire, B. Roche, T. McGinnity, and L. McDaid, "Predicting a chaotic time series using a fuzzy neural network," *Information Sciences*, vol. 112, no. 1, pp. 125–136, 1998.

[161] H. Jaeger and H. Haas, "Harnessing nonlinearity: Predicting chaotic systems and saving energy in wireless communication," *Science*, vol. 304, no. 5667, pp. 78–80, 2004.

[162] S. Krishnagopal, M. Girvan, E. Ott, and B. R. Hunt, "Separation of chaotic signals by reservoir computing," *Chaos: An Interdisciplinary Journal of Nonlinear Science*, vol. 30, no. 2, p. 023123, 2020.

[163] J.-Y. Tang, B.-D. Lin, J. Yu, X. He, and C. Wang, "Parallel time-delay reservoir computing with quantum dot lasers," *IEEE Journal of Quantum Electronics*, vol. 58, no. 2, pp. 1–9, 2022.

[164] M. C. Soriano, S. Ortín, L. Keuninckx, L. Appeltant, J. Danckaert, L. Pesquera, and G. van der Sande, "Delay-based reservoir computing: Noise effects in a combined analog and digital implementation," *IEEE Transactions on Neural Networks and Learning Systems*, vol. 26, no. 2, pp. 388–393, 2015.

[165] Y. Paquot, F. Duport, A. Smerieri, J. Dambre, B. Schrauwen, M. Haelterman, and S. Massar, "Optoelectronic reservoir computing," *Scientific Reports*, vol. 2, p. 287, Feb. 2012.

[166] L. Larger, A. Baylón-Fuentes, R. Martinenghi, V. S. Udaltsov, Y. K. Chembo, and M. Jacquot, "High-speed photonic reservoir computing using a time-delay-based ar-

chitecture: Million words per second classification," *Phys. Rev. X*, vol. 7, p. 011015, Feb 2017.

[167] D. Wenkack Liedji, J. H. Talla Mbé, and G. Kenne, "Classification of hyperchaotic, chaotic, and regular signals using single nonlinear node delay-based reservoir computers," *Chaos: An Interdisciplinary Journal of Nonlinear Science*, vol. 32, no. 12, p. 123126, 2022.

[168] K. Kanno, A. A. Haya, and A. Uchida, "Reservoir computing based on an external-cavity semiconductor laser with optical feedback modulation," *Opt. Express*, vol. 30, pp. 34218–34238, Sep 2022.

[169] M. Goldmann, F. Köster, K. Lüdge, and S. Yanchuk, "Deep time-delay reservoir computing: Dynamics and memory capacity," *Chaos: An Interdisciplinary Journal of Nonlinear Science*, vol. 30, no. 9, p. 093124, 2020.

[170] F. Stelzer, A. Röhm, R. Vicente, I. Fischer, and S. Yanchuk, "Deep neural networks using a single neuron: folded-in-time architecture using feedback-modulated delay loops," *Nature Communications*, vol. 12, p. 5164, Aug. 2021.

[171] T. Hülser, F. Köster, L. Jaurigue, and K. Lüdge, "Role of delay-times in delay-based photonic reservoir computing," *Optical Materials Express*, vol. 12, no. 3, pp. 1214–1231, 2022.

[172] F. Stelzer, A. Röhm, K. Lüdge, and S. Yanchuk, "Performance boost of time-delay reservoir computing by non-resonant clock cycle," *Neural Networks*, vol. 124, pp. 158–169, 2020.

[173] J. Jin, N. Jiang, Y. Zhang, W. Feng, A. Zhao, S. Liu, J. Peng, K. Qiu, and Q. Zhang, "Adaptive time-delayed photonic reservoir computing based on kalman-filter training," *Opt. Express*, vol. 30, pp. 13647–13658, Apr 2022.

[174] F. Köster, S. Yanchuk, and K. Lüdge, "Insight into delay based reservoir computing via eigenvalue analysis," *Journal of Physics: Photonics*, vol. 3, p. 024011, apr 2021.

[175] L. Jaurigue, E. Robertson, J. Wolters, and K. Lüdge, “Reservoir computing with delayed input for fast and easy optimisation,” *Entropy*, vol. 23, no. 12, 2021.

[176] Y.-S. Hou, G.-Q. Xia, E. Jayaprasath, D.-Z. Yue, W.-Y. Yang, and Z.-M. Wu, “Prediction and classification performance of reservoir computing system using mutually delay-coupled semiconductor lasers,” *Optics Communications*, vol. 433, pp. 215–220, 2019.

[177] Z. Lu, J. Z. Kim, and D. S. Bassett, “Supervised chaotic source separation by a tank of water,” *Chaos: An Interdisciplinary Journal of Nonlinear Science*, vol. 30, no. 2, p. 021101, 2020.